Available online at www.sciencedirect.com

jmr&t Journal of Materials Research and Technology

journal homepage: www.elsevier.com/locate/jmrt

Original Article

Strain-rate effects and dynamic behavior of high entropy alloys

Aomin Huang [a], *Saryu J. Fensin* [b], *Marc André Meyers* [a,*]

[a] *University of California, San Diego, USA*
[b] *Los Alamos National Laboratory, USA*

ARTICLE INFO

Article history:
Received 31 July 2022
Accepted 8 November 2022
Available online 15 November 2022

Keywords:
Dynamic behavior
Shock
Shear bands
Dislocations
HEAs
Twinning
High entropy alloys

ABSTRACT

The novel class of multicomponent alloys, also known as high-entropy alloys (HEAs) exhibits excellent properties under low strain-rate conditions. These are especially revealed in the high strength of nanocrystalline CoCrFeMnNi and AlNbTiV alloys, and in the high fracture toughness of AlCoCrCuFeNi and NbMoTaW alloys. Nevertheless, up to now, the dynamic behavior of these high-entropy alloys has not been investigated to the same extent as the quasi-static response. A significantly different mechanical response, such as spallation failure and shear localization, manifests itself when materials are subjected to dynamic loading. Shear localization is an essential precursor to shear failure; studies addressing retardation of its onset are important because of their relevance to applications such as armor for military use. The resistance to shear localization is associated with the extensive work hardening ability enabled by dislocation slip, twinning, and phase transformations which override thermal softening. Apart from shear localization, in contrast to the conventional fracture failure dictated by fracture toughness, spallation resulting from tensile pulses and involving propagating micro-cracks and/or micro-voids also plays an important role in dynamic performance. Although distinctive behaviors have also been reported for other conventional metallic materials under dynamic loading, the unique characteristics of HEAs warrant this review.

1. Introduction

Numerous studies have been directed towards a novel class of alloys with multiple-principal elements, also known as high-entropy alloys (HEAs). Conventional alloys normally contain one single principal element with addition of other elements in varying amounts to tailor properties. In contrast, high entropy alloys [1,2] are comprised of five or more principal elements to maximize configurational entropy ΔS_{config} ($\Delta S_{config} = RlnN$, where N is the number of elements in system), which promotes formation of liquid or random solid solution phases with simple structures such as body-centered cubic (BCC) and face-centered cubic (FCC) and deters the formation of brittle intermetallic phases. High-entropy alloys (HEAs) as novel metallic materials were first discovered in 2004 [1,2]. Based on their constituent elements, HEAs can be classified into five different classes: 1) 3-D transition metals only, 2) transition metals with

* Corresponding author.
E-mail address: mameyers@ucsd.edu (M.A. Meyers).
https://doi.org/10.1016/j.jmrt.2022.11.057

elements possessing larger atomic radii, 3) HEAs composed of refractory metals, 4) ceramic HEAs comprised of oxygen, boron and other anions and 5) others which are comprised of 4f elements Dy, Lu, Tb, Y. Due to multiple constituent elements in HEAs, unique properties, i.e., high hardness/strength, excellent wear resistance and damping capacity, have been discovered. Although mechanical properties at low strain-rates have been the focus of many research efforts and reviews [3–8], properties when the HEAs are subjected to dynamic loading have yet to be fully investigated [3–6].

1.1. *Core effects of HEAs*

In comparison with conventional alloys, four core effects, which are: (1) High-entropy effect; (2) Sluggish diffusion effect; (3) Severe lattice distortion effect; (4) Cocktail effect, are proposed as possible reasons that render HEAs unique, as shown in Fig. 1. Discussion of each individual effect will be presented first. The high entropy effect describes the thermodynamics which can influence equilibrium structures and microstructures, thereby playing an important role in alloy design. Sluggish diffusion effect is involved in other aspect, which is phase transformation. As for severe lattice distortion effect, it is of great importance to mechanical properties (i.e., dislocation movement) and it is closely related to three other effects. The cocktail effect derives its name from synergy of compositions and microstructures. Finally, the short-range ordering effect, as a newly added crucial effect of HEAs, originates from distinctive energetic favorability between different atomic pairings.

The high entropy effect, which is explained via thermodynamic theory, illustrates the relationship between enhanced system stability and increasing number of elements. According to $\Delta G_{mix} = \Delta H_{mix} - T\Delta S_{mix}$ [9] (where T is the temperature, ΔG_{mix} is mixing Gibbs free energy, ΔH_{mix} is mixing enthalpy and ΔS_{mix} is mixing entropy), an increment of mixing entropy promotes smaller Gibbs free energy and enhances solid solution phase stability, especially at elevated temperature. Although random solid solution is considered as the stable phase in HEAs, the formation of multiphases, such as nanoprecipitates and second phases, is commonly found, which can be attributed to local stress/strain, varying interatomic interaction, enthalpy and other effects [10]. One recent study [11] discovered a second-phase formation when the CoCrFeMnNi HEA was subjected to a 700 °C annealing treatment for 1000 h, which questioned the stability of random solid solution phase in HEAs. In addition, owning to high configurational entropy, solid solution phase is believed to be stable status of HEAs. That is, non-configurational entropy and mixing enthalpy are thought to be negligible in HEAs. However, such assumption can only be valid in ideal solid solutions, where total Gibbs free energy is governed by configurational entropy. Otto [12] proposed in his work that none of the equiatomic alloys comprised of five principal elements displayed a single solid solution phase, suggesting a higher enthalpy and non-configurational entropy that can no longer be overlooked. Nevertheless, An et al. [13] achieved a near single phase in CoCrCuFeNi-based HEAs, regardless of positive mixing enthalpy, by applying radio frequency sputtering combined with rapid quenching.

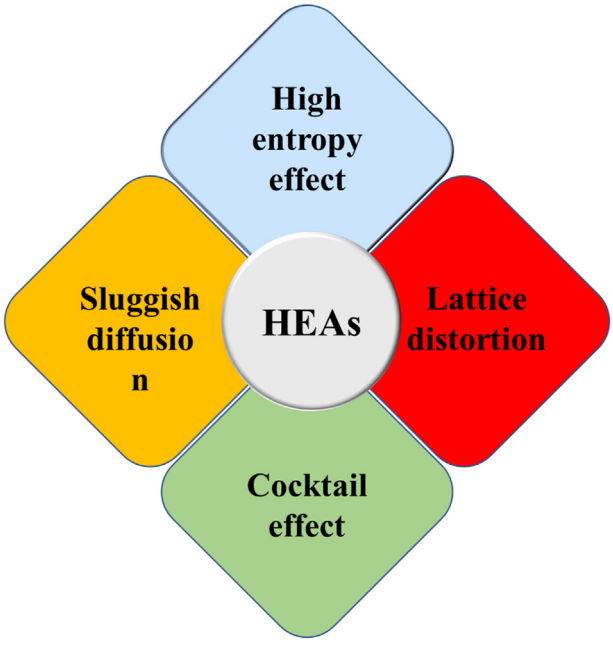

Fig. 1 – Schematic illustration of four core effects in HEAs.

A certain lattice potential energy barrier (LPE) needs to be overcome for atomic migration to occur from one site to another. For HEAs, significantly different diffusional behavior in comparison with conventional alloys, namely sluggish diffusion effect, has been put forward by Yeh [1]. Such effect is mainly derived from a substantial variety of neighboring atoms of each lattice site, thereby generating different LPEs. In contrast, pure metals have constant LPEs throughout all lattice sites due to identical surrounding atmosphere of atomic arrangement. One can imagine that if an atom jumps from a high-energy site to a lower energy vacancy site, it can be "trapped". Meanwhile, if an atom is initially at a low-energy site, then jumps to a high-energy vacancy site, it tends to return to the original site. Both situations promote sluggish diffusion and inhibit atomic migration.

The lattice distortion effect is mainly derived from a variety of atomic sizes in the lattice. Due to the nature of vast amounts of constituent compositions in HEAs, the differences in atomic sizes and bonding energies contribute to high tendency to form the severe lattice distortion effect. Assuming no chemical ordering, all elements are randomly placed in the lattice and the atoms with larger radii will push the smaller ones away from their original positions, thereby generating strain energy and affecting the HEAs' properties. Atomic mismatches can be large in some circumstances, thereby forming a severe lattice distortion effect. Such effect has been observed in both BCC [14,15] and FCC [16,17] matrix HEAs.

The term "cocktail effect" was first put forward by Ranganathan [18] to describe metallic alloys. Such effect illustrates that the mechanical and physical properties can be altered unexpectedly by mixing multiple components. For example, with increasing atomic fraction of Al, rising hardness and conversion of FCC matrix to BCC matrix phase have been observed in $CoCrCuNiAl_x$ HEAs [1]. The drastic change of hardness (from 133HV to 655HV) achieved by altering atomic fraction of Al is

partly attributed to an increasing atomic mismatch and strong interatomic binding force between Al atoms and other metallic atoms. This effect really represents unpredictable properties caused by the great variety of compositional choices for HEAs.

Short-range ordering (SRO) has been widely observed in binary alloy systems [17,19–21] and is considered to be one of the major strengthening mechanisms. Preceding studies have investigated SRO in both BCC-based [22,23] and FCC-based [24,25] HEAs. This effect is closely related to bonding energy between atoms and local strain energy. Although HEAs are believed to be random solid solutions, some studies [26–29] point out that certain degrees of ordering arrangement of atoms can take place at local domains, resulting in SRO structures. If the mixing enthalpy between certain atoms is lower than others in system, denoting a stronger favorability, then SRO can develop. Due to the complexity of multi-component systems, energetic favorability among atomic pairings can be vastly different. Regarding the formation of SRO, another important factor is local strain energy. Due to lattice distortion, strain energy at some local domains can be much higher than the average, suggestive of metastable state regions. Thus, in order to mitigate strain energy, atoms need to realign, and this leads to SRO. Unlike long-range ordering, such ordered atomic arrangements can only persist over a few to several interatomic distances. Simulations predicting SRO with corresponding four groups of configurations in CrCoNi alloy were reported by Ding et al. [30] illustrating a strong relationship between local chemical order and stacking-fault energy. In addition to computational simulation, such local ordering structure has also been discovered in CrCoNi alloy via energy-filtered transmission electron microscopy by Zhang et al. [29]. They have concluded that tailoring SRO is of great importance to mechanical properties, such as promoting dislocation planar slip in FCC metals and altering Peierls-Nabarro energy barriers. The interaction between SRO and dislocation carriers, e.g., twinning, dislocation, lattice resistance, is summarized in Fig. 2.

1.2. *Deformation mechanisms*

Due to intriguing features derived from inherently complex compositions of HEAs, their response to dynamic loading can be very distinctive in contrast to conventional metallic materials. For instance, the SFE of HEAs can be varied significantly from one domain to another due to presence of local chemical order in comparison with uniform SFE throughout conventional metallic materials. Such unique phenomenon can strongly affect dislocation glide mode and their dissociation, which leads to different deformation substructures such as deformation twins, deformation-induced microbands, slip bands, phase transitions and, in some extreme cases, amorphization. Phase transformations in HEAs are significantly affected by residual strains and lattice distortion, which result from atomic size mismatch between different constituent elements. These residual strains can subsequently contribute a "driving force" to induce phase transformation [31]. In addition, the deformation mechanism can also be altered when the loading condition is changed, and the changing path can be different in HEAs. For example, rising strain rate is widely believed to promote wavy to planar glide transition [32]; however, the dislocation substructures in FCC solid solution HEAs may not follow this rule due to "planar softening rule" [33]. One of the main foci in the current review is how the change in loading conditions can actually alter the dynamic properties considering the unique characteristics of HEAs.

2. Mechanical behavior

2.1. *Dynamic behavior*

The study of the dynamic response of materials involves several disciplines, including physics, chemistry, mechanics, and materials science. The classic definition of dynamic behavior requires that materials undergo a non-static condition of rapidly changing loading; they therefore exhibit very different properties in comparison with materials subjected to static and quasi-static conditions of loading [34]. Besides, in contrast to quasi-static and static deformation that maintain static equilibrium condition, due to higher strain-rate subjected at dynamic deformation, inhomogeneous distribution of stress is often generated. Such is the case with elastic, plastic, and shock-wave propagation.

One important effect that occurs when dislocations are forced to move at high velocities is viscous phonon drag [35–37]. Such effect is due to the rapidly propagating dislocations interacting with the elastic lattice vibrations. Phonon drag is negligible at quasi-static conditions because the dislocation movement is too slow to interact with the phonons. In addition, such viscous drag effect at low temperature, at which electron drag becomes more active and dominant, is prohibited due to small population of phonons [38]. This high-

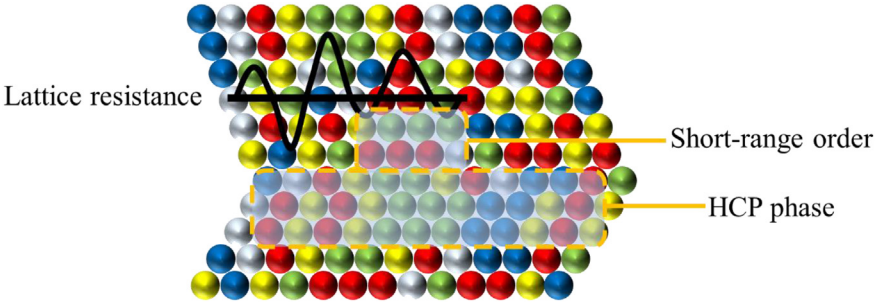

Fig. 2 – Schematic illustration of the interplay between SROs and different deformation carriers in a representative FCC HEA [226].

velocity effect contributes to the scattering of phonons, which significantly influences the viscosity and the frictional force. Operative phonon drag effect is always coupled with vastly increased yield strength.

Apart from the phonon drag effect, additional deformation mechanisms, for instance, deformation twinning, phase transformations, shear banding, are operative in metallic materials subjected to high strain rate deformation [34,35]. One major downside of dynamic deformation is, often, a deteriorating ductility. Therefore, a comprehensive understanding of high strain-rate plastic deformation behavior is essential for its potential use in structural engineering applications. In terms of experimental methods, strain-rate ranges from 10 to 10^8 s^{-1} can be produced by varying approaches, such as dynamic compression on split-Hopkinson pressure bar, shock compression in gas guns, laser-driven systems, detonation waves from explosives, ballistic impact, etc. However, there is a limit to the strain rates that can be achieved experimentally, and the mechanical response at strain rates higher than on the order of 10^9 s^{-1} is difficult to investigate. In this regime we have to rely on simulations, especially molecular dynamics.

2.2. Thermally activated process

The deformation behavior of metals and alloys strongly depends on strain rate and temperature, indicative of a thermally activated process [32]. This process is predominantly determined by required stress-dependent Gibbs free energy $\Delta G(\sigma)$ to enable dislocation glide. In order for a dislocation to move, possible obstacles, such as solute atoms, precipitates, need to be bypassed. The activation volume V is usually used to represent how much material is involved in the thermally activated processes. It is defined as:

$$V = \frac{\partial(\Delta G(\tau))}{\partial \tau}\Big|_T = -M\frac{\partial(\Delta G(\sigma))}{\partial \sigma}\Big|_T = MKT\frac{\partial \ln(\dot{\varepsilon})}{\partial \sigma}\Big|_T = bA \tag{2.1}$$

where M = 3.06 is an orientation factor, σ is uniaxial stress, τ is shear stress, b is the Burgers vector., T is temperature, $\dot{\varepsilon}$ is plastic strain and A is activation area swept by dislocation. V is usually expressed in units of b^3. Given that incremental strength derived from grain size strengthening is usually thought to be independent from temperature and strain rate [39,40], solid solution and dislocation–dislocation interaction provide dominant contributions to the strengthening effect. The activation volume for solid solution FCC HEAs can be expressed as follows:

$$\frac{1}{V} = \frac{1}{V_{ss}} + \frac{1}{V_f} \tag{2.2}$$

where the two terms denote contributions caused by solid solution strengthening and forest hardening.

The activation volume contributed by solute strengthening can be written as [41–43]:

$$V_{ss} = \frac{0.55\Delta E_b(T)M}{\sigma_{ss}} \tag{2.3}$$

where $\Delta E_b(T)$ is the energy barrier that needs to be bypassed for the change of shear modulus at temperature T, σ_{ss} is the incremental stress due to solid solution strengthening.

The activation volume derived from the multiplication of dislocations can be formulated as [44]:

$$V_f = \frac{M\alpha G b^2 w}{\sigma_f} \tag{2.4}$$

where σ_f is the incremental stress due to forest hardening, w is the length scale of junction barrier overcome by a dislocation, and parameter α represents rate dependence of breaking dislocation from the forest network. In contrast to conventional FCC metals with high activation volumes ranging from 200 to 2000 b^3, a much smaller activation volume between 7 and 77 b^3 was reported [45] for CoCrFeMnNi alloy at temperatures of 77 K and 298 K, respectively. The difference in their activation volume is attributed to much smaller number of solute atoms in CoCrFeMnNi alloy. In addition, deformation mechanisms of micro/nano-crystalline materials can be identified by their activation volume, where dislocation glide and dislocation–dislocation interaction prevail in the regime of ~100 b^3 to 1000 b^3, and interphase boundaries dominate in the regime of ~10 b^3. Fan et al. [46] proposed a flow stress "upturn" at the strain rate between 10^3 s^{-1} to 10^4 s^{-1}. This "upturn" has been previously attributed to the onset of non-Arrhenius response [47–50]. They have discovered an ultra-small activation volume in the high stress region, which causes high strain-rate sensitivity.

2.3. Strengthening mechanisms

Metals are characterized by non-directional metallic bonding and higher probability to form defects. Thus, the development of strengthening mechanisms is essential. Apart from tuning chemical bonding or crystalline structure, interfering with the movement of defects via stress fields or substructures is the most effective method of strengthening metals. The most common strengthening mechanisms are grain-boundary strengthening, precipitation strengthening, two-phase hardening, solute strengthening, and order strengthening [55,66].

2.3.1. Dislocation strengthening

Forest hardening is a strengthening effect that arises from increasing dislocation density coupled with the formation of dislocation junctions during plastic deformation. Such junctions are able to restrain dislocation motion, leading to strain hardening, until it is compromised by sufficiently high local stress. The relationship between critical resolved shear stress to destroy junctions and dislocation density can be expressed by the following equation:

$$\tau_{CRSS} = \alpha G b\sqrt{\rho} \tag{2.5}$$

where α is a parameter, ρ is dislocation density.

With respect to the strain rate effect on dislocation substructures, Sevillano et al. [52] proposed that a rising strain rate can generate comparable effect to reducing the temperature and SFE. Coupled with the rising rate is the shift of dislocation glide mode, from wavy to planar, which thereafter refines the dislocation cells and traps dislocations inside the cell structure [53]. Classic CoCrFeMnNi alloy dislocation movement was found to be governed by planar glide on {111} slip planes [39,54] at strain rates below 3×10^3 s^{-1}, which was

also commonly found in the family of low SFE [55,56], short-range ordered [33], or high frictional stress [57] metallic materials. Although planar slip is favored in low SFE materials, it has also been discovered in some solid solution FCC alloys with high SFE due to the "glide plane softening" effect [33]. This effect relies heavily on the short-range ordering. Wong and his co-workers [58] developed a tunable dislocation glide mode for $Al_{0.3}CoCrFeNiMn_x$ by modifying the atomic fraction of Mn. While low Mn alloys displayed wavy glide dominance, their high Mn counterparts were dominated by planar glide. In the higher strain-rate region ($9 \times 10^3\ s^{-1}$), Tsai et al. [54] proposed a transition of deformation mechanism, from dislocation-glide to nano-twinning in the CoCrFeMnNi alloy.

2.3.2. *Solution strengthening*

The strengthening effect derived from interaction between solute atoms and dislocations, more specifically, the former's strain field and the latter's stress field [51,56–59], is widely known as the reason behind solid solution strengthening. As a result, an increasing resolved shear stress is required to effect continuous plasticity by dislocation motion, thereby subsequently leading to an enhanced yield strength. Two sets of models, strong (Fleischer model) [60–63] and weak pinning models (Labusch model) [64,65], as shown in Fig. 3, were developed to describe solid solution strengthening in alloys. In the strong pinning model, solutes are treated as individual point obstacles, resulting in strong pinning effect. Meanwhile, in the weak pinning model, energetic fluctuation due to collective effect in area with randomly distributed solutes, decreases the dislocation energy, thereby providing a weak pinning effect. Contrary to the Fleischer model, in which solute atoms are expected to be sparsely and randomly distributed with low concentration, the Labusch model demonstrates a strengthening effect related to a forest of solute atoms, which is proposed to be more applicable to multi-component solution alloys [67–69] with varied atomic sizes. Assuming a single solute species i, the incremental strength analyzed by Labusch model can be formulated as [64–69]:

$$\Delta\sigma_{ss} = f\mu\left[\left(\frac{\eta_i}{1+\frac{1}{2}|\eta_i|}\right)+\alpha^2\delta_i^2\right]^{\frac{2}{3}} x_i^{\frac{2}{3}} \tag{2.6}$$

where f and α are dimensionless parameters, μ is shear modulus, η_i, x_i and δ_i are elastic modulus, molar fraction and lattice mismatches of solute species i, respectively. The strengthening effect estimated by the Fleisher model can be expressed as:

$$\Delta\sigma_{ss} = B_i X_i^{\frac{1}{2}} \tag{2.7}$$

where B_i is a constant related to shear modulus and X_i is the solute content. However, due to variation of composition, atomic size misfit, and interatomic distance, strengthening of HEAs is usually estimated through the Labusch model [68]. Derived from binary system, Toda-Caraballo developed a model named after himself [68,70] to describe solid solution strengthening in HEAs. This model can be formulated as:

$$\Delta\sigma_{ss} = F_t Z G B x^n \tag{2.8}$$

where F_t is the orientation factor, Z is scaling factor, G is the shear modulus, n is Labusch dependence and can be determined to be 2/3 for concentrated alloys, and x is solute content. The term B is used to describe the resultant total lattice distortion caused by solute atoms and can be expressed as:

$$B = \left(\xi\sqrt{\{\eta'\}^2+\{\alpha\delta\}^2}\right)^{\frac{4}{3}} \tag{2.9}$$

where ξ is number of active slip systems in the alloy. η' represents the elastic modulus mismatch between the solute and solvent. α is a constant indicating whether screw or edge dislocations prevail. A larger α corresponds to an increasing fraction of edge dislocations. δ is the atomic size mismatch.

Solid solution strengthening of FCC HEAs turns out to be comparable to that discovered in conventional alloys, with respect to atomic size mismatch governance and magnitude of activation volume [68,70–72]. However, its BCC counterpart, where deformation is mainly controlled by screw dislocation motion, exhibits both strengthening and softening effects [73,74]. Maresca and Curtin [75] developed a model for solution strengthening specifically in BCC materials, by placing more emphasis on edge dislocation motion. Senkov et al. [76] and and Yao et al. [77], however, have put forward a model incorporating elastic modulus mismatch which can be formulated as:

$$\Delta\sigma b^2 = ZF^{\frac{4}{3}}c^{\frac{2}{3}}E_L^{-\frac{1}{3}} \tag{2.10}$$

where Z is dimensionless material constant, b is Burgers vector, E_L is the dislocation line tension, F is the interaction force. Therefore, in general, these three models –Toda-Caraballo, Senkov-Yao, and Maresca– place emphasis on different factors, which are atomic size mismatch, elastic modulus mismatch, and edge dislocation motion, respectively.

Coury et al. [78] studied solution strengthening of NbTaTi, MoNbTaTi, WnbTaTi, HfNbTaTi, CrNbMoTi and CrMoTaTi refractory HEAs by applying these three models, reporting that the Toda-Caraballo could not produce as accurate prediction to refractory HEAs as to FCC HEAs [68,70,79].

2.3.3. *Grain size strengthening*

Grain boundaries provide pronounced strengthening effect at low temperatures. Traditional grain-boundary strengthening is expressed through the classic Hall-Petch equation:

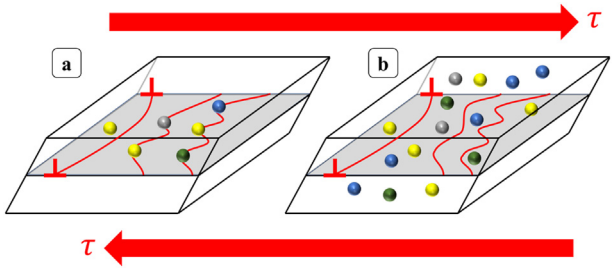

Fig. 3 – Schematic of classic solution strengthening mechanisms: (a) Fleischer model and (b) Labusch model.

$$\sigma_y = \sigma_{y0} + K_{HP} d^{-0.5} \tag{2.11}$$

where σ_y is yield stress, d is the grain size, K_{HP} is the Hall-Petch coefficient. According to this equation, the strength of crystalline materials is inversely proportional to grain size to the power of 1/2. Schuh et al. [80] reported a superior tensile strength obtained in a nanocrystalline Cantor alloy. The nanocrystalline structure provides a high-volume fraction of grain boundaries which act as obstacles to prevent further movement of dislocations. Although significantly enhanced strength can be obtained, an undermined ductility comes along with it. Gangireddy [81] and his co-workers discovered an inversely proportional relationship between strain rate sensitivity and strength when grain cell size is larger than dislocation cell. The grain size is also related to the hardness [82].

2.3.4. *Twinning*

Twinning is an excellent work hardening mechanism and provides similar strengthening effect as high-angle grain boundaries [68], by impeding the migration of dislocations and by generating additional sites for dislocation nucleation. Interaction between dislocations and twin boundaries has been extensively studied and divided into three routes in FCC metals [69,70]: slip transfer, confined-layer slip and twinning partial slip (Fig. 4). Regarding slip transfer and confined-layer slip, dislocations will rather be converted into partial dislocations and move along twin boundaries and interior domains, or create dislocation junctions, which are also known as hard mode I and II. However, when maximum shear loading is applied along the twin plane, restraints caused by twin boundaries are significantly weakened, which is known as "soft mode". A promising approach to provide a desirable combination of enhanced ductility and strength by introducing twinning has been investigated experimentally [71–77] The formation of twins can be mainly achieved by two routes: mechanical deformation, or appropriate annealing treatment. In the latter, the thickness of annealing twins will be typically larger than that for deformation twins. A large twin width is accompanied by wider spacing between twin boundaries, thereby weakening the effect of blocking dislocation movement. Thus, a superior hardening effect is always associated with deformation twins due to much smaller distance between twin boundaries. Initiation of mechanical twins is closely dependent on stacking fault energy; in low stacking-fault energy (<~20 mJ/m^2) materials, twinning turns out to be the dominant deformation mechanism. Certain conditions, such as low strain rate and high deformation temperature can inhibit mechanical twinning. Meyers et al. [92] developed a constitutive description of twinning stress, by which the effect of temperature, strain rate and grain size on twinning stress can be predicted. The twinning stress in FCC metals can be expressed as [78]:

$$\sigma_T = \alpha_T \left(\frac{\gamma_{SF}}{Gb}\right)^{\frac{1}{2}} \tag{2.12}$$

where α_T is a fitting parameter, γ_{SF} is stacking-fault energy, G is shear modulus and b is the Burgers vector. It is often assumed that the temperature and strain rate have only a modest effect on the twinning stress. Twinning occurs when σ_T is equal to or lower than slip stress σ_S, whose relationship with strain rate and temperature can be expressed by the Zerilli-Armstrong equation for FCC metals:

$$\sigma_s = \sigma_G + C_1 \varepsilon^{\frac{1}{2}} \left\{ exp - \left[-C_2 - C_3 \ln\left(\frac{\dot{\varepsilon}}{\dot{\varepsilon}_0}\right)\right] T \right\} \tag{2.13}$$

where σ_G is athermal stress, $\dot{\varepsilon}_0$ is a reference strain rate, C_1, C_2, and C_3 are parameters. In contrast to the twinning stress, the slip stress is closely related to temperature and strain rate. The tendency to form mechanical twins is mainly associated with rivalry between twinning stress and slip stress, while lower slip stress makes it more difficult to form twinning. In high SFE FCC metals, twinning is prohibited at quasi-static loading conditions; however, it is extensively generated under shock loading [94,95]. As for BCC and HCP, increasing strain rate has a comparable effect on twin formation as decreasing temperature [96]. Contrary to FCC, BCC and HCP exhibit lower probability to form twins, due to lack of potential slip systems [93,97]. Despite SFE being of great importance for tendency for twin formation (see Eq. (2.12)), another

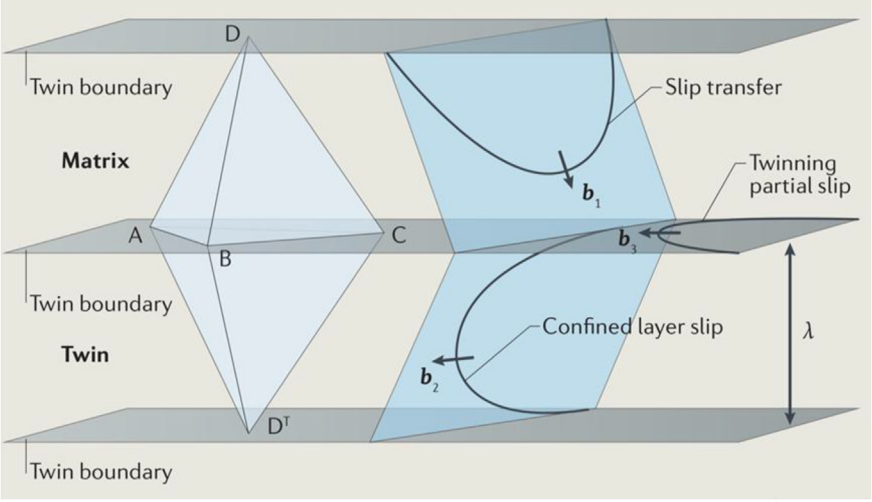

Fig. 4 – Interaction between dislocations and twin boundaries in FCC metals [227].

important factor, which is also essential, is the deformation mode. For instance, although deformation twins were found in uniaxially compressed CrMnFeCoNi HEA, none was discovered in tensioned alloys subjected to uniaxial tension. Mostly, decreasing temperature is coupled with lower stacking, which promotes the twinning-induced plasticity (TWIP) effect in FCC metals [98]. Such effect can be tailored by adjusting composition. Deng et al. [99] claimed to successfully design a twinning-induced plasticity non-equiatomic $Fe_{40}Mn_{40}Co_{10}Cr_{10}$ HEA. By reducing Co, Cr contents and completely removing Ni from CrMnFeCoNi HEA, they discovered a transition of deformation mechanisms from dislocation slip at low strain level to deformation twins plus slip at high strain level and attributed the distinctive behavior at higher strain to reduced SFE in their material. Nano-scale deformation twins, also known as nano-twins have been shown to contribute considerably to strain hardening ability by obstructing dislocation movement and subdividing initial grains into twin-surrounded lamellas [83–91].

2.3.5. *Precipitation strengthening*

Precipitation hardening derived from second-phase particles enables higher strength by interacting with dislocations. Due to the complex composition of HEAs, studies of precipitation strengthening in HEAs remain inconclusive. Hardening effect can be derived from two routes, namely, by-pass and particle shearing mechanisms, which primary rely on size of the precipitate particles. Regarding precipitation hardening in HEAs, due to the high probability of forming simple solution, this observation is rare. Preceding studies have proposed the presence of second phases in $CuCr_2Fe_2NiMn$, $Al_{0.3}CrFe_{1.5}MnNi_{0.5}$ [100] (FCC plus BCC phases), single BCC $Al_{0.5}CrFe_{1.5}MnNi$ [80], $Al_xCrFe_{1.5}MnNi_{0.5}$ [101], single FCC FeCoNiCr [102] and CoCrFeMnNi with addition of titanium [103]. He et al. [104] also reported incremental strength of over 300 MPa contributed by precipitation hardening in $(FeCoNiCr)_{94}Ti_2Al_4$ HEAs.

2.3.6. *Two-phase hardening*

Two-phase hardening can be observed in alloys composed of multiple phases with widely different properties; this can generate a synergy of high strength and excellent ductility. Interestingly, apart from grain-boundary hardening, the nanocrystalline Cantor alloy also promotes phase transformation by providing pathways for atomic diffusion, suggesting that single-phase HEAs can only exist under certain restricted conditions [67]. Phase segregation occurs at grain boundaries and eventually leads to formation of second phase precipitates. Thus, in this case, the strengthening effect caused by a second phase is similar to precipitate hardening. Two of the most common phase transformations observed in HEAs are the FCC to BCC and FCC to HCP transition, which can be activated by either appropriate heat treatment or sufficiently high stress loading. As for its presence in HEAs, superior mechanical properties owing to phase transformations have been proposed for $Co_{20}Cr_{26}Fe_{20}Mn_{20}Ni_{14}$ [105] and FeCoCrNi [106] at cryogenic temperature, CoCrFeMnNi under hydrostatic compression [107] and AlCoCrFeNi [108], etc. Aside from traditional FCC to BCC and FCC to HCP transformation, recent research also uncovered a crystalline to amorphous phase transformation in CoCrFeMnNi alloy achieved by dynamic compressive [109] and quasi-static tensile [110] tests.

3. Mechanical properties

3.1. *Dynamic compression/tensile tests by split-Hopkinson compression bar (SHPB)*

The mechanical response at strain-rates ranging from 10^2-10^4/s is usually investigated by Kolsky's split-Hopkinson bar system [111,112]. In classic split-Hopkinson compression testing, samples are sandwiched between incident and transmitted bars. When the stress wave propagates through the sample, pulse signals are generated and then captured by strain gages attached at the surface of the bars. Regular stress profiles including engineering stress/strain and strain-rate can be derived from pulse signals through following equations:

$$\dot{\varepsilon} = \frac{-2C_0}{L_s}\varepsilon_r(t) \tag{3.1}$$

$$\varepsilon_e = \frac{-2C_0}{L_s}\int_0^t \varepsilon_r(t)dt \tag{3.2}$$

$$\sigma_e = \frac{A_0}{A_s}E_0\varepsilon_t \tag{3.3}$$

where ε_r is the reflected wave signal, ε_t is the transmitted wave signal, L_s is the length of the cylinder specimen, ε_e is engineering strain, σ_e is engineering stress, C_0 is the wave velocity of maraging steel (~5000 m/s), A_0 and A_s are cross-sectional areas for the bar and specimen, respectively.

Application of the Hopkinson bar is not only limited to compression, but also to torsion and tensile tests. The design of the tension testing setup on split-Hopkinson bar system was proposed by Hauser [113], and Lindholm and Yeakley [114]. Chiddister and Malvern [115] developed a high-temperature setup. The split-Hopkinson bar was properly modified for torsion tests by Baker and Yew [116]. The geometry of specimen used in tests can be classified as continuous and discontinuous. The discontinuous specimens include hat-shaped [117–121], double shear [122–124], single/double notch [125–128], compact forced simple shear specimens [129]. Of the other specimens with continuous geometry, the simplest one is the cylindrical specimen.

Shear localization as an undesired deformation mechanism, leading to catastrophic shear failure of materials, has always been found in dynamically deformed specimens. Such failure mechanism has been extensively investigated in metallic materials [120,130–133] and usually been obtained from high strain-rate loading tests, such as split-Hopkinson compression, ballistic impact, drop-weight tower and shock compression. Initiation of shear localization is mainly associated with shear instability which can be expressed by three different terms [134]:

$$d\tau = \left(\frac{\partial\tau}{d\gamma}\right)_{\dot{\gamma},T} d\gamma + \left(\frac{\partial\tau}{\partial\dot{\gamma}}\right)_{\gamma,T} d\dot{\gamma} + \left(\frac{\partial\tau}{\partial T}\right)_{\dot{\gamma},\gamma} \mathrm{dT} \tag{3.4}$$

where first term indicates the work hardening effect, second term represents the strain rate effect on shear stress and third

term represents thermal softening. Based on equation (3.4), the occurrence of instability ($d\tau < 0$) is closely related to the work hardening ability, where high strain hardening rate will impede shear instability and poor strain hardening ability will lead to localization. A critical shear strain γ_c is often used as a representative parameter to determine the critical condition to initialize shear localization. This critical strain has been proposed by Culver [134] and can be expressed as following:

$$\gamma_c = \frac{n\rho C_V}{\beta\left|\frac{\partial\tau}{\partial T}\right|} \tag{3.5}$$

where n is strain-hardening exponent, ρ is density, C_V is specific heat capacity, β is Taylor-Quinney factor. The value of critical strain is always inversely proportional to strain rate and strain-hardening rate and proportional to strain-rate sensitivity [135,136].

In statically deformed specimens, the heat generation rate is surpassed by the heat diffusion rate. However, in dynamically deformed specimens, due to insufficient time for heat dissipation, heat cannot be successfully dissipated, and drastic temperature rise can take place, which is also known as thermal softening effect. The temperature rise due to adiabatic deformation can be written as:

$$dT = \frac{\beta}{\rho C_V}\sigma d\varepsilon \tag{3.6}$$

Normally, the stress-strain response is conveniently predicted with a modification of the classic Johnson–Cook equation:

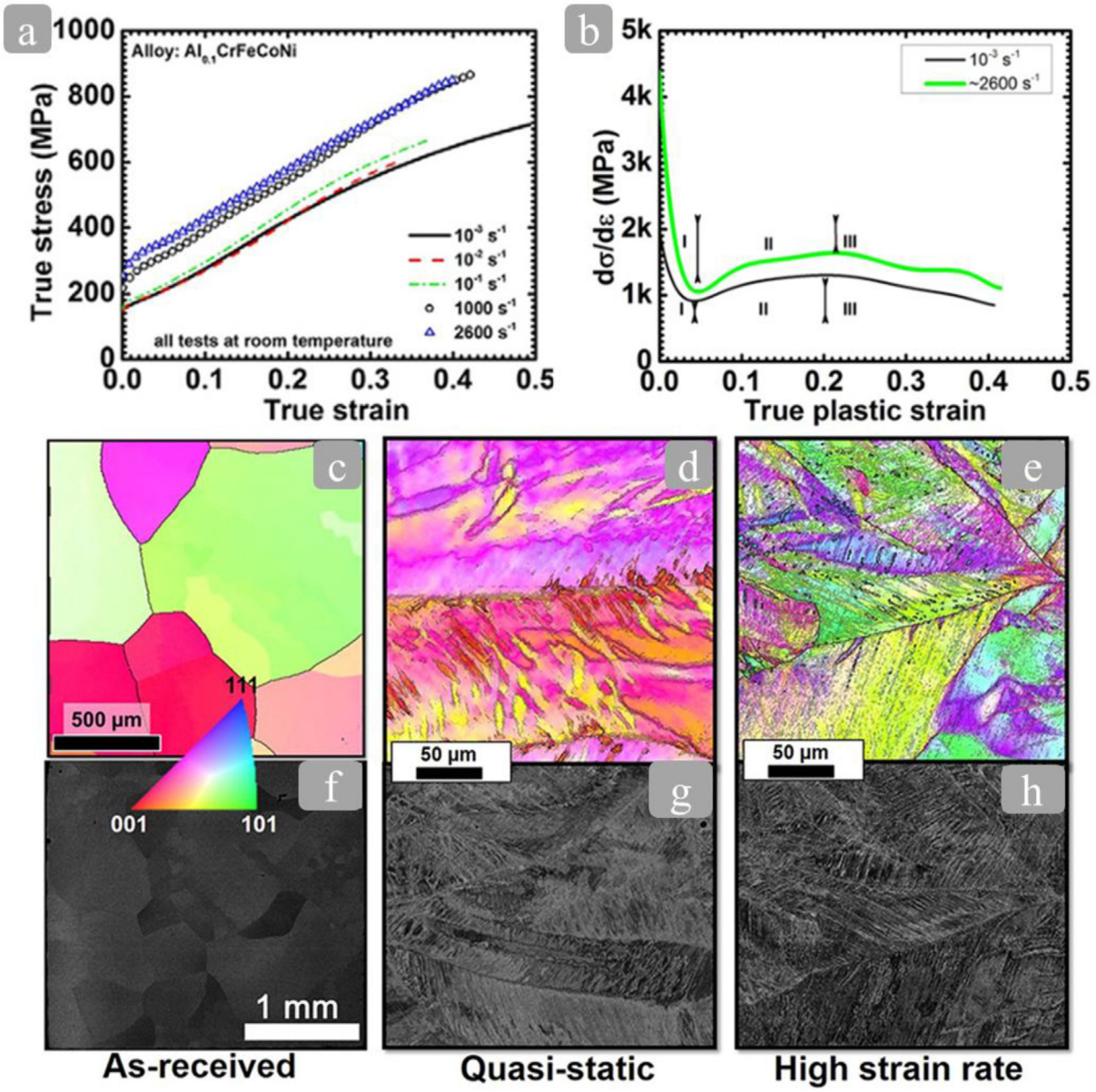

Fig. 5 – (a) True stress vs. true strain curves at different strain rates (10^{-3}, 10^{-2}, 10^{-1}, 1000, 2600 s^{-1}) (b) Plot of strain hardening rate as function of true plastic strain (c)–(e) Electron backscatter diffraction images and their corresponding (f)–(h) Scanning electron microscope for as-received, quasi-statically deformed and dynamically deformed samples [37].

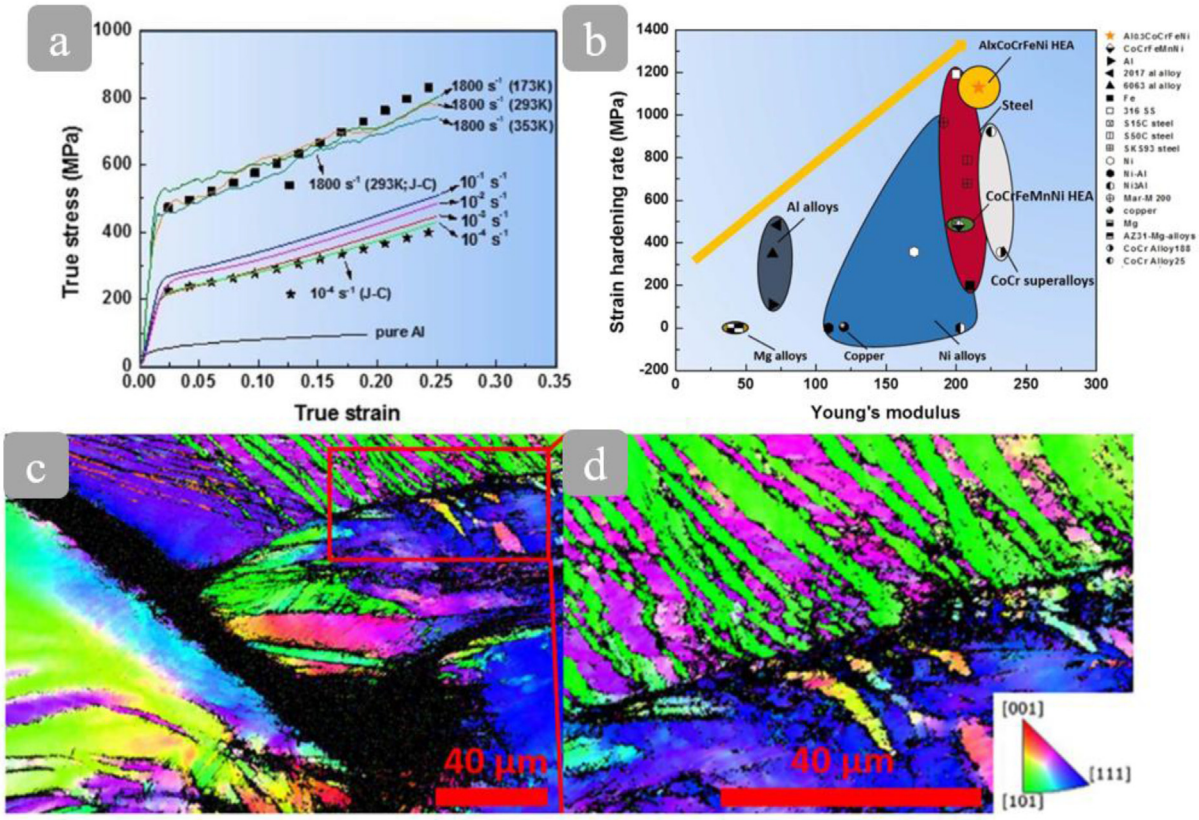

Fig. 6 – (a) True compressive stress vs. true compressive strain curves of the $Al_{0.3}$CoCrFeNi high-entropy alloy at different strain rates with corresponding Johnson–Cook fitting curve. (b) Comparison of strain-hardening ability of $Al_{0.3}$CoCrFeNi HEA with other metallic materials. (c) (d) IPF mapping near deformation tip, showing extensive twins across grains.

$$\sigma = (\sigma_0 + B\varepsilon^n)\left(1 + C\log\frac{\dot{\varepsilon}}{\dot{\varepsilon}_0}\right)\left(\frac{T}{T_r}\right)^A \tag{3.7}$$

where A, B, C, n are experimental-based parameters, T and T_r are testing and reference temperatures, respectively. This modified version of Johnson–Cook equation was proposed by Meyers et al. [137], thereby predicting corresponding temperature as a function of strain, strain-rate, thermal softening, and strain hardening:

$$T = \left[T_r^{1-A} + 0.9(1-A)\varepsilon\frac{1 + C\ln\frac{\dot{\varepsilon}}{\dot{\varepsilon}_0}}{\rho C_V T_r^A}\left(\sigma_0 + \frac{B\varepsilon^n}{n+1}\right)\right]^{\frac{1}{1-A}} \tag{3.8}$$

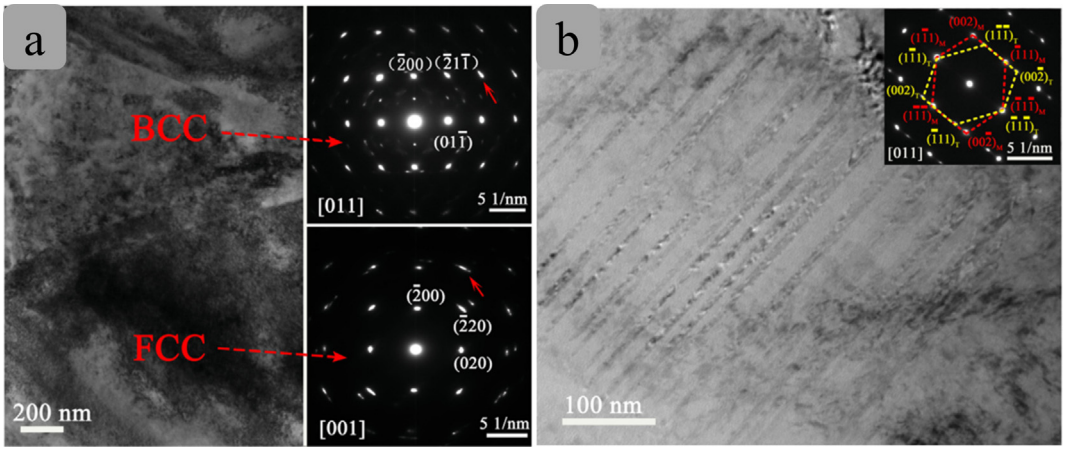

Fig. 7 – (a) Bright field TEM images of the samples deformed at a strain rate of 3600 s^{-1} and the corresponding SAED pattern. (b) The HRTEM image of the deformation twins and corresponding SAED pattern [147].

Continuous development of shear localization can lead to the formation of a banded structure, namely adiabatic shear band, accompanied with softening effect [138]. As the strain-rate keeps increasing, the thermal softening effect becomes more significant. The evolution of shear bands in thermo-viscoplastic materials was studied by Molinari and Clifton [139], and Clifton et al. [135], who presented an idealized model to predict critical condition for shear localization without considering heat conduction, inertia, and elasticity. Ultra-fined/nanocrystalline grains, which result from dynamic recrystallization (DRX), can always be found within shear bands [118,140–142]. Such ultra-fined/nanocrystalline grains were first reported by Meyers and Pak in titanium [142]. DRX is an important microstructural evolution mechanism associated with temperature rise in local domains. Conventional migrational recrystallization theories are no longer suitable for DRX due to significantly shorter deformation time for grain migration. Therefore, equiaxed recrystallized nano-sized grains are usually observed in shear band. Meyers et al. [144] and Hines et al. [143] pointed out that low angle grain boundaries can rotate when subjected to severe plastic deformation. Thus, occurrence of DRX is mainly attributed to elongated dislocation cells which subsequently turn into elongated sub grains. Such mechanism is called rotational recrystallization.

3.1.1. *Al–Cr–Fe–Co–Ni HEAs*

The first ever study on dynamic properties of HEAs was conducted by Kumar et al. [37]. They performed compressive tests on $Al_{0.1}CrFeCoNi$ HEA at both quasi-static (strain rates of 10^{-3},10^{-2} and 10^{-1} s^{-1}) and dynamic conditions (strain rate of 2600 s^{-1}), revealing a stronger strain-rate dependence at the latter condition. Such stronger relationship between strain-rate and yield strength is common for low SFE materials. Under high strain rate loading, dislocation planar glide is governed by more active partial dislocation movement in low SFE materials, and the phonon drag effect on dislocation motion becomes more pronounced. They successfully tuned down the SFE (<20 mJ m^{-2}) in CrFeCoNi by introducing Al. The authors attributed the drastic rise in yield strength, as displayed in Fig. 5(a), to the phonon drag effect and intensified partial dislocation movement. With respect to strain hardening, given higher frequency of partial dislocation activity, twinning prevailed and consistently generated a rising strain hardening rate in stage II, as shown in Fig. 5(b, e, h). Hence, Kumar et al. [37]

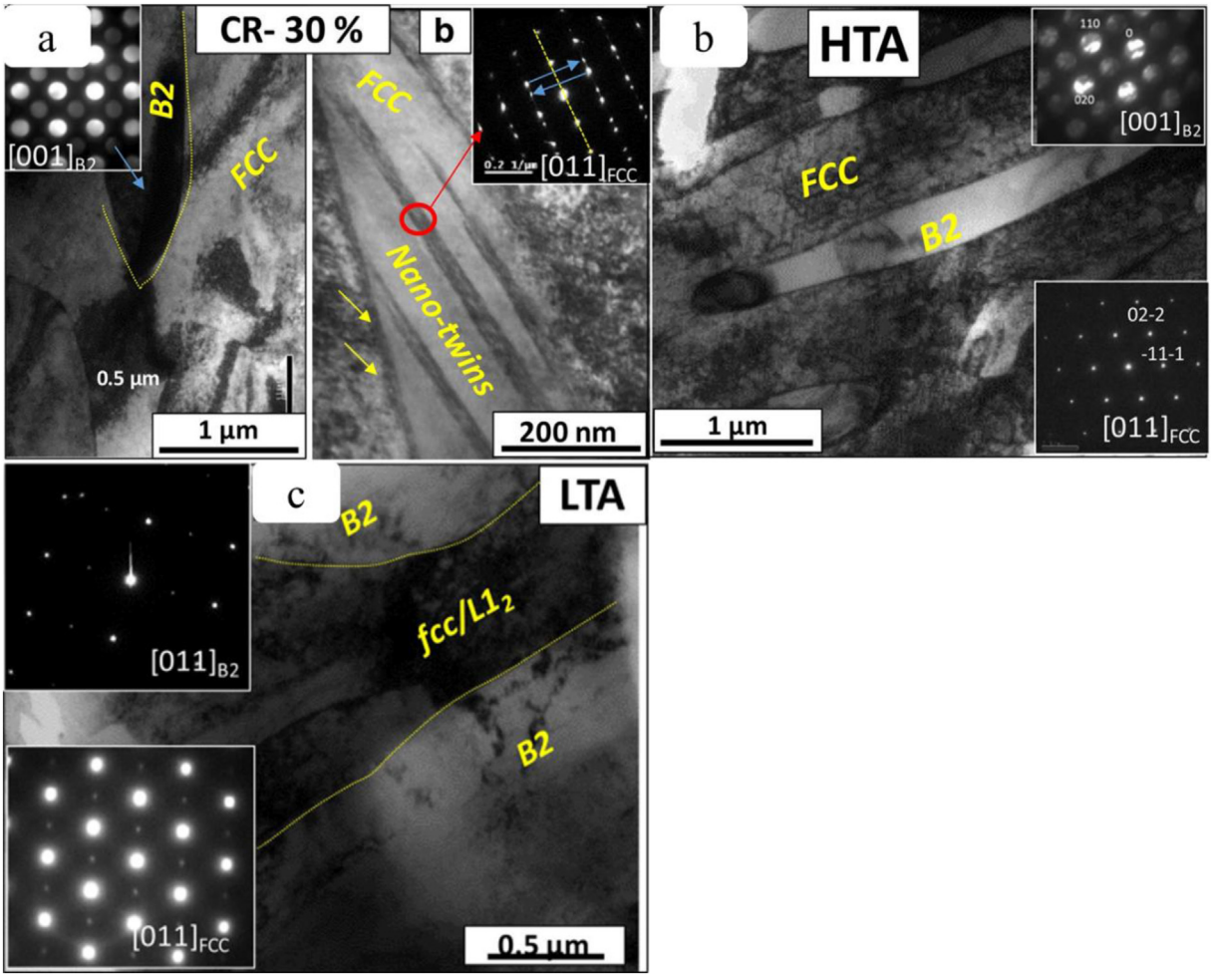

Fig. 8 – Bright field TEM images and corresponding SADE patterns in: (a) as-cold rolled specimen (b) high temperature annealed and (c) low temperature annealed samples [228].

concluded that the excellent work hardening ability at high deformation velocity was primarily derived from deformation mode governed by twinning, which is similar to other low SFE materials.

The dynamic properties of the $Al_{0.3}CoCrFeNi$ HEA were examined by Li et al. [145]. On the basis of Kumar's research, Li and his co-workers investigated similar $Al_xCoCrFeNi$ systems with a higher atomic fraction of Al (~0.3) to achieve an even lower SFE. This work reported a high resistance to shear localization in this material. The stress–strain curves at varying strain-rates and temperatures are illustrated in Fig. 6(a). The modified Johnson–Cook equation defined earlier (Eq. (3.7)), was applied to quantitatively study the shear instability formation in this alloy. By incorporating the experimentally determined strain hardening and thermal softening parameters, a $\frac{d\tau}{d\gamma}$ with a value of 405 MPa could be determined at a shear strain of 1.1. Thus, shear instability was expected to be suppressed under the conditions at which the specimen was tested. However, Tang et al. [146] observed ultra-fine grains as a result of dynamic recrystallization by applying high-pressure torsion with a pressure of 6.0 GPa for 8 revolutions in $Al_{0.3}CoCrFeNi$ alloy. Thus, the suppression of shear localization may also be related to different deformation mode. In addition, higher shear strains and temperatures are needed for the initiation of shear localization. The retardation of localization was mainly attributed to the extensive formation of mechanical twins, as shown in Fig. 6(c) (d), which benefitted from increase of Al content. As illustrated in Fig. 6(b) which compares HEAs with other conventional metallic alloys, at high strain hardening rate (above 1000 MPa). A significantly higher strain-hardening rate than that in coarse grain pure Al (below 500 MPa at strain over 0.05), was established in $Al_{0.3}CoCrFeNi$. Thus, this suggests a great potential to be future candidate of impact-resistant materials.

To produce a comprehensive study of dynamic properties of $Al_xCoCrFeNi$ HEAs, Wang et al. [147] carried out dynamic compression tests on $Al_{0.6}CoCrFeNi$ HEA. In contrast to single FCC phase formation in $Al_{0.3}CoCrFeNi$, the $Al_{0.6}CoCrFeNi$ HEA exhibited a BCC second phase. The dynamic compressive strengths at strain rates of 2800, 3600 and 4000 s^{-1} were 880, 842, 997 MPa, respectively. In addition, this alloy possessed excellent strength and ductility with an ultimate fracture strain approaching 40% at strain rate of 4000 s^{-1}. Therefore, a remarkable work hardening ability was expected to overcome strength-ductility tradeoff. Closely interacting dislocations were observed under TEM, as shown in Fig. 7(a). Under high-speed deformation, the dislocation moving pattern tends to convert from the planar plus wavy glide to wavy glide [148], where predominantly wavy glide is always coupled with the formation of dislocation cells. Operation of wavy glide rendered considerable resistance to dislocation movement, thereby contributing to elevated flow stress of this alloy. In addition, due to disparate stacking fault energy between FCC and BCC phase, profuse deformation twins were observed in the former phase, as shown in Fig. 7(b), while only dislocations were present in the latter phase. Therefore, the operation of multiple deformation modes such as forest dislocation strengthening, solid solution strengthening, and deformation twins leads to remarkable ability to resist the strength-ductility trade-off.

The dynamic behavior of $Al_xCoCrFeNi$ with highest Al content was studied by Gangireddy et al. [228]. They examined the dynamic properties of $Al_{0.7}CoCrFeNi$ alloys comprised of FCC matrix plus B2 lamellar structure, which has been discovered by a preceding study [149]. By conducting high (1100 °C) and low (580 °C) temperature annealing treatments, distinctive properties were revealed: while high temperature annealed alloy possessed higher work hardening ability, the low temperature annealed alloy had a higher yield strength. The low temperature treatment contributed to inferior ability for dislocation recovery compared to one annealed at high temperature, thereby promoting formation of ordered $L1_2$ precipitation, as shown in Fig. 8(c). The difference in mechanical properties between B2 and FCC phases leads to inhomogeneous deformation, whereby the internal domain of B2 provides higher dislocation storage capability [150,151] and the softer primary FCC phase can accommodate greater plasticity. In general, the distinct dynamic behavior is mainly the result of different degrees of dislocation recovery raised by different annealing temperatures.

The first investigation on dynamic properties of $AlCoCrFeNiTi_x$ was reported by Jiao et al. [152]. Unlike classic AlCoCrFeNi with modification only in Al content, they introduced Ti. The dynamic compressive results of Ti_0, $Ti_{0.2}$, and $Ti_{0.4}$ alloys are revealed in Fig. 9(a–c), suggesting that the yield strength was proportional to the atomic ratio of Ti, where Ti_0 alloy exhibits the lowest yield strength of 1546 MPa and $Ti_{0.4}$ exhibits highest yield strength of 2090 MPa. The enhanced compressive strength was attributed to the larger atomic radius of Ti atoms leading to severe lattice distortion and significant enhancement of the solid solution strengthening effect. Their results are summarized in Fig. 9(d) and compared with Ni-based superalloys and Bulk Metallic Glasses, $AlCoCrFeNiTi_x$ exhibited a high ultimate strength while maintaining a relatively large strain to failure, which is attributed to solid solution strengthening, phase variation, thermally activated mechanisms [153–155], and the phonon drag effect.

Besides the conventional AlCoCrFeNi system that only contains metallic elements, Wang and his co-workers [156] designed a $(Al_{0.5}CoCrFeNi)_{0.95}Mo_{0.025}C_{0.025}$ HEA. Preceding research [157,158] reported that the addition of Mo and C could enhance mechanical properties of $Al_{0.5}CoCrFeNiMo_x$ HEAs by forming a (Cr, Mo)-rich σ phase and promoting precipitation hardening. The yield strengths of $(Al_{0.5}CoCrFeNi)_{0.95}Mo_{0.025}C_{0.025}$ deformed at strain rates of 550, 1300, 2200 and 3000 s^{-1} and were 754, 878, 958, and 1057 MPa, respectively. In comparison with $Al_{0.3}CoCrFeNi$ HEA [145], a much higher strain hardening rate was observed in $(Al_{0.5}CoCrFeNi)_{0.95}Mo_{0.025}C_{0.025}$, but pronounced shear banding was found. This contradictory phenomenon was ascribed to dissolved Mo atoms that slow down thermal diffusion. Hereafter, thermal softening was benefitted from hindered heat diffusion, and promoted shear banding.

3.1.2. *Co–Cr–Fe–Mn–Ni HEAs*

Surprisingly, the classic CoCrFeMnNi (Cantor alloy) is the first ever discovered HEA but is not the first HEA to be examined dynamically. Its dynamic compressive properties were investigated by Park et al. [159] in 2017. The yield strength under dynamic conditions was reported to be 590, 650,

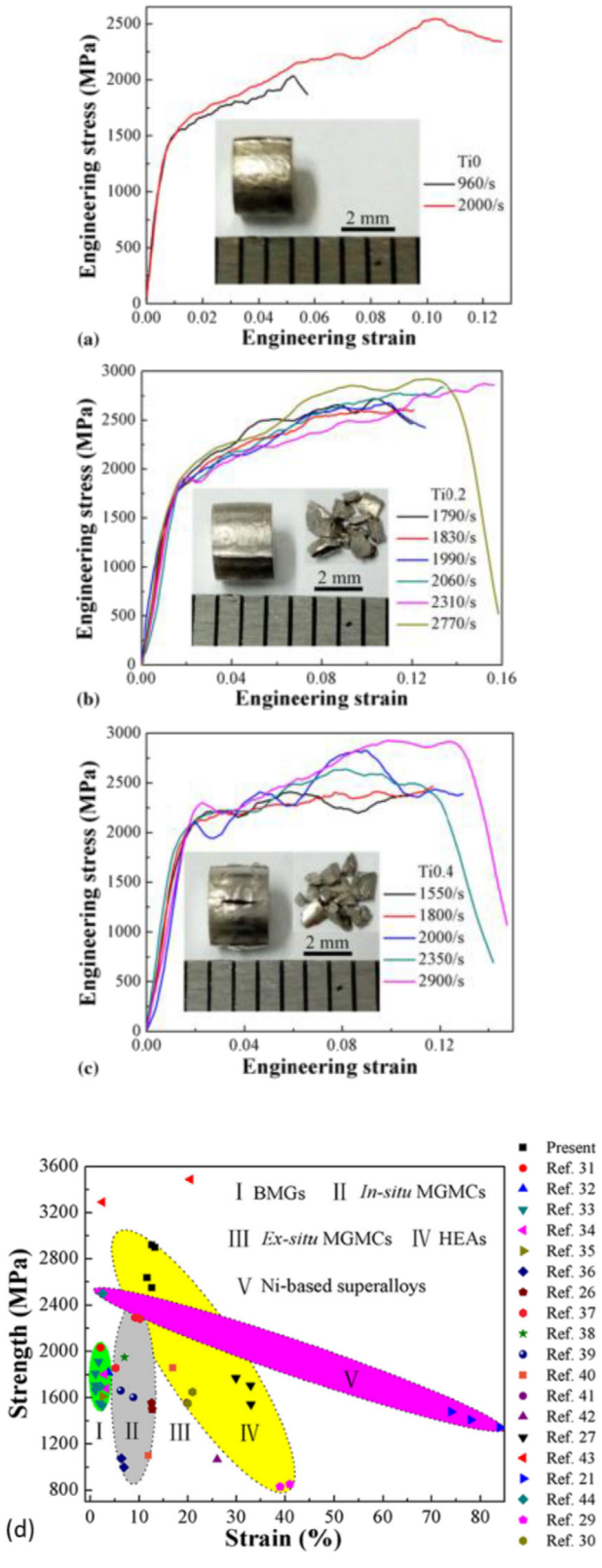

Fig. 9 – Dynamic compressive engineering stress–strain curves of Ti_0 (a), $Ti0_{0.2}$ (b), and $Ti_{0.4}Ni$ Al (c) alloys. (d) Ultimate strength as a function of fracture strain for various materials, under dynamic loading [152].

680 MPa at strain rates of 3000, 3500, 4700 s^{-1}, respectively. Fig. 10 shows the Inverse Pole Figure (IPF) maps in the plane of compression and transverse directions for quasi-statically and dynamically deformed specimens. Greater inhomogeneity of strain can be observed in the latter. The strain hardening rate derived from the dynamic stress vs. strain curve, as shown in Fig. 10(b), can be divided into four stages (A, B, C, D), corresponding to steep drop of hardening rate caused by the elastic–plastic transition, slow linear decrease caused by dislocation glide coupled with dynamic recovery [160], steady hardening rate related to formation of mechanical twins, and, finally, steady decrease of hardening rate. Profuse twins were observed under both quasi-static and dynamic conditions. A rather higher density of twins was observed in dynamically deformed samples; this was similar to what was reported in $Al_{0.1}$CrFeCoNi alloy [37]. As the alloy was further strained, a gradually decreasing work hardening rate was overcome by thermal softening, which led to shear instability, as shown in Fig. 10(e, f, i, j). Contrary to conventional FCC alloys with high activation volume, such as Cu (200–2000 b^3), α-brass (200–400 b^3), an exceptionally low activation volume (~10 b^3), indicative of extensive twinning, was measured for CoCrFeMnNi alloy. Thereby, profuse twins contribute to the remarkable work hardening ability of this alloy, resembling $Al_{0.3}$CoCrFeNi [145].

Li et al. [161] have also examined the dynamic properties of CoCrFeMnNi HEA, but prepared by a different method, spark plasma sintering (SPS) method, and focusing on adiabatic shear localization. Unlike in the arc-melting method, alloys prepared by SPS are likely to contain voids, leading to residual porosity and lower strength. They obtained a high strain hardening rate (~1100 MPa) at a strain of 0.2 when the alloy was deformed at strain rate of 1600 s^{-1}. Moreover, through imposed localized shear deformation in hat-shaped specimens, they successfully established the critical shear strain (~7) to induce shear banding (Fig. 11(b)). The retardation of shear localization suggested a strong work hardening ability, which involved twinning and strong dislocation planar glide. Within the shear band, they observed a similar subgrained structure to the one reported by Park [159], as shown in Fig. 11(c). This grain refinement is due to occurrence of dynamic recrystallization. Fig. 11(d) shows that, compared with titanium [137], Ti–6Al–4V alloy [162], AISI 1006 steel [47], brass [47]and copper [120], the Cantor alloy has the best ability to resist the softening effect in the temperature range of 200 K–1000 K. In addition, some nanotwins were found within those nanograins, indicating that they could still exhibit plasticity at elevated temperature.

Wang et al. [163] provided an interesting insight to dynamic properties of as-cast CoCrFeMnNi HEA. Without homogenization treatment, this alloy showed a dendritic structure. At high strain rate, unlike preceding studies on annealed alloys [159,161], as-cast alloy displayed unique "serration behavior", which can be seen as tooth-like flow stress curves in Fig. 12(a). Zhang et al. [164] reported that the serration behavior is more pronounced at elevated temperatures and under dynamic deformation. They ascribed this continuously fluctuating stress to the formation of a heterogeneous structure, namely, deformation bands, as

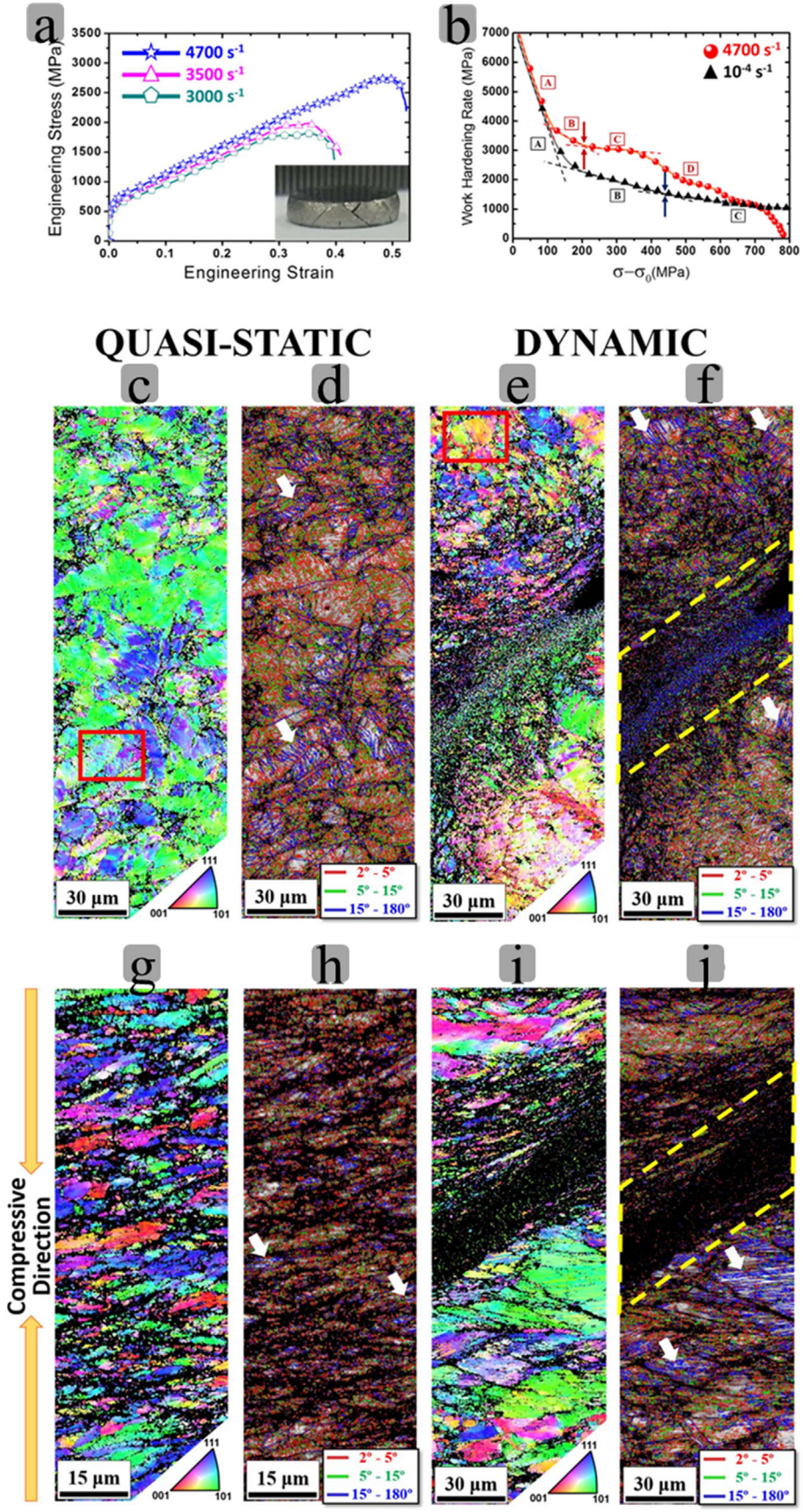

Fig. 10 – (a) Engineering stress vs. engineering strain curves under dynamic compression (b) Strain hardening rate as a function of true plastic strain. IPF maps one the plane of compressive direction (c)–(f) and transverse direction (g)–(j) (c, d, g, h) at 10^{-4} s^{-1} (e, f, i, j) at 4700 s^{-1} [159].

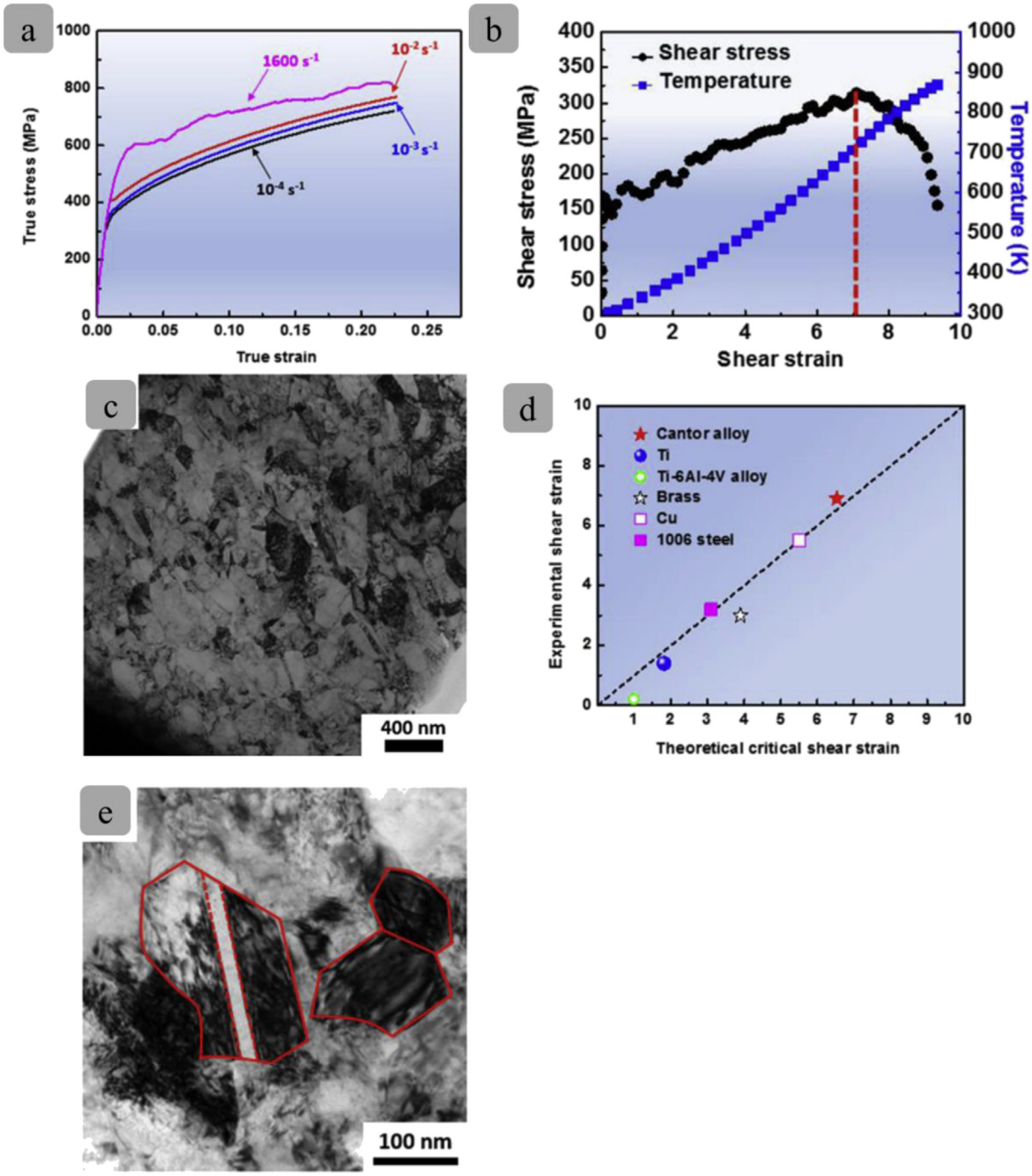

Fig. 11 – (a) Stress vs. strain curves at different strain; (b) shear stress as function of shear strain and corresponding temperature rise within the shear band; (c) TEM micrograph showing recrystallized grains with dislocations and twins; (d) Critical shear strain for shear localization for multiple materials (Cantor alloy, Ti, Ti–6Al–4V alloy, brass, copper and 1006 steel); (e) Twin boundaries within recrystallized grain [161].

displayed in Fig. 12(b and c). Deformation bands in this case generate the Portevin-Le Chatelier effect [165–168]. The serrated flow stress was a result of interaction between moving dislocations and deformation bands and could become more evident at higher strain rate due to larger amount of such heterogeneous structure, as illustrated in Fig. 12(c and d). Besides the alloy prepared by the traditional arc melting method, Wang et al. [169] also extended their work to serration behavior of CoCrFeMnNi HEA prepared by SPS. In contrast to their previous work [163], where serrated flow stress resulted from formation deformation bands, here they ascribed it to secondary Cr-rich oxide phase. The

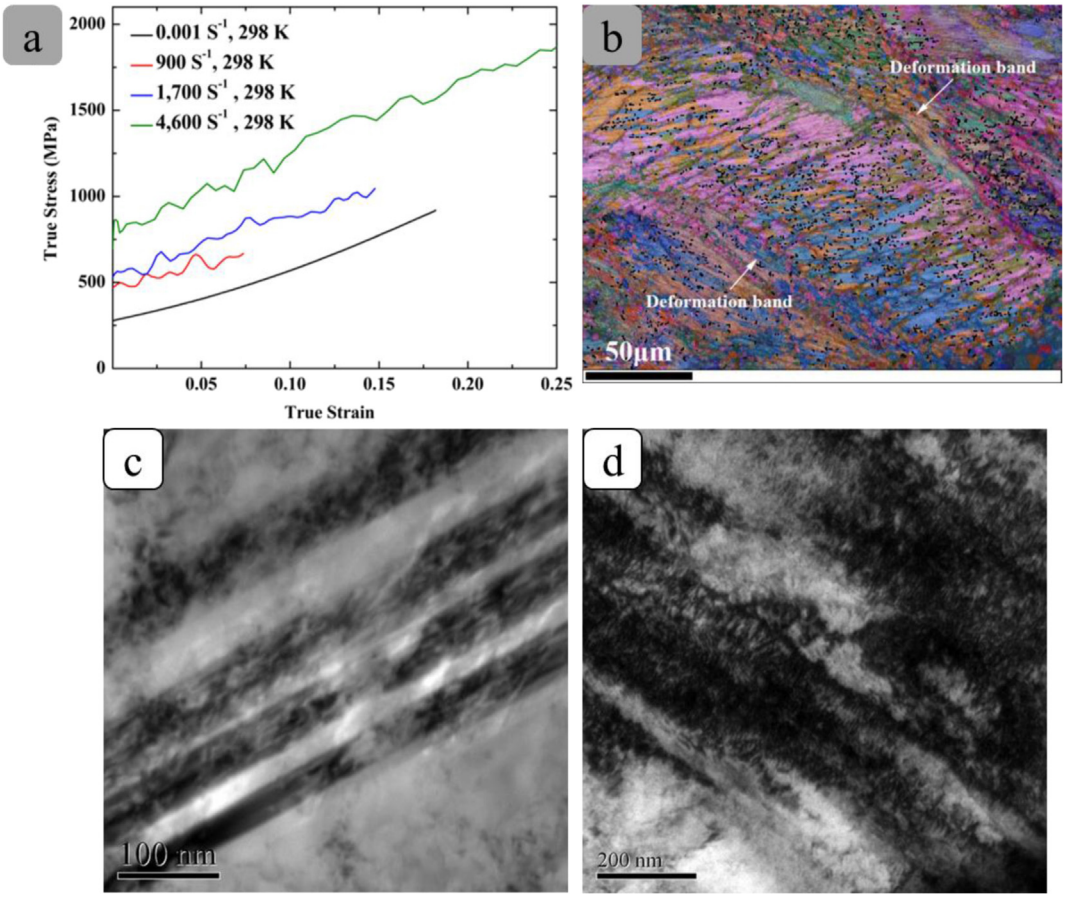

Fig. 12 – (a) Compressive true stress vs. true strain curves for CoCrFeMnNi HEA at different strain rates. (b) The Euler plus band contrast image of the deformed specimen at the strain rate of 4600 s^{-1}. Bright field TEM micrograph of specimens deformed at strain rates of (c)1700 s^{-1}, (d)4600 s^{-1} [163].

dispersed Cr-rich particles within matrix provided a strong pinning effect for dislocations movement by generating the Portevin-Le Chatelier effect (Fig. 13). The role of secondary particles was quite comparable to deformation bands, in terms of slowing down dislocation movement. Each time a dislocation was pinned and unpinned by second phase particle it causes an increase and decrease in stress [164].

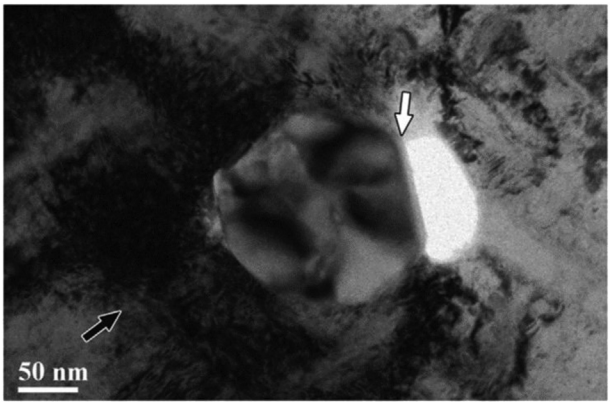

Fig. 13 – The bright field TEM micrograph showing pinned dislocations at the boundary of secondary phase particles [164].

On the basis of Park's and Li's work, Tsai et al. [54] proposed a transition of deformation mode when CoCrFeMnNi alloy was subjected to a high strain rate of 9000 s^{-1}. As mentioned before, dynamic deformation of CoCrFeMnNi alloy seems to be governed by dislocation glide. However, at a strain rate of 9000 s^{-1}, kinked twins were observed, suggesting a deformation mode dominated by twinning, as shown in Fig. 14. Such alteration of deformation mode, generating an enhanced strain hardening rate coupled with rising strain rate, makes further study of CoCrFeMnNi alloy deformed at ultra-high strain rate (shock compression) more interesting.

To provide further insight to the effect of adiabatic heating on mechanical response of CoCrFeMnNi, Soares et al. [170] reported that the Taylor-Quinney coefficient was not equal to 0.9 as was previously assumed for the determination of temperature rise at high strain rate for metallic materials. The Taylor-Quinney coefficient is a parameter denotes efficiency of plastic work converted into heat. This coefficient can be classified into two components: integral beta (β_{int}) and differential beta (β_{diff}), which correspond to how much strain energy is converted in to heat and how much mechanical energy is converted into heat, respectively; they can be expressed as:

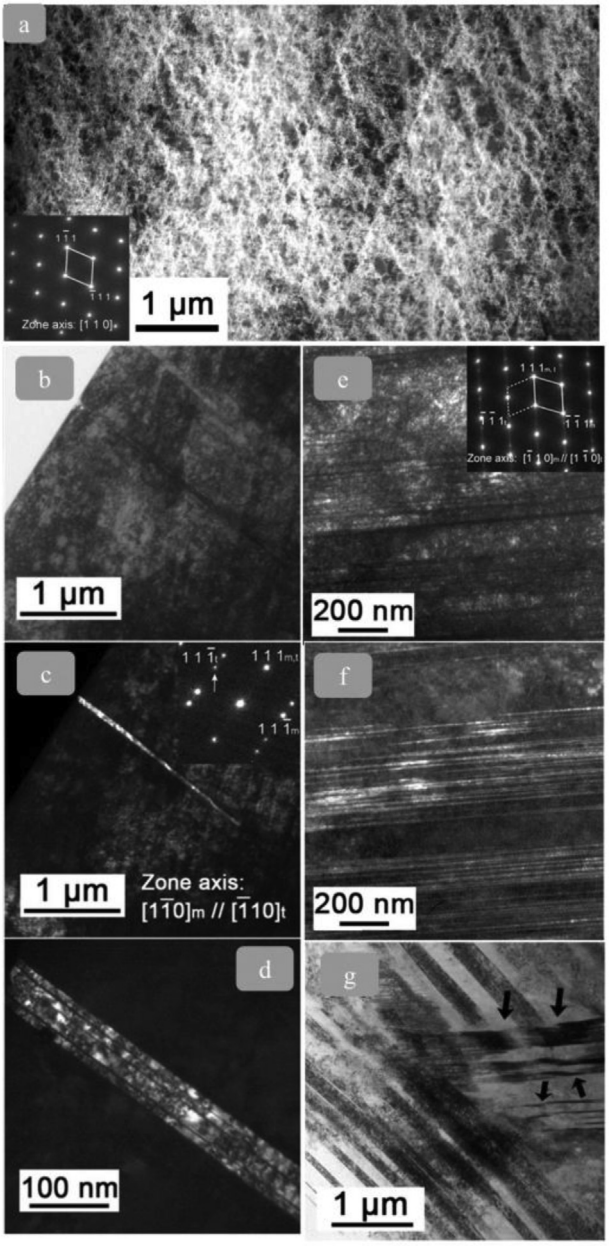

Fig. 14 – (a) TEM micrograph of 40% strained specimen at a strain rate of 3 × 10^3 s^{-1} (b,e) Bright field images of deformation twins present at the strain rate of 6 × 10^3 s^{-1} and 9 × 10^3 s^{-1}, respectively (c,d) dark-field image of bundle of twins in sample deformed at strain rate of 6 × 10^3 s^{-1} (f,g) Twin–twin interaction with kinked structures in specimen deformed at strain rate of 9 × 10^3 s^{-1} with 40% strain [54].

$$\beta_{int} = \frac{\rho C_p \Delta T}{\int dW_p} \tag{3.9}$$

$$\beta_{diff} = \frac{\rho C_p \dot{T}}{\dot{W}_p} \tag{3.10}$$

where C_p is heat capacity, dW_p is the increase in plastic work, ρ is density, T is temperature, $\dot{T}$ and $\dot{W}_p$ are differentials of plastic work and temperature with respect to time. Fig. 15(a and b) reveals β_{int} and β_{diff} as a function of strain at different strain rates. The authors discovered that the adiabatic heating in specimens deformed at 1,750, and 2800 s^{-1} were quite similar and their corresponding β exhibited certain degree of plastic strain dependence.

Apart from most common dynamic test performed by high strain rate compression, Qiao et al. [171] investigated the strain rate dependent microstructural evolution of CoCrFeMnNi via split Hopkinson tensile bar (SHTB) at a strain rate of 7000 s^{-1}. Distinct fracture behaviors were found under different loading conditions, as shown in Fig. 16(a and b), indicating a typical ductile and ductile plus brittle fracture mode in statically and dynamically deformed specimens, respectively, which is suggestive of a transition of fracture mode. Such transition of fracture mode has also been observed in Al_xCrMnFeCoNi alloy by Cao and his co-workers [172]. Similar to CoCrFeMnNi subjected to dynamic compression [159,161], dislocations and twins prevailed in dynamically tensioned specimens, as illus-

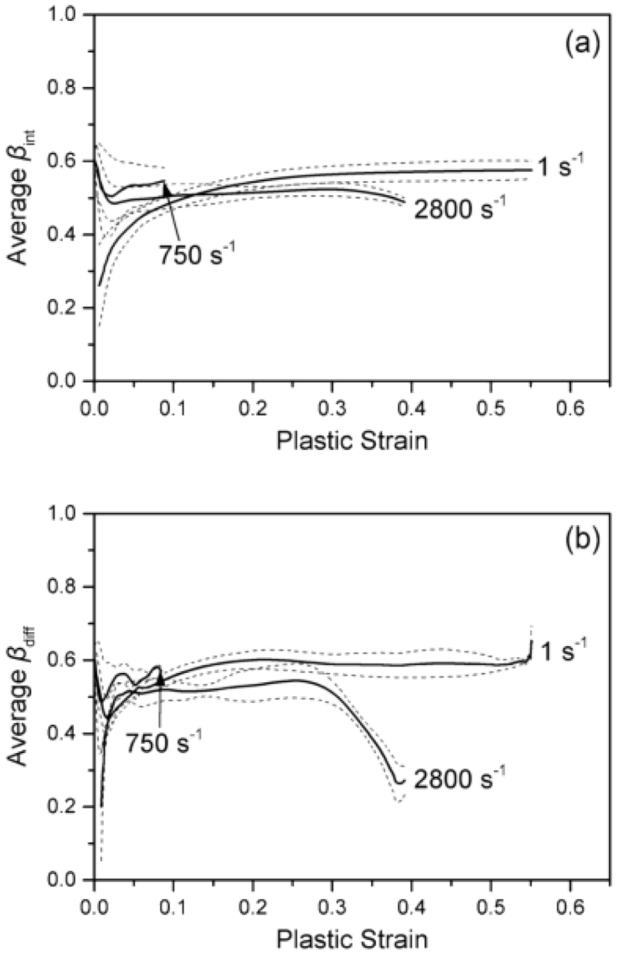

Fig. 15 – (a) Integral β and (b) differential β diff as a function of true strain for the CoCrFeMnNi high-entropy alloy under different strain rate (1 s^{-1}, 750 s^{-1}, 2800 s^{-1}) [170].

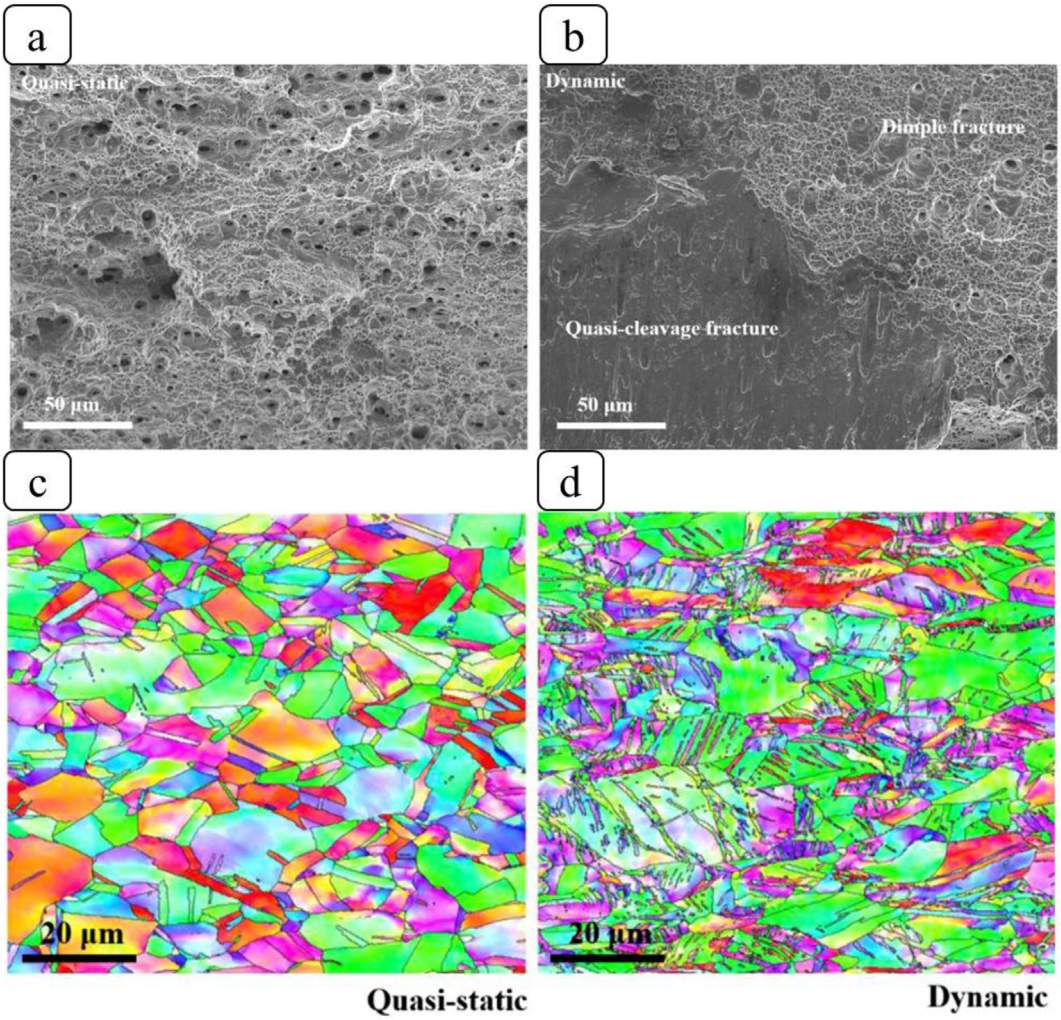

Fig. 16 – SEM micrographs of the fracture morphology for (a) quasi-statically deformed and (b) dynamically deformed specimens. EBSD micrograph of (c) statically deformed specimen at strain of 0.34 and (d) dynamically deformed specimen at strain of 0.57 [171].

trated in Fig. 16(c and d), in contrast to the statically deformed one. The differences in deformation structures cause alteration of fracture from purely ductile to a mixture of ductile/brittle at high strain rates.

Amorphization is most often obtained by two routes in metallic materials: rapidly decreasing temperature to below glass transition temperature T_g or introducing structural/chemical disorder. Recently, a large amount of emphasis has been put on solid-state amorphization (SSA) achieved by severe plastic deformation [173,174]. It is known that accumulation of defects can eventually lead to amorphization. Amorphization in HEAs is being widely studied to broaden their applications in the field of advanced nuclear materials, corrosion and oxidation resistant materials, but is rarely observed experimentally.

Outside of conventional deformation modes of dislocation glide, twinning, microbanding, Zhao et al. [109] reported the formation of an amorphous phase in Cantor alloy achieved via dynamic compressive tests, suggesting an unprecedented deformation-induced amorphization. Associated with amorphization, vast amounts of crystalline defects such as stacking faults, twins and HCP phases have also been observed in dynamically deformed specimens, as shown in Fig. 17(a–e). In order to activate the FCC to HCP phase transition, the required driving force $G_{HCP} - G_{FCC}$ can be established as a function of stacking fault energy γ_{SF}:

$$\frac{\gamma_{SF}}{2b} = G_{HCP} - G_{FCC} \tag{3.11}$$

Such driving force needs to be fulfilled by generating defect energy G_d, which can be expressed as following:

$$G_d \sim \frac{\rho G b^2}{2} \tag{3.12}$$

where ρ is defect density. Combining Equation (3.11) and equation (3.12), they predicted a critical value of $\rho \sim 8 \times 10^{15} m^{-2}$, which was achievable by dynamic loading, to initiate phase transformation. With ongoing plastic deformation, the severely deformed FCC and HCP can be further converted into

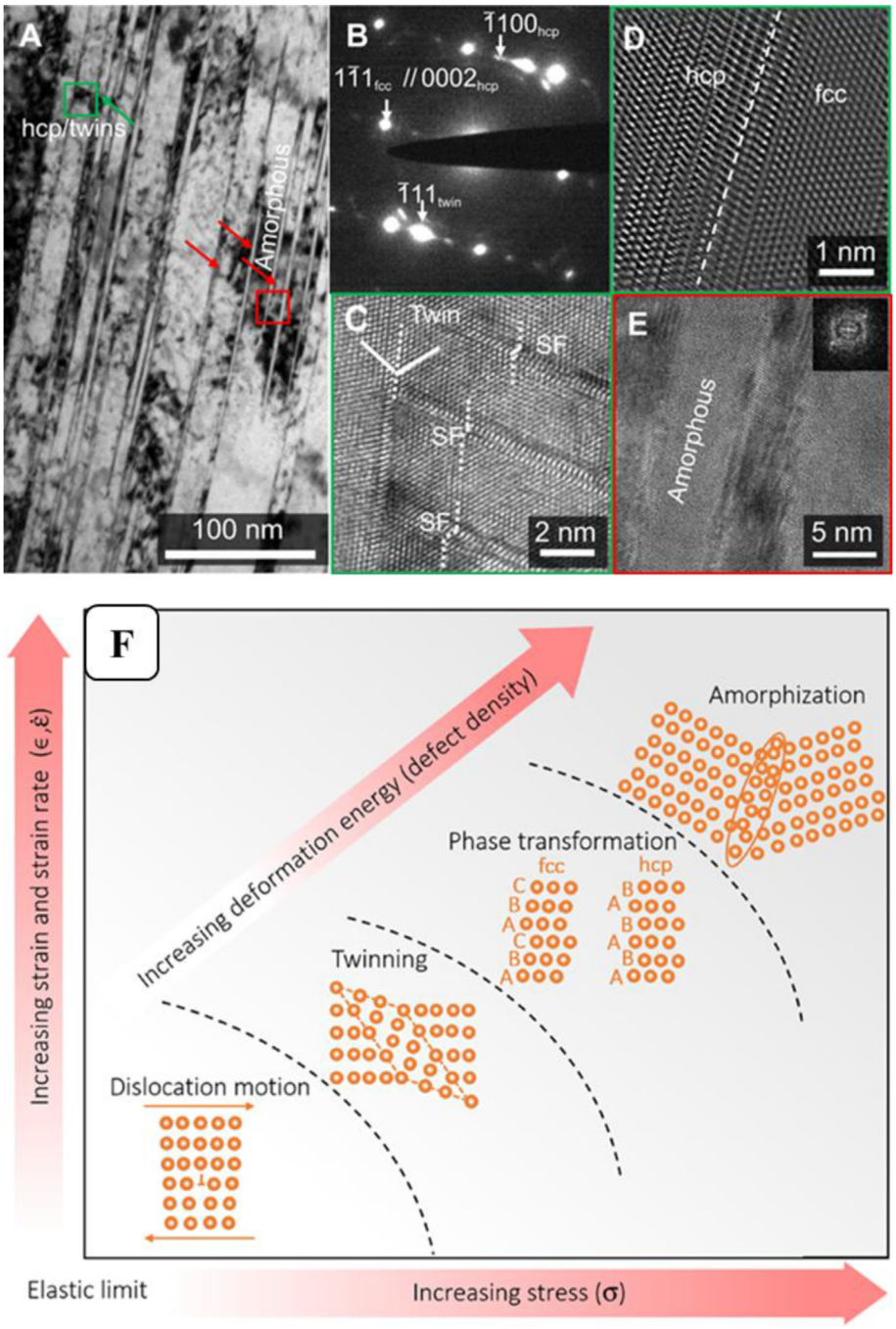

Fig. 17 – (a–e) TEM micrograph of the CoCrFeMnNi HEA subjected to dynamic compression/shear, showing the formation of deformation twins, HCP and amorphous phases. (f) Microstructural evolution of CoCrFeMnNi HEAs subjected to increasing stress and strain rate [109].

an amorphous phase, due to continuously rising defect concentration. In addition, the amorphous domains located favorably at the intersections of HCP and twin packets. A relationship between shear strain and volume fraction of amorphous phase was accordingly proposed [109]:

$$f_a = K[1 - \exp(-\alpha\gamma)]^n \tag{3.13}$$

where K is a constant related to various factors (stacking fault energy, volume fraction of HCP martensite in the deformation packets, and so on), $1 - \exp(-\alpha\gamma)$ is a term that represents fraction of deformation bands and γ is shear strain. Accordingly, the rising defect density was coupled with increasing fraction of deformation bands, which had previously been found in as-cast Cantor alloys [163], leading to the propagation

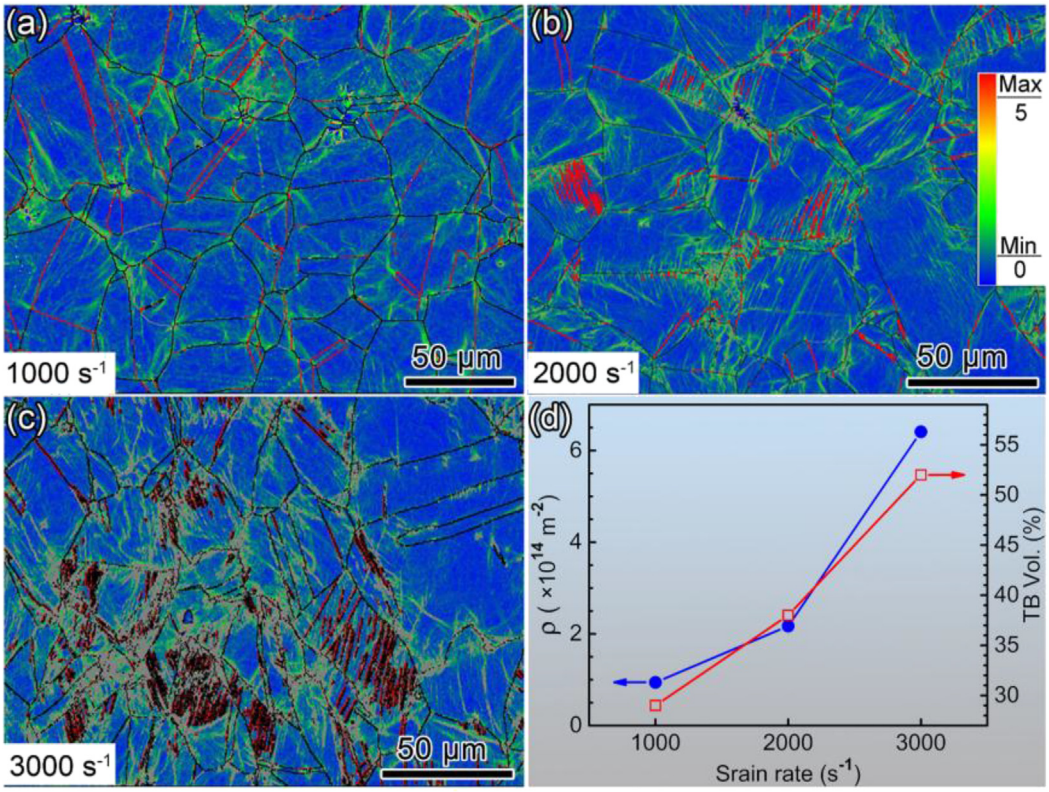

Fig. 18 – (a–c) EBSD local misorientation maps of the $Cr_{26}Mn_{20}Fe_{20}Co_{20}Ni_{14}$ HEA undergoing strain rates of (a) 1000 (a), (b) 2000 and (c) 3000 s^{-1}, respectively. The twin boundaries are indicated by red lines. (d) Estimated dislocation density (ρ) and volume fraction of twin boundaries as function of strain rates [175].

of amorphization. The authors conclude that as flow stress increased, in addition to the common deformation mechanisms (dislocation motion, twinning, phase transformations), previously reported in CoCrFeMnNi HEA, a newly discovered amorphization was added. This renders a remarkable strain hardening ability under dynamic conditions; the corresponding microstructural evolution is plotted in Fig. 17(f).

Other than investigations on equiatomic CoCrFeMnNi HEA, a systematic study on dynamic properties of non-equiatomic $Cr_{26}Mn_{20}Fe_{20}Co_{20}Ni_{14}$ alloy was performed by Jiang et al. [175]. Preceding studies [176] suggested that this alloy possessed a low stacking fault energy of 24 mJ m^{-2} and synergy of excellent strain hardening ability and considerable ductility (maximum strain: 73%) at quasi-static strain rate. They subjected the alloy to dynamic compression at three strain rates (1000, 2000 and 3000 s^{-1}). Noteworthy that continuously increasing flow stress was obtained at the three strain rates (1000, 2000 and 3000 s^{-1}), indicative of a remarkable strain hardening ability at various loading conditions. The local misorientation map shown in Fig. 18 reveals that the volume fractions of twins and stacking faults increase with strain rate. The highest temperature rise caused by adiabatic deformation was estimated to be 64.7 K, which was far from the recrystallization temperature (640 K) of this alloy. Thus, no shear band was observable under TEM. In addition, a smaller activation volume (11 b^3) was found in the present alloy, compared with CoCrFeMnNi HEA (76.8 b^3 [177]). Profuse twins and twin-dislocation reactions were attributed to such low activation volume, which showed a good agreement to previously reported value for twin-dislocation reactions (1–100 b^3 [177]). Moreover, the low stacking-fault energy of this alloy contributes to restricted cross-slip and dislocation climb and increasing density of stacking faults, thereby promoting dislocation and stacking fault strengthening. Therefore, the authors conclude that increasing strain rate from 1000 s^{-1} to 3000 s^{-1} facilitated an evolution of deformation mechanism from dislocation glide to stacking faults plus nano-twinning, then eventually to dense dislocation arrays plus nano-twin bundles, which resemble the CoCrFeMnNi HEA deformed at increasing strain from 3000 s^{-1} to 9000 s^{-1} [54]. This synergy of multiple deformation mechanisms guarantees a retained hardening ability and retards shear localization.

Accordingly, the study of the classic Cantor alloy has been extendedly to strain rates ranging from 1000 s^{-1} to 9000 s^{-1}. A relevant question is: how would the addition of a sixth metallic element change properties of Cantor alloy at high strain rates? Cao et al. [172] examined the dynamic tensile behavior and developed a microstructural evolution of $Al_xCrMnFeCoNi$ (x = 0, 0.4, 0.6) HEAs. It was revealed that the dynamic tensile strength was proportional to the fraction of Al, which is mainly due to the formation of B2 precipitates (Fig. 19(a and b)). The interphase boundaries between B2 precipitates and FCC matrix, shown in Fig. 19(c)–(e), capture large amounts of dislocations and provide a strong boundary strengthening effect. Increasing

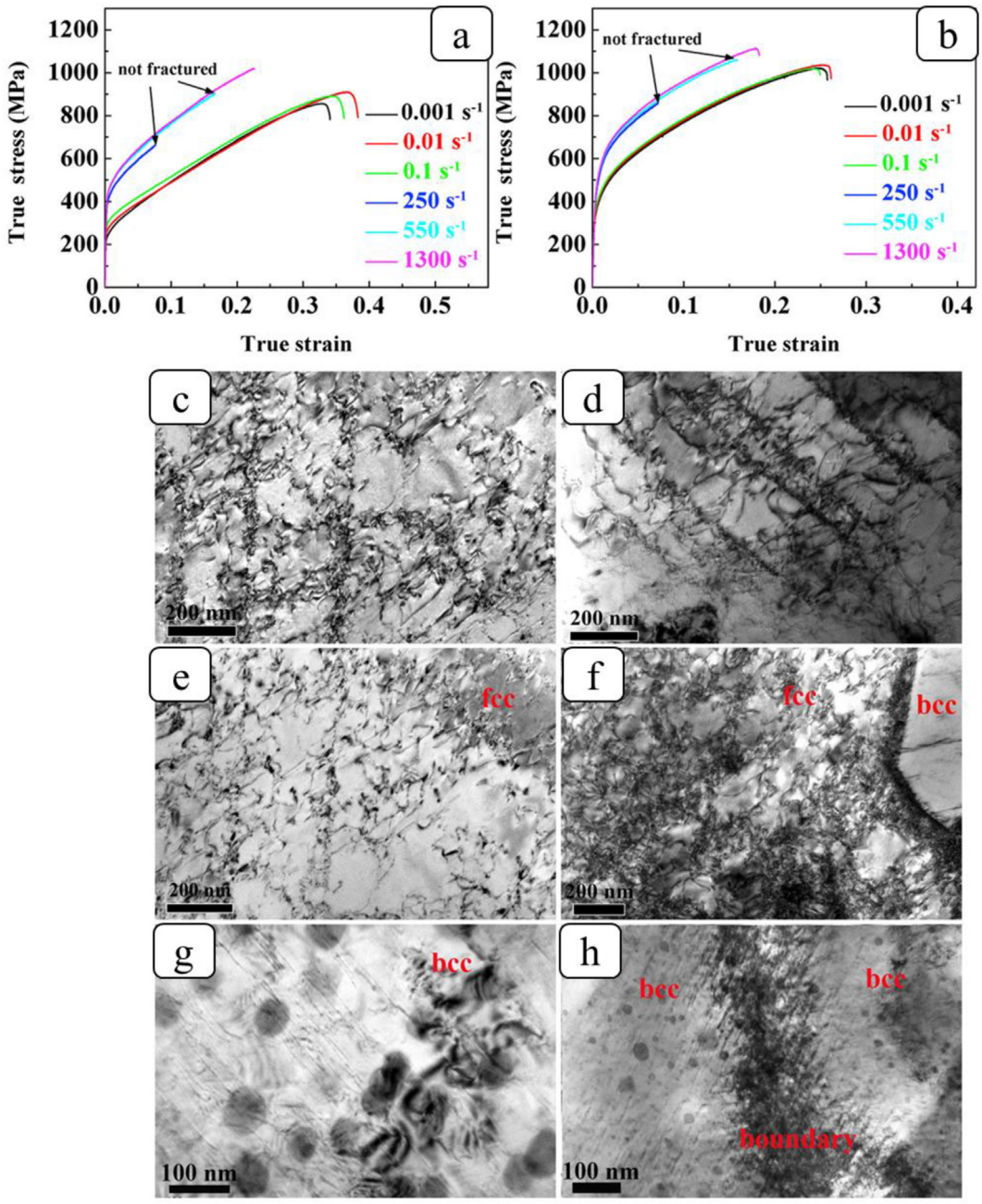

Fig. 19 – Dynamic compressive stress strain curves of (a) $Al_{0.4}CrMnFeCoNi$ (b) $Al_{0.6}CrMnFeCoNi$ alloys. (c) TEM micrographs of dislocation configuration of (c–e) $Al_{0.6}CrMnFeCoNi$ tested at strain rate of 10^{-3} s^{-1} (c,d,e) and 1300 s^{-1} (f,g,h) [172].

the fraction of Al not only promoted formation of precipitates but also restrained grain growth of the matrix phase, leading to considerably refined grains in $Al_{0.6}CrMnFeCoNi$. In comparison with CoCrFeMnNi [178], $Al_{0.4}CrMnFeCoNi$ exhibited small activation volume (10–24 b^3), close to the one reported for $Cr_{26}Mn_{20}Fe_{20}Ni_{14}$ [175], indicative of intensive dislocation motion over obstacles raised by solute atoms. In addition, the $Al_{0.4}CrMnFeCoNi$ revealed a higher strain rate sensitivity ($m = 0.039–0.048$) in comparison with $Al_{0.6}CrMnFeCoNi$, which resulted from the positive relationship between Al content and activation volume. Thus, the authors concluded that the high strength of $Al_{0.6}CrMnFeCoNi$ was chiefly due to the multiple strengthening mechanisms, including precipitation hardening, solid solution strengthening, and boundary strengthening.

3.1.3. *Refractory HEAs*

Although FCC HEAs have received a vast amount of attention due to their excellent mechanical properties at relatively low temperatures, the inherently low melting points of their constituent elements make them less desirable for application in a wider temperature range. For instance, many aerospace materials require exposure to extremely high temperatures and require sufficiently high strength to bear external dynamic loading. For the time being, Ni-based superalloys are widely

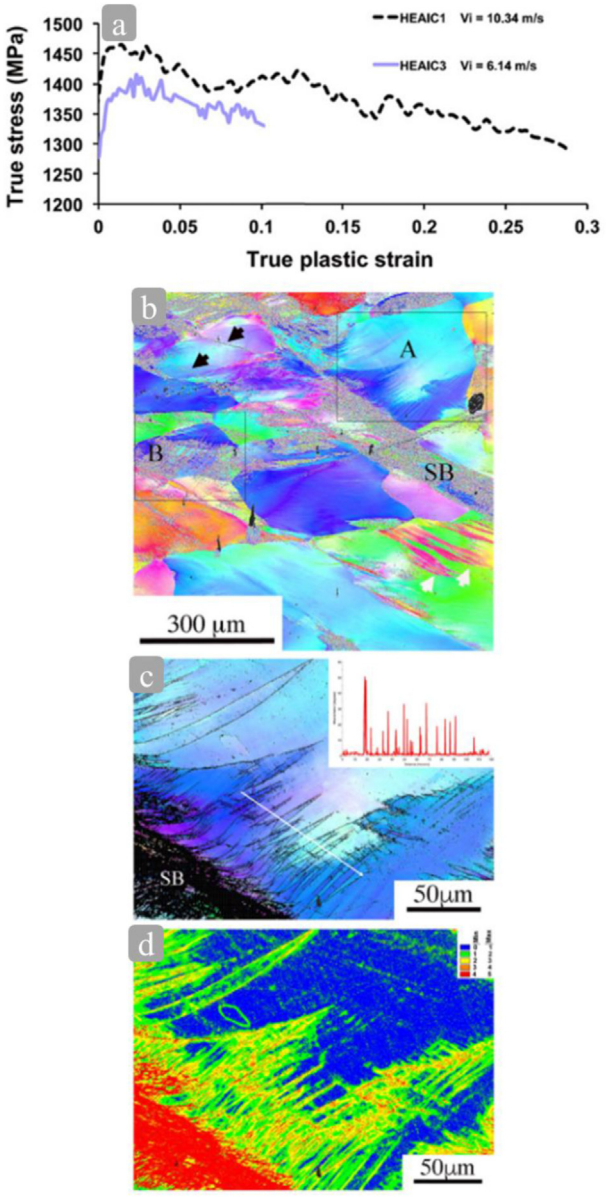

Fig. 20 – (a) The compressive true compressive stress vs. true compressive strain curve of RHEA $Ti_{20}Hf_{20}Zr_{20}Ta_{20}Nb_{20}$. (b) IPF map showing the localized deformation in area adjacent to shear band. (c) Magnified grain boundary map of the area marked by A in (b). (d) KAM map of (c) indicating lattice distortion and lenticular structures in interior and the neighboring area of the shear band [179].

used in critical components of modern-day jet engines. Novel refractory high-entropy alloys (RHEAs) are being considered as a potential replacement for superalloys due to their excellent resistance against softening at elevated temperature. Dynamic properties of $Ti_{20}Hf_{20}Zr_{20}Ta_{20}Nb_{20}$ with average grain size of ~200 μm were investigated by Dirras et al. [179] using a Hopkinson bar system with strain rate up to ~$3.4 \times 10^3\ s^{-1}$. They are among the first to investigate dynamic properties of BCC HEAs comprised of refractory elements. The stress–strain curve at high strain-rate condition illustrated in Fig. 20(a), shows a progressively decreasing flow stress at strains >0.05, denoting the occurrence of instability and an intensive softening effect after yielding. Formation of shear bands was clearly revealed in Fig. 20(b), with a highly distorted neighboring needle-like features indicated by black arrows with misorientation profile displayed in Fig. 20(c). Such needle-like structure is considered as thin shear bands at internal areas of grains. The lamellar structure was previously defined as a combination of twins and shear bands [180]. However, a misorientation angle lower than 60° has been revealed across the boundaries of needle-like structures, as shown in Fig. 20(c), suggesting other possibilities than twin boundaries and demanding additional work to provide additional clarification. Although preceding studies reported that the occurrence of shear band is always coupled with DRX. The formation of DRX in the present alloy is strongly confined due to slow diffusion rate in Ta and Ta–W alloys [181]. Therefore, the authors proposed that the DRX is unlikely to form in the $Ti_{20}Hf_{20}Zr_{20}Ta_{20}Nb_{20}$ alloy with such short duration of deformation time.

On the basis of Dirras's work [179], the dynamic behavior of $Ti_{20}Hf_{20}Zr_{20}Ta_{20}Nb_{20}$ RHEA at elevated temperature was further investigated by Hu et al. [182]. The true stress–strain curves at various strain-rates and temperatures are displayed in Fig. 21. As shown in Fig. 21(a), the strain rate hardening effect at room temperature was not pronounced under dynamic conditions. At elevated temperature (673 K), however, the yield strength of the alloy exhibited stronger dependence to strain rate. Such behavior could be explained in terms of strain-rate sensitivity, m:

$$m = \frac{\partial \sigma}{\partial \ln \dot{\varepsilon}} = \frac{\sigma_2 - \sigma_1}{\ln(\dot{\varepsilon}_2 - \dot{\varepsilon}_1)} \tag{3.14}$$

σ_2 and σ_1 are the flow stresses in compression at different strain rates of $\dot{\varepsilon}_2$ and $\dot{\varepsilon}_1$. A stronger strain rate dependence of stress occurs at elevated temperature. Such behavior was chiefly associated with more intensive viscous drag effect [183,184]. The high strain-rate sensitivity established at elevated temperature suggests enhanced resistance to shear localization. In addition, similar to conventional alloys, the yield strength and flow stress was inversely proportional to the temperature increase. Such behavior is often found in BCC metals and is mainly due to a change of Peierls-Nabarro stress, which is the predominant factor controlling screw dislocation propagation. One can also see that the $Ti_{20}Hf_{20}Zr_{20}Ta_{20}Nb_{20}$ RHEA retains a relatively high strength at elevated temperature. The temperature sensitivity parameters η_a which revealed the thermal softening effect of materials are listed in Table 1, and are expressed as:

$$\eta_a = \left| \frac{\sigma_2 - \sigma_1}{T_2 - T_1} \right| \tag{3.15}$$

where σ_1 and σ_2 are stresses at temperature T_2 and T_1, respectively. The authors conclude that the enhanced viscous drag effect was coupled with elevated temperature, and was reflected in rising strain-rate sensitivity of dynamic tests at 673 K.

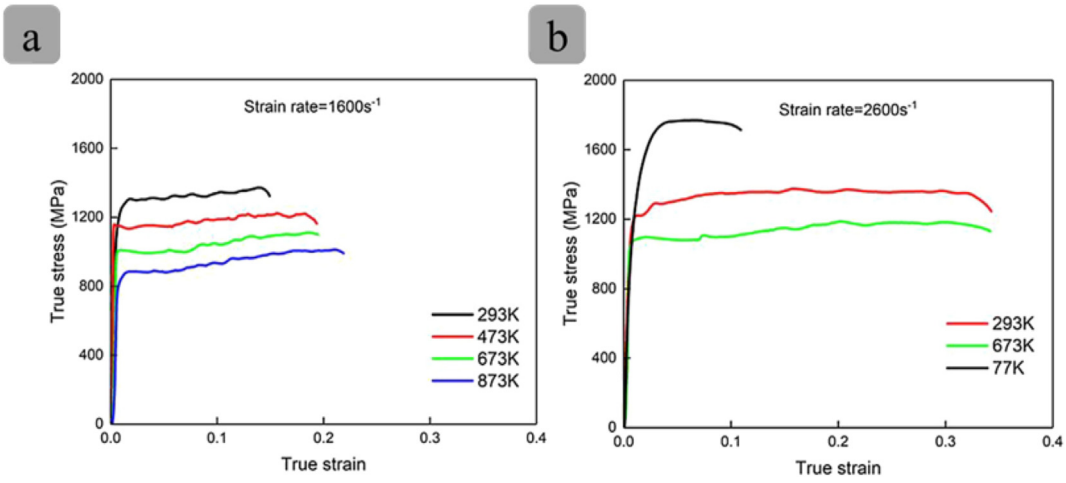

Fig. 21 – Dynamic compressive true stress true strain curves of $Ti_{20}Hf_{20}Zr_{20}Ta_{20}Nb_{20}$ RHEA samples at various strain rates and temperatures [182].

Table 1 – Variation of temperature sensitivity η_α with strain rate [183].

True strain	Strain rate	Temperature(k)	Temperature sensitivity, η_a (Mpa/K)
0.03	$1600s^{-1}$	293 K–473 K	0.83
		473 K–673 K	0.79
		673 K–873 K	0.54
	$2600s^{-1}$	77 K–293 K	2.19
		293 K–673 K	0.55

Particular HEA systems have been investigated extensively, for example, the Al–Cr–Fe–Co–Ni and Co–Cr–Fe–Mn–Ni. Based on the dynamic properties examined by Hopkinson pressure bar, most HEAs comprised of three d-transition elements exhibited both high strength and high strain hardening ability when subjected to dynamic loading. Despite evident shear banding observed widely in dynamically deformed HEA, the critical shear strain to induce shear localization was significantly deterred. Further microstructure characterization suggested that although traditional approaches to improve work hardening ability, like twinning and dislocation multiplication, were detected in HEAs, their presence could be altered by local chemical order, second phase formation, solution atoms and so on. RHEAs, however, provide another path to design high-temperature alloys. With the addition of refractory elements, their strength at elevated temperatures was well maintained.

3.2. *Ballistic impact response*

Understanding of dynamic behavior at strain rates ranging on the order of $10^5\ s^{-1}$, beyond the usual range of Hopkinson bars, is mainly achieved by ballistic impact tests [185]. In general, ballistic impact test is accomplished by high-speed collision between projectile and target materials. This idea was first proposed by Taylor [186] in 1948 by accelerating a flat-head cylindrical projectile to a rigid target. This test is also known as Taylor impact test. It is very useful in obtaining important information on the dynamic behavior of materials. The plastic deformation generated during impact is concentrated in the impact region, which is which is separated from undeformed material. In Taylor's analysis, the dynamic yield strength can be estimated by the following equation:

$$\sigma_y = \frac{\rho v_0^2}{2} \cdot \frac{l_0 - l_f}{l_0 - L_f} \cdot \frac{1}{\ln(l_0 - l_f)} \tag{3.16}$$

here ρ is cylindrical rod density, l_0 is initial length of the rod, v_0 is projectile flying velocity, l_f is final undeformed section length, L_f is the overall final length of the specimen.

During this process, the leading elastic compressive wave is followed by the plastic compressive wave [187]. When this amplitude exceeds the yield strength of the material, severe deformation in the form of radial motion outward away from the specimen axis occurs.

Distinctive shear condition can take place with different geometries of projectile, such as cylindrical, conical, and blunt. Investigations of impact response have been conducted on various metallic materials, including 7039 aluminum alloy [188], $Al_{0.1}CoCrFeNi$ [189] and $Fe_{27}Co_{24}Ni_{23}Cr_{26}$ [190]. However, due to substantial amounts of variants and uncertainties in ballistic impact tests, the experimental results can vary significantly from one source to another.

The ballistic response of Mn-free $Fe_{27}Co_{24}Ni_{23}Cr_{26}$ alloy, as one of the variants close to CoCrFeMnNi HEA, was examined [190]. As shown in Fig. 22, EBSD mapping revealed the deformation response in three different domains: (a) undeformed, (b) intermediate deformation, and (c) severe deformation. In the domain prior to deformation, only annealing twins were discovered, while nano-sized twins could not be distinguished (Fig. 22(a, d)). As shown in Fig. 22(e) (f), specimens subjected to both intermediate and heavy deformation revealed twin–twin interaction, while the latter revealed formation of nanotwin bundles and interaction between deformation nanotwins due

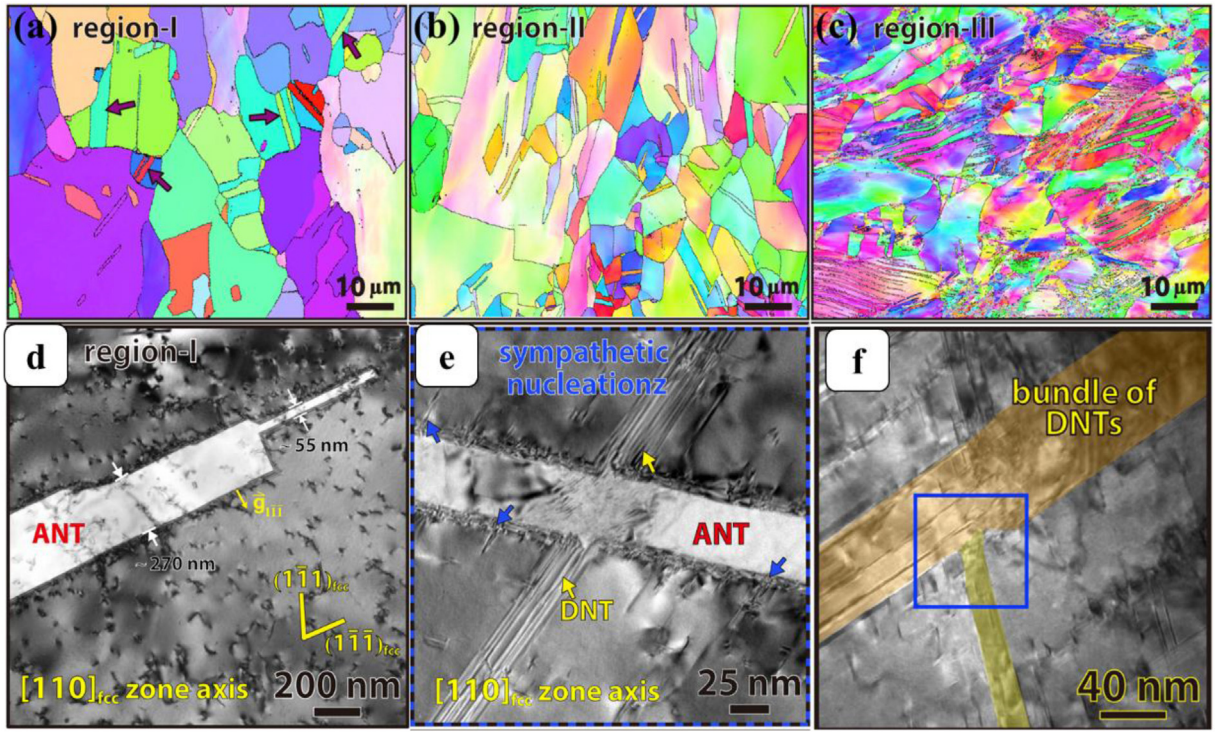

Fig. 22 – (a) EBSD IPF maps and TEM images of $Fe_{27}Co_{24}Ni_{23}Cr_{26}$ alloy (a, d) non-deformed area (b, e) intermediate deformation area and (c, f) severely deformed area. Annealing nanotwins are revealed in (d, e, f), and bundle of deformation nanotwins (DNTs) are revealed in (e, f) [190].

to increasing twin density. Therefore, multiplication of twins significantly confines dislocation motion and deters the activation of shear localization.

Muskeri et al. [189] reviewed the ballistic impact response of single-phase $Al_{0.1}CoCrFeNi$ HEA, which is one of the first HEAs examined dynamically. By applying EBSD analysis, distinctive microstructures were observed in areas with different distances to the crater wall, as shown in Fig 23. In the condition of partial penetration, both low angle misorientation (~2-3°) and high angle misorientation (~60°) deformation corresponding to deformation microbands and deformation twins, respectively, were revealed in Fig 23(a). Deformation microbands were formed as a consequence of planar dislocation arrays that had been previously observed in FeNiMnAlCr alloy [191], $Cr_{10}Mn_{50}Fe_{20}Co_{10}Ni_{10}$ alloy [192], and $Al_4Mo_4Nb_8Ti_{50}Zr_{34}$ alloy [193]. They can provide similar effect as strain hardening due to mechanical twins through dense dislocation boundaries. One can see that the domains close to the crater wall exhibited much higher hardness (by a factor of 2.5) than the undeformed domains, as illustrated in Fig. 23(e). In addition, there was no evident formation of shear bands at low-velocity impact, indicative of the excellent strain hardening ability associated with twins and microband formation. However, increasing impact velocities (to 739 m s^{-1} and 994 m s^{-1}) were coupled with pronounced formation of shear bands and recrystallized grains, suggestive of dominant thermal softening over hardening effect. In full penetration condition, the highest hardness (~5 GPa) was measured at the domain near the entry and exit holes.

Moreover, Choudhuri et al. [194] reviewed the ballistic performance of a series of nickel-based HEAs, reporting an excellent classic strength-ductility tradeoff. They fabricated $AlCoCrFeNi_{2.1}$ HEA with dual-phase (FCC–B2 phases) via thermomechanical processing. The ballistic testing was performed with tungsten-carbide projectiles. Varying impact velocities were applied to investigate deformation features in three different conditions (partially penetrated/plugged/fully penetrated) as shown in Fig. 24(b–d). The EBSD micrograph of partially penetrated specimen (Fig. 24(f)), displays a restrained crack growth path within B2 lamellar domains. In addition, shear bands were also observed, denoting severe shear deformation in local domains. Such phenomenon was likely associated with residual stresses provided by crack formation. However, with increasing striking velocity (higher than plug condition), shear localization becomes the dominant failure mode and guides crack growth, similar to other HEAs mentioned earlier.

Instead of studying the impact resistance, the penetration performance, essential to anti-armor application, was examined by Xing-Fa Liu et al. [195]. Besides HEAs only comprised of 3 d-transition metals, such as Fe, Co, and Ni, the emphasis has shifted to HEAs containing refractory elements such as Mo, Ta, and W. A "self-sharpening" multiphase WFeNiMo HEA fabricated by electromagnetic levitation melting technology was investigated by Liu et al. [195]. There is a constant competition between ballistic ("bullet-proof") materials and materials to defeat armor. The concept of "self-sharpening" is associated with the specific increase in the depth of the

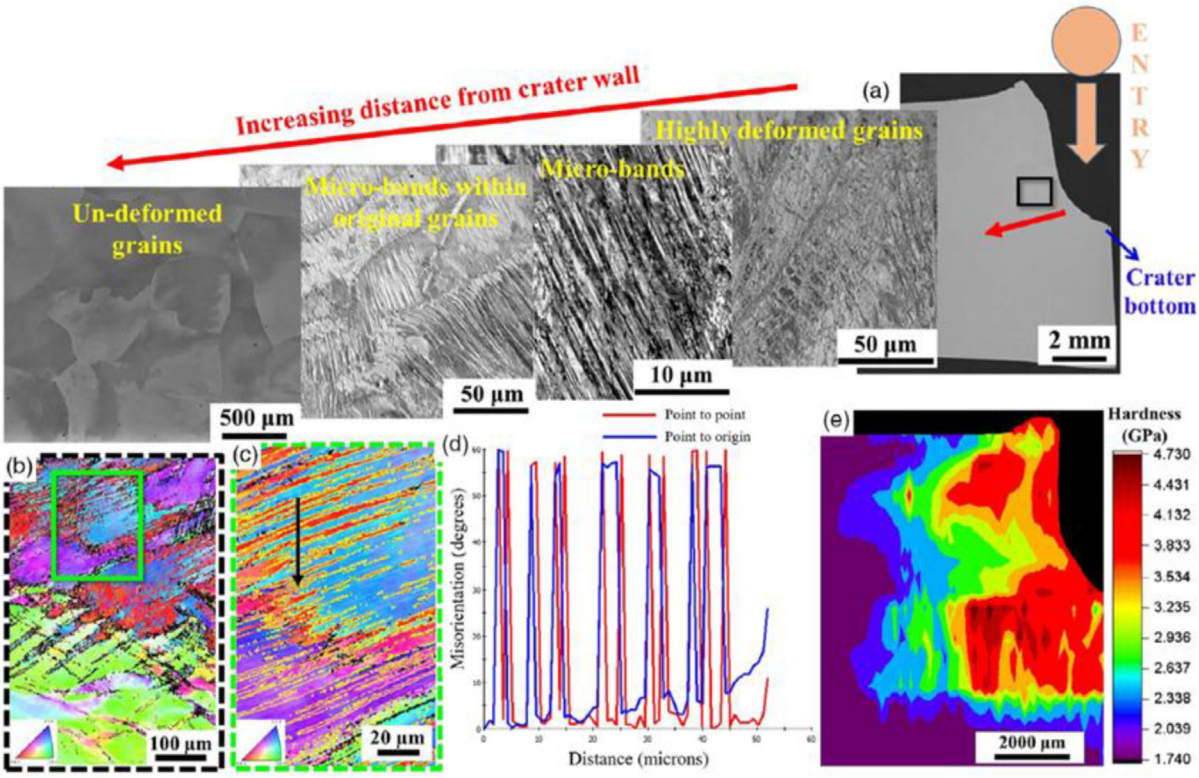

Fig. 23 – (a) Microstructure as a function of distance from the crater wall for partially penetrated $Al_{0.1}$CoCrFeNi HEA plate showing highly deformed grains, microbands, and undeformed grains; (b) IPF map of the domain in the black box marked in (a); (c) Magnified IPF map of the selected domain in green box marked in (b) showing formation of deformation twins; (d) misorientation profile along the arrow shown in (c), indicating boundaries with 60° misorientation that is classic trait of twinning; (e) nano-indentation hardness contour map indicating maximum hardness at the domain close to crater wall [189].

penetration (DOP) by sharpening the penetrator rod into acute shape. Conventional materials used to fabricate rod penetrators are tungsten heavy alloys (WHAs) and depleted uranium alloys (DUAs). While the WHA are relatively less effective due to high penetration resistance plus decreased DOP, the DUA penetrators are widely banned because of many relative long-term health problems. In DUAs the sharp tip is ensured by sequential shear-band formation. On the other hand, WHAs tend to form mushroom shape upon impact, significantly compromising penetration performance. Therefore, novel metallic alloys, that can efficiently penetrate through armors, are desperately in need. Preceding studies proposed applying severe plastic deformation, such as cold torsion [196], swage molding [197], and hot-hydrostatic extrusion [198,199]. Other researchers claimed a "self-sharpening" achieved by inducing shear localization [200–206]. Contrary to traditional uniaxial dynamic compression tests on cylindrical specimens, whose stress conditions are unfavorable for shear band formation [207], the unique shape of rod penetrator endows desired conditions for shear localization to take place. The shear failure localized at the edge of the penetrator heads during deformation consistently pulls off and sharpens them, leading to high depth of penetration. In addition to the softest FCC matrix phase, tungsten BCC and Fe/Ni concentrated μ phases can provide stiffer and stronger properties of the present alloy. Substantially different properties among three phases enabled the excellent synergy of high strength and ductility under dynamic conditions, with yield strength, fracture strength and fracture strain equal to 1200 MPa, 1900 MPa, 0.28, respectively. As for the ballistic performance, in contrast to conventional 93 W alloy, the WFeNiMo HEA exhibited a superior penetrating performance, represented by the acute head shape, as shown in Fig. 25. The achievable "self-sharpening" ability was mainly attributed to unique microstructure of WFeNiMo HEA, which promoted higher susceptibility to shear localization. As the shear bands continue to develop, the deformed parts are peeled off, resulting in the sharp shape of the penetrator. μ phase plays an essential role in shear band formation by promoting inhomogeneous deformation and higher strain gradients. The shear localization mechanism proposed in Fig. 26 (c-g) illustrates that the distribution of μ precipitates contributes to the intense inhomogeneous deformation and strain gradient.

3.3. *Shock compression response*

The shock response of materials is an indication of their mechanical properties at ultra-fast deformation speed. Via explosive detonation, projectile impact, high-power pulsed-laser-driven shock compression, ultra-high-speed deformation can

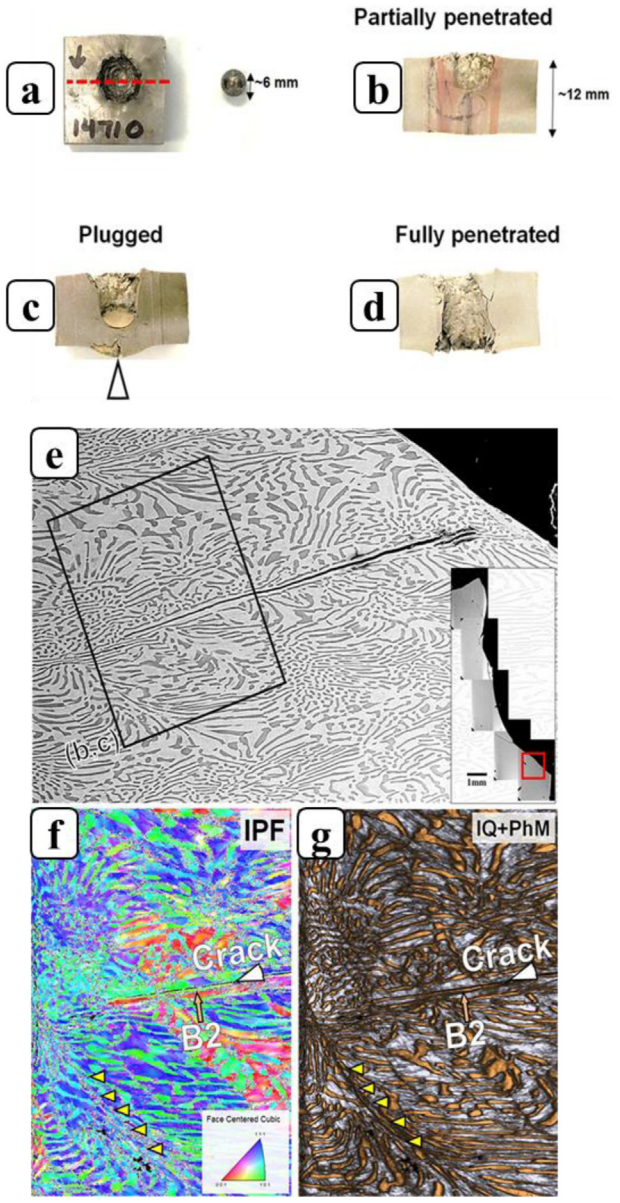

Fig. 24 – (a–d) Optical micrographs showing (a) sections of the impacted EHEA plate along with the WC projectile. Cross sectional areas of specimens with different impact conditions: (b)partial penetration, (c) plugged condition, (d) full penetration. (e) BSE (back scattered electron) image, and corresponding (f) EBSD IPF mapping for area within black box, showing formation of crack along FCC/B2 interphase (indicated by white arrow) and shear band (indicated by yellow arrow).

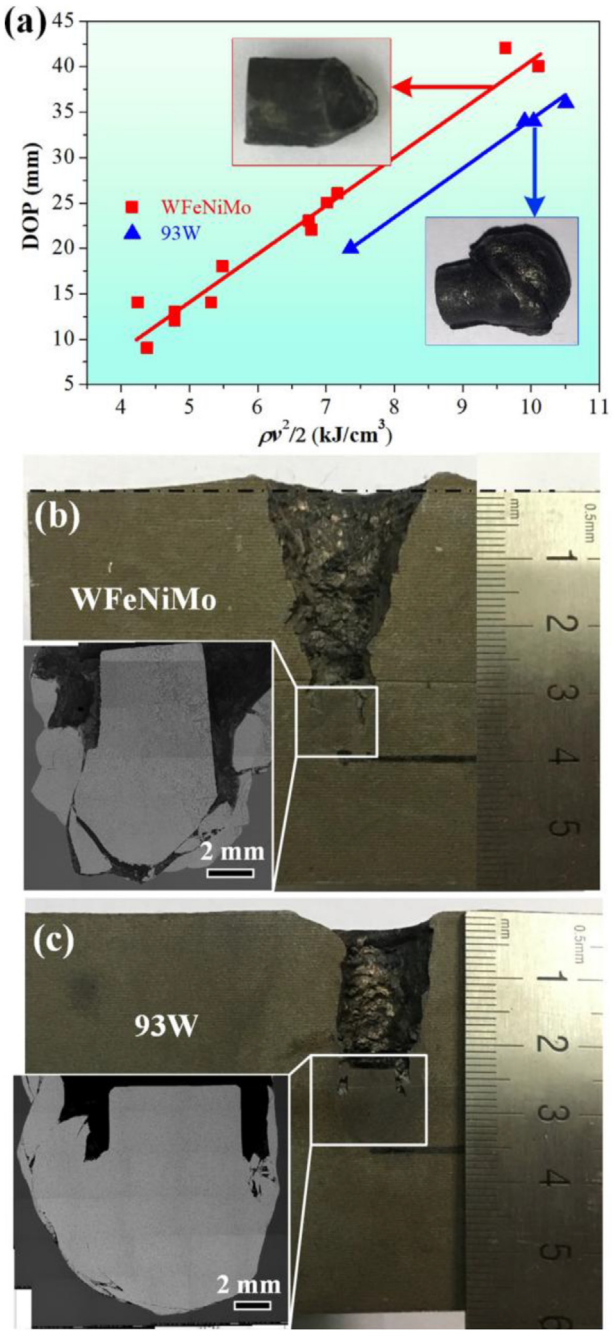

Fig. 25 – (a) Depth of penetration of WFeNiMo rod and 93 W rod versus kinetic energy per volume calculated by $\frac{\rho V^2}{2}$, with images of the retrieved remnants, respectively; longitudinal sections of medium carbon steel targets impacted by (b) a WFeNiMo penetrator and (c) a 93 W penetrator, with SEM micrographs of the remnant in the corresponding insets, respectively [195].

be generated. The propagation of a plane shock is denoted by the (U, u) Hugoniot curve (U is shock velocity and u is particle velocity), which is one of the primary methods to investigate shock compression response. In addition, the yield strength derived from the curves which is also known as HEL (Hugoniot Elastic Limit), which represents strength at the point when relaxation wave has not arrived, and target is only deformed along lateral direction. The yield strength in shock compression can measured through von Mises yield criterion [35]:

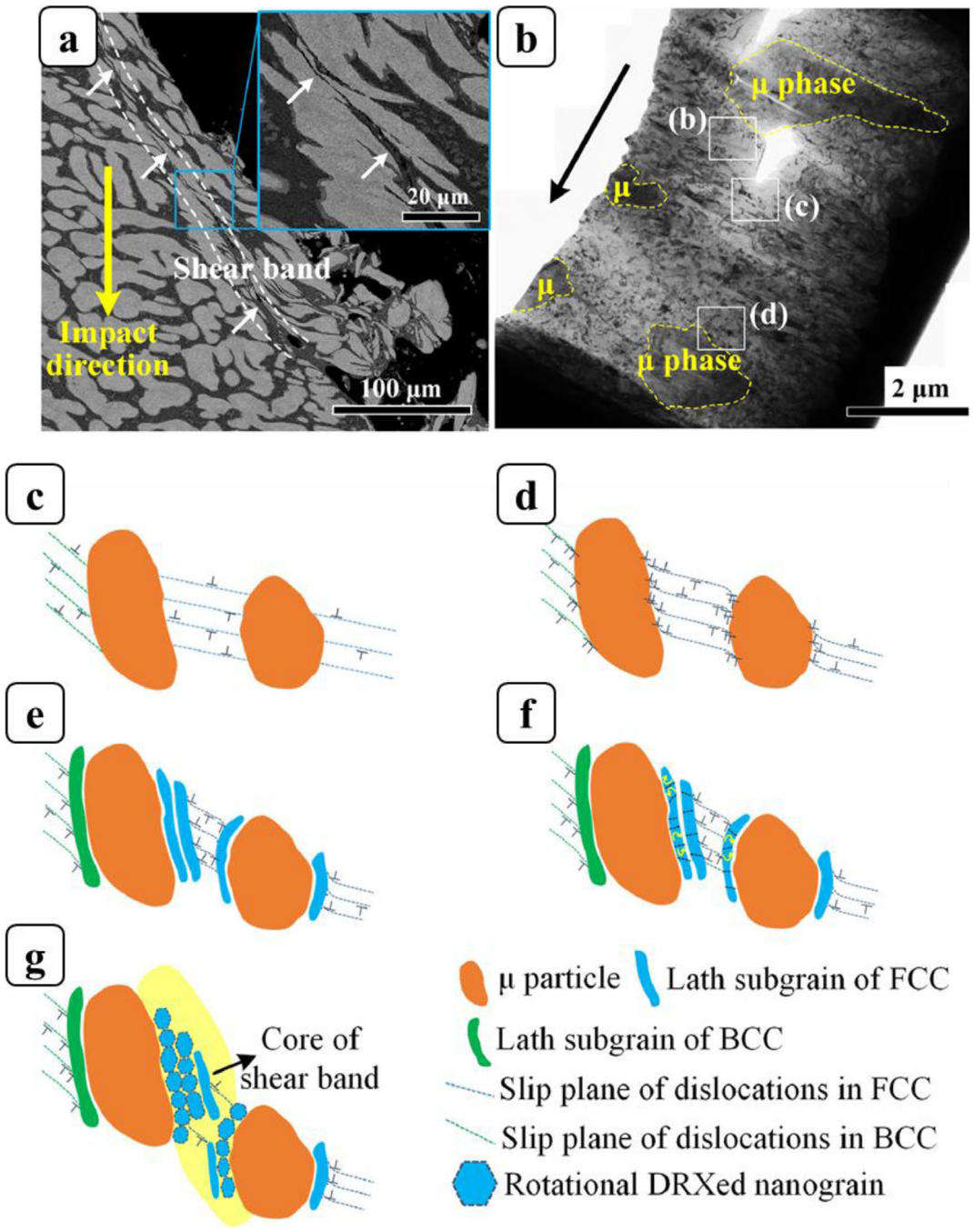

Fig. 26 – (a) SEM and (b) TEM images showing microstructures of shear band. (c-g) Schematic drawing showing the formation mechanism of shear band in WFeNiMo alloy; (c) Undeformed microstructure with low dislocation density; (d) Formation of strain gradient due to geometrically necessary dislocation (GND); (e) Formation of elongated subgrains due to cotinuously rising dislocation density; (f) Elongated subgrain evloves into equiaxed grains and rotates to accommodate further deformation; (g) Onset of shear band cc [194].

$$\sigma_Y = \sigma_H\left(\frac{1-2\upsilon}{1-\upsilon}\right) \tag{3.17}$$

where υ is Poisson's ratio, σ_H is elastic limit under uniaxial strain condition. Therefore, the HEL value can be expressed as a function of yield strength σ_Y and Poisson's ratio υ, and this relationship can only be applied to dynamic conditions. The plate impact geometry is illustrated in Fig. 27.

An investigation on shock compression response of the FCC-matrix CoCrFeMnNi alloy and BCC-matrix NiCoFeCrAl alloy was performed by Jiang et al. [208]. The measured free surface velocity profiles in Fig. 28 illustrate that high elastic limits (HEL) could be obtained from both HEAs (2.3–2.9 GPa and 3.5–3.9 GPa), suggesting a surprisingly high capacity to resist high speed damage. Fig. 29 displays the TEM

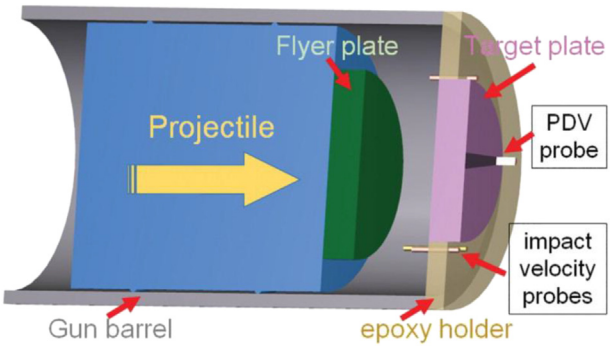

Fig. 27 – Schematic drawing of plate impact [208].

micrographs for undeformed and deformed specimens, suggesting low densities of dislocations and stacking faults before shock compression in both CoCrFeMnNi alloy and NiCoFeCrAl HEAs. The TEM images of deformed samples recovered from 11.7 GPa to 10.4 GPa are shown in Fig. 29(a) and Fig. 29(b), respectively. As shown in Fig. 29(a)., mechanical twinning and dense dislocations are observed, therefore suggesting a dominant deformation mechanism l by dislocation movement and twinning for FCC-matrix CrMnFeCoNi alloy. In contrast, no visible twins could be found in NiCoFeCrAl alloy and only tangled dislocations can be observed, denoting a plasticity primarily led by dislocation movement. A much higher shock yield strength was measured in the latter, which could be attributed to precipitate hardening and nano-

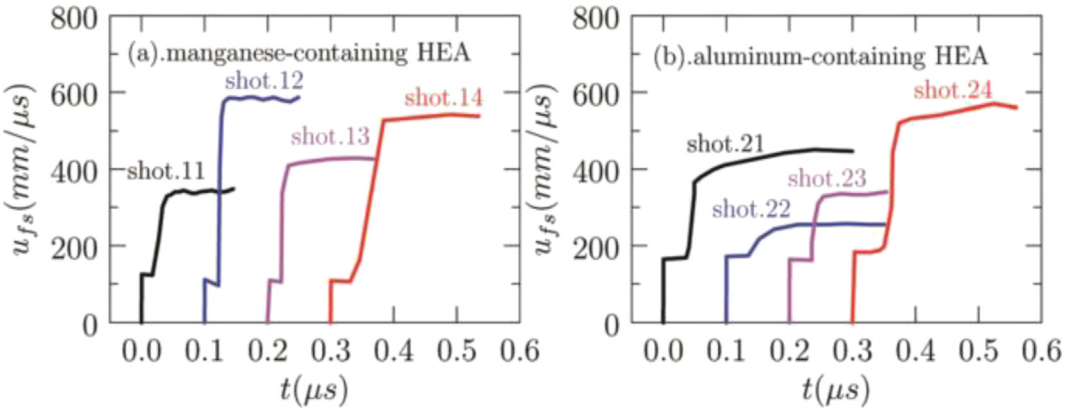

Fig. 28 – The measured free surface particle velocity as a function of time for (a) CoCrFeMnNi and (b) NiCoFeCrAl HEAs [208].

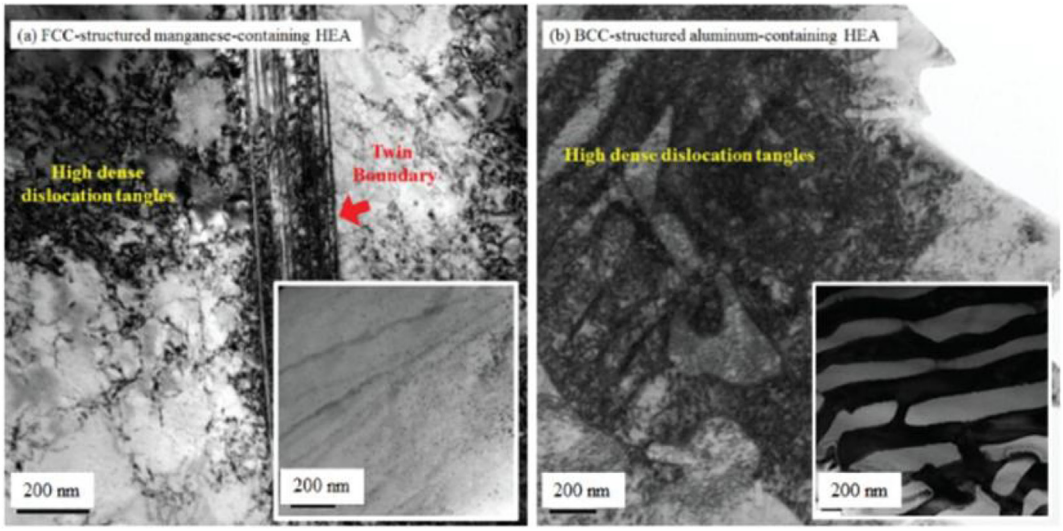

Fig. 29 – TEM micrograph showing distinct microstructure in the deformed and undeformed samples: (a) comparison between the pre-loading manganese-containing HEA (CrMnFeCoNi) sample and sample recovered from 11.7 GPa, indicating the formation of tangled dislocations and deformation twins; (b) comparison between the pre-loading aluminum-containing HEA (NiCoFeCrAl) sample and sample recovered from 10.4 GPa, indicating formation of tangled dislocations [208].

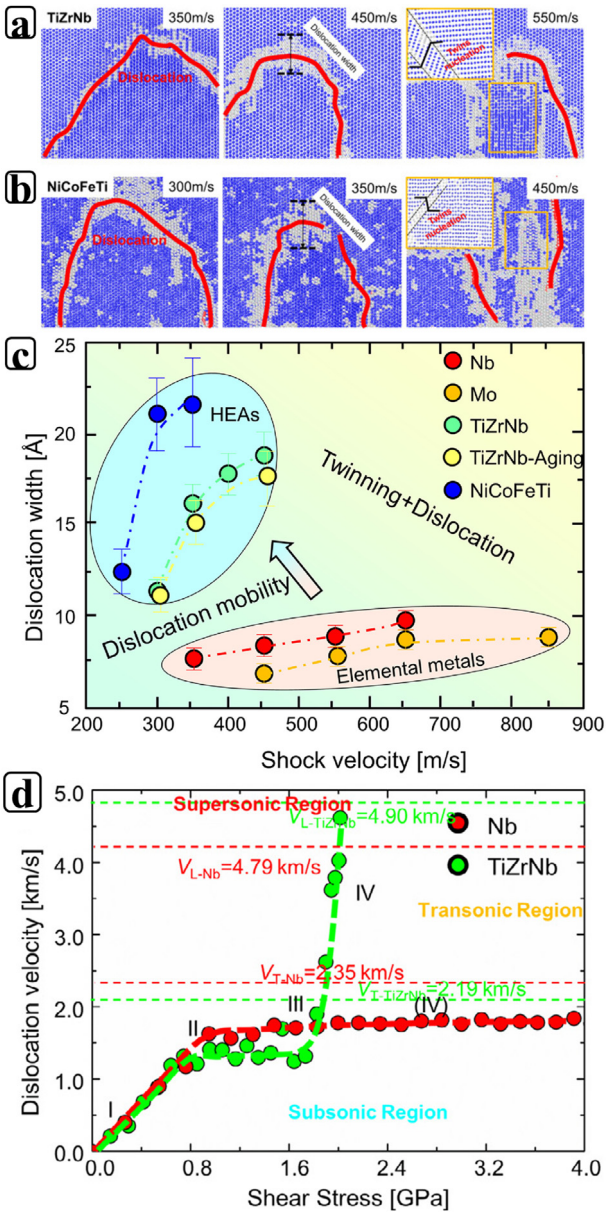

Fig. 30 – (a) (b) Typical dislocation structures at the wave front for bcc NiCoFeTi and TiZrNb HEAs. The atomic configuration is identified by common neighbor analysis (CNA), blue: bcc, white: defect. The red line shows the contour of moving dislocations. The inserts show the magnification of the corresponding nano-twin nucleus at the highest shock velocity. (c) Dislocation width as a function of shock velocity. NiCoFeTi and TiZrNb samples are prepared with random solid-solution while TiZrNb-Aging shows the TiZrNb samples with local chemical short-range order [209].

composite strengthening effect resulting from the formation of Cr-rich and Al-rich BCC phases [1]. The authors concluded that the exceptionally high HEL could be possibly associated with inherent server lattice distortion coupled with enhanced lattice frictional stress.

Molecular dynamics (MD) [209] using the common neighbor analysis (CAN) for defect identification pointed out the shock strength dependence of dislocation structure for BCC HEAs, illustrating a strong relationship between shock velocity and dislocation width, as shown in Fig. 30(a–c). An extended edge dislocation structure was observed in TiZrNb and NiCoFeTi HEAs which was different from BCC elemental materials Nb and Mo. Such unique dislocation structure was mainly attributed to the strong dependence of dislocation behavior on shear stress. The high shear stress was coupled with high dislocation mobility and extended morphology, while a compact dislocation core structure was associated with a low shear stress. Extended features of edge dislocations were correlated to four stages of shock response that correspond to compact dislocation core, dislocation with elastic energy radiation, extended dislocation core and twinning, as shown in Fig. 30(d).

3.3.1. *Spall behavior*

Spallation is a type of fracture that occurs at strain rates larger than 10^2 s^{-1}. When materials are subjected to shock waves, a tensile pulse is generated when waves reach to the free surface. During this process, if the tensile stress exceeds the strength, spall failure occurs [210,211]. The evolution of spall failure involves the nucleation and propagation of micro-voids or micro-cracks resulting from the transient tensile stress. Curran [212] developed a model in 1987 to describe the formation of voids and cracks. Several properties can be measured in a spalling test including spall strength and the time to failure. This technique has received a vast amount of attention due to its importance to materials applications in military and industrial fields. In contrast to the static loading, the fracture modes and deformation mechanisms are significantly different [35,212,213]. The pressure in the shock wave can be expressed by the Rankine-Hugoniot relationship [214]:

$$P = \rho_0 U u \tag{3.18}$$

where ρ_0 is the density of specimen, u is the particle velocity, and U is the wave velocity. It can be approximated as:

$$U = c_b + su \tag{3.19}$$

where c_b is the bulk sound speed and s is linear Hugoniot slope coefficient. These two parameters are material dependent, and the equation is known as equation-of-state. Another important factor to be considered is the free-surface velocity which represents the velocity change of the free surface during impact test. This parameter is usually used to describe the initial damage and the damage evolution rate. Similar to the stress–strain curve in dynamic tensile/compressive test that provides stress profile during deformation, free-surface velocity profiles are used to investigate shock wave motion, void nucleation kinetics, and spall strength. According to Stepanov [215], the spall strength can be expressed as:

$$\sigma_f = \rho_0 c_l \Delta u \left(\frac{1}{1 + \frac{c_l}{c_b}} \right) \tag{3.20}$$

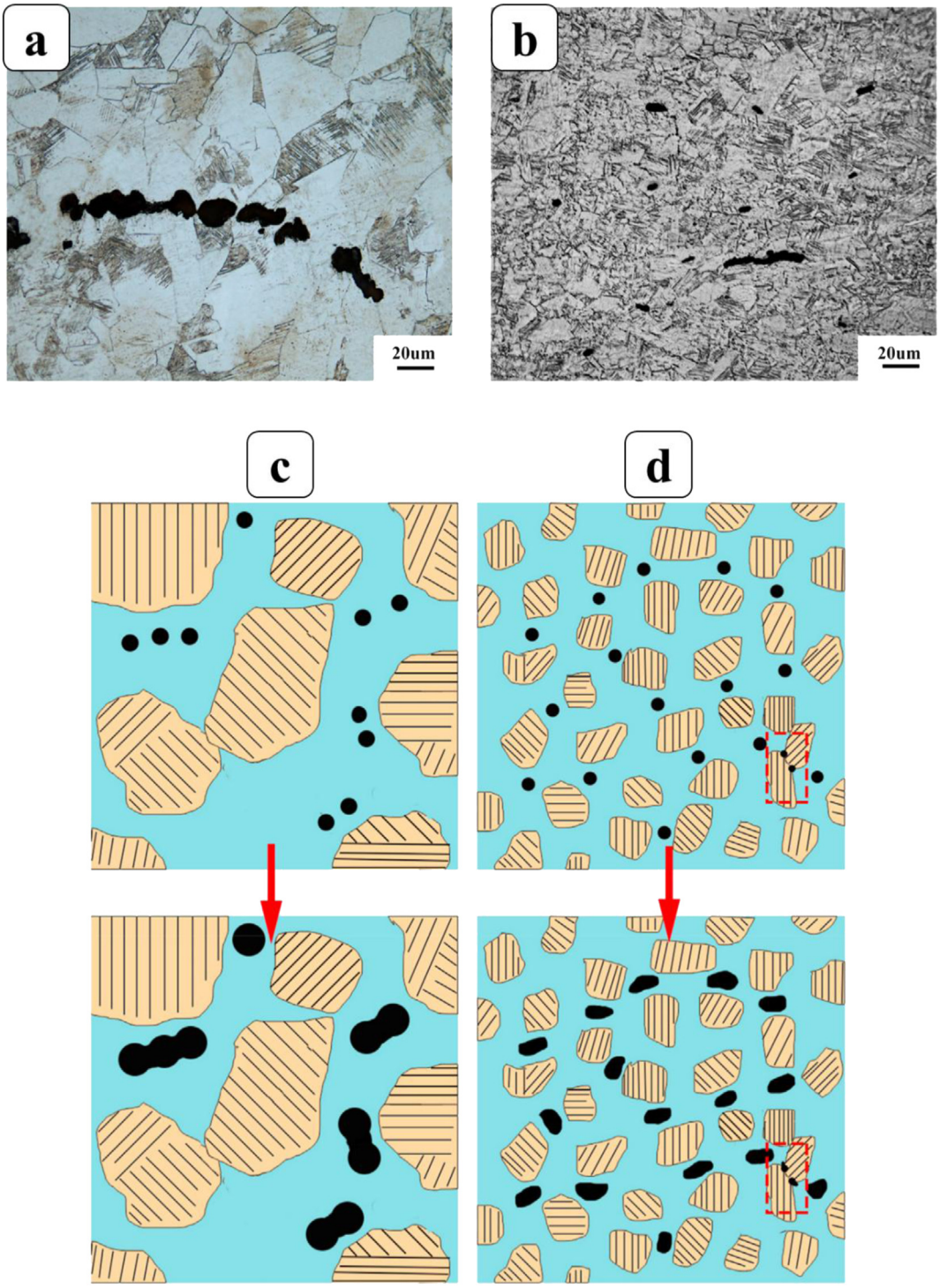

Fig. 31 – Optical microscope images of spall damaged (a) hot-rolling plus quenching (HRQ) sample; (b) cold-rolling plus quenching sample (CRQ). Schematic drawing of void evolution in the (c) HRQ and (d) CRQ samples [216].

where ρ_0 is the sample density, c_l is sound velocity along longitudinal direction, Δu is equal to difference between maximum and minimum particle velocity. Therefore, it is crucial to study HEAs that can resist spallation due to their potential value to be applied to nuclear engineering, which are demanding in terms of resistance to intense ion irradiation.

The spall behavior of metastable dual-phase $Fe_{50}Mn_{30}CoCr_{10}$ HEA at two impact velocities (190 m/s and 420 m/s) has been reported by Yang et al. [216] by using a single-stage light gas gun; the formation of voids and microcracks was affected by phase composition. Alloys subjected to different manufacturing processes (hot-rolling + quenching, cold-

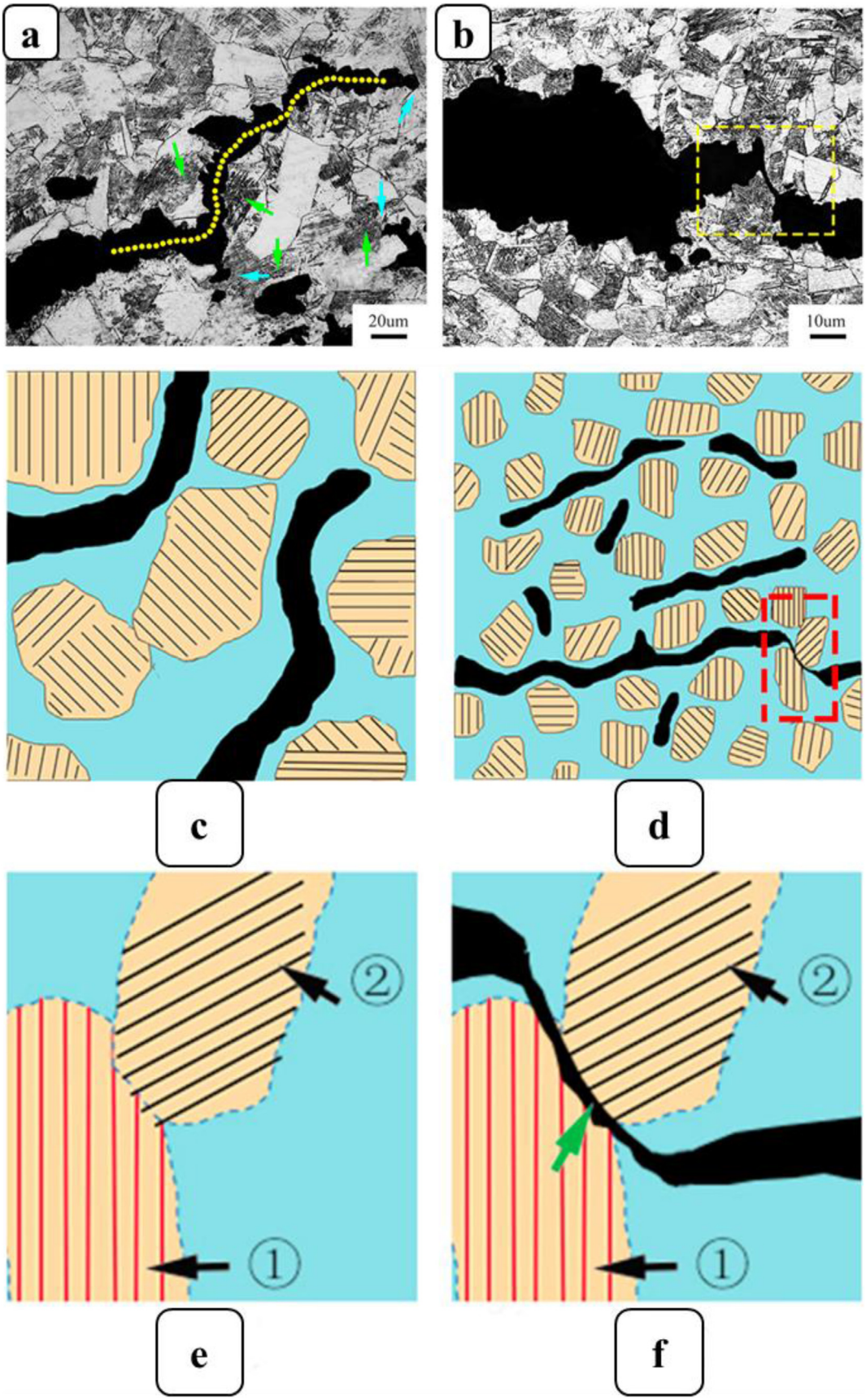

Fig. 32 – Evolution of micro-cracks under 420 m/s impact loading: (a) HRQ sample subjected to impact velocity of 420 m/s; (b) CRQ samples subjected to velocity of 420 m/s. Schematic drawing of the microcrack propagation: (c) evolution of microcrack in HRQ sample; (d) evolution of microcrack in CRQ sample; coalescence path at the interface of adjacent martensite phase; (e) the martensitic area with two different variant orientations; (d) the formation of coalescence path at the interface of two variants [216].

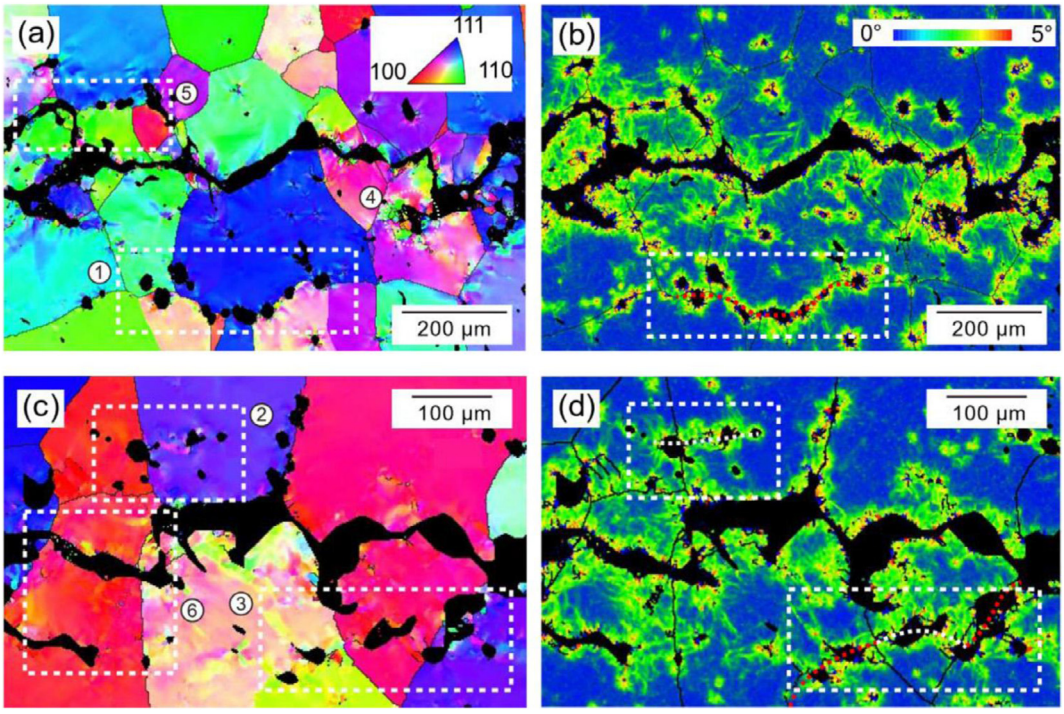

Fig. 33 – EBSD (a, c) IPF maps and (b, d) KAM maps of void coalescence and crack propagation in $Al_{0.1}CoCrFeNi$ HEA [221].

rolling + quenching) exhibit distinctive phase components. One major important factor was the formation of martensite. The size of martensite plates for hot-rolled specimens was much larger than the cold-rolled ones, however its weight ratio was much higher and its distribution in matrix was more uniform in cold-rolled specimens. Due to a deficiency of driving force caused by neutralization between compressive residual stress and external tensile pulse, the interior of martensite was unavailable for void nucleation. However, interfaces between matrix and martensite were preferred sites for void nucleation [217–220]. Fig. 31 shows the microstructure of (a) hot-rolled and (b) cold-rolled samples subjected to 190 m/s impact loading, denoting a higher density but less intensively nucleation of voids, faster initial damage rate, and lower spall strength in cold-rolled sample. Void nucleation, growth and coalescence at an impact velocity of 420 m/s are summarized in Fig. 32, suggesting that refined and evenly distributed martensite constrains coalescence which can lead to the formation of microcracks. Phase content can also affect the propagation of microcracks. Large-sized martensite plates can serve as obstacles to deviate or block microcrack propagation while small-sized martensite plates only have very limited effect in influencing microcrack propagation, resulting in the generation of large-sized cracks.

Contrary to $Fe_{50}Mn_{30}CoCr_{10}$ HEA, whose spall strength is mainly contributed by second-phase formation, Zhang et al. [221] demonstrated a superior ability to resist spallation in $Al_{0.1}CoCrFeNi$ alloy in a single-stage gas gun experiment, despite its inferior yield strength and tensile strength. The weaker spall strength in the $Fe_{50}Mn_{30}CoCr_{10}$ HEA is the result

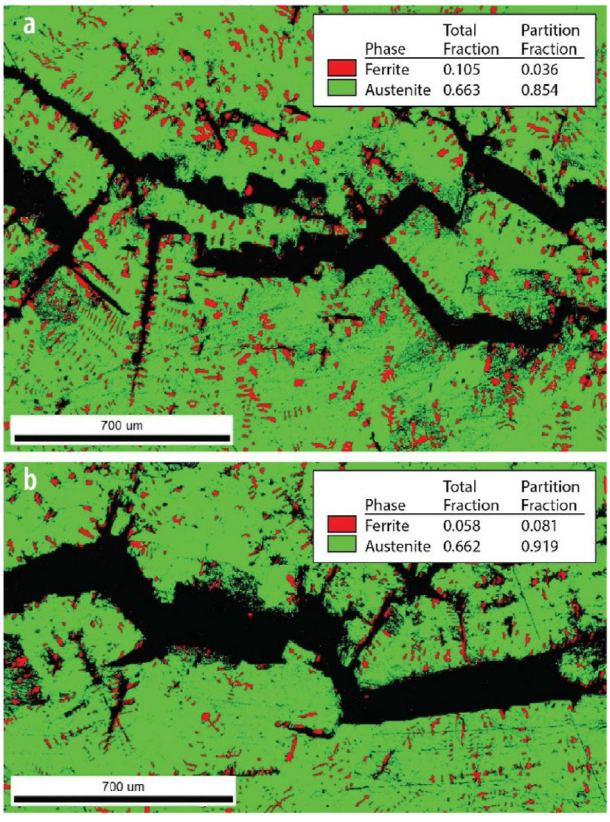

Fig. 34 – EBSD IPF maps showing cracking propagation and void nucleation in FeCrMnNi alloy [224].

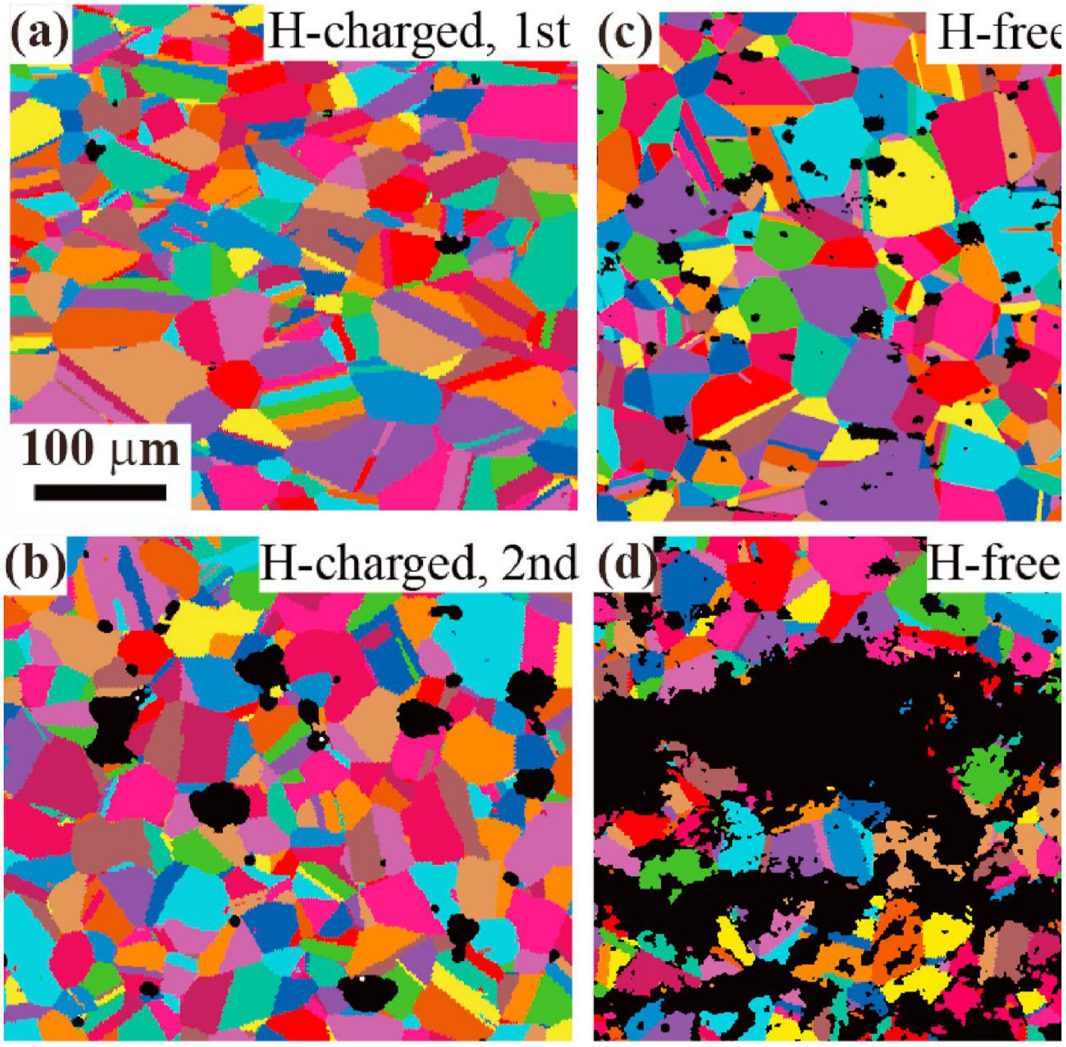

Fig. 35 – EBSD IPF maps showing cracking propagation and void nucleation in H-charged and H-free CoCrFeNiMn alloy (results from two experiments) [224].

of a soft matrix phase and rapidly growing cracks along interfaces between phases. It is noteworthy that at impact velocities below 511 m s^{-1}, deformation mode was governed by stacking faults and dislocation glide, while nano-twinning was benefited from rising shock velocity (>511 m s^{-1}). Moreover, an optimized spall strength can also be derived from approach of crack formation in $Al_{0.1}$CoCrFeNi. Intragranular voids dominated; they tend to emerge in regions adjacent to high angle grain boundaries. These voids are then connected by high misorientation bands and eventually lead to cracking, as shown in Fig. 33.

In contrast to ductile failure found in $Al_{0.1}$CoCrFeNi alloy, Hawkins et al. [222] observed a brittle spallation failure in FeMnCrNi alloy. They discovered that at the preliminary stage of spallation, relatively brittle ferrite phase was favored for void nucleation, as shown in Fig. 34. Although relatively same conditions (projectile velocity, tilt, etc.) were applied while spalling test, scattering results of HEL and spall strength were obtained. They conjectured that such disparate properties could possibly be caused by inhomogeneous microstructure and presence of Cr-rich ferrite phase. Given by its brittle failure mode, FeMnCrNi alloy was believed to be less desirable to be used in extreme loading conditions.

Thürmer et al. [223] provided experimental results combined with simulation for the classic equiatomic Cantor alloy. A spall strength of ~8 GPa at the strain rate of ~10^7 s^{-1} was found in this alloy, which was possibly caused by homogeneous distribution of composition and lack of phase segregation; the latter is detrimental to the buildup of spall strength. Moreover, traditional strengthening methods including nanotwins and precipitation also help to enhance strength.

Outside of the standard Cantor alloy composition, Xie et al. [224] reported a retardation of spallation in CoCrFeNiMn alloys charged with hydrogen. They introduced hydrogen into the alloy by using a cathodic electrochemical charging technique and investigated its effect on spallation. With the addition of hydrogen, the sizes of micro-cracks and micro-voids were

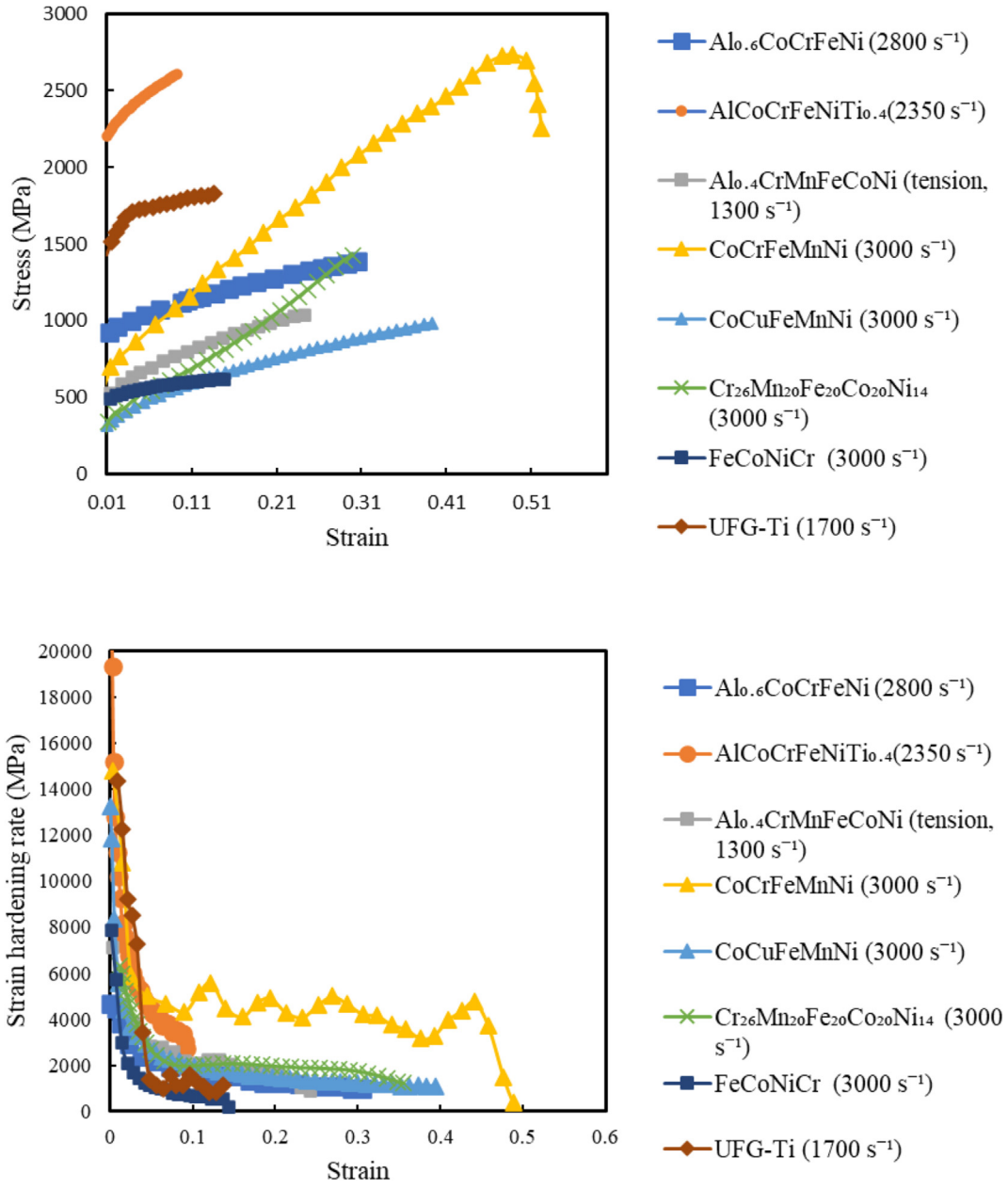

Fig. 36 – (a) Stress–strain curves and (b) Strain hardening rate vs. strain of various of high entropy alloys and ultrafine-grained-titanium (UFG-Ti).

reduced, as revealed in Fig. 35. The preliminary stage of vacancy and vacancy-hydrogen complex formation is mainly achieved by removing metallic atoms and replacing them with hydrogen atoms. Such optimized behavior primarily led to a higher diffusion barrier in hydrogen-vacancy complex. On the other hand, coalescence of micro-voids was greatly constrained by the pinning effect produced by hydrogen.

4. Summary and conclusions

Due to the complexity of multi-components systems, HEAs have highly tunable physical properties. However, systematic understanding of HEAs subjected to dynamic loading is yet to be achieved. Here, we report on mechanical behavior of HEAs under dynamic conditions, such as spall, shock wave compression, and split Hopkinson pressure bar compression/tension. Outstanding properties are found in FCC-based HEAs at room temperature and BCC-based HEAs at elevated temperatures. Nevertheless, the dynamic response of HEAs at cryogenic temperature is not included in present report.

Multiple deformation mechanisms contribute to the complex behavior: microband strengthening, solution strengthening, forest hardening, precipitation hardening, and martensitic transformation, which partially account for the extraordinary properties and deterred formation of shear

bands. In addition, twinning is a prominent deformation mechanism in the FCC-based HEAs due to their inherently low SFE. Shear banding resulting from adiabatic deformation derived from deteriorating strain hardening rate is widely present in many HEAs. HEAs with second phases exhibit outstanding dynamic properties, perhaps better than the single-phase HEAs. The inherently hard BCC and soft FCC phases generate an exceptional work hardening ability for $Al_xCoCrFeNi$ and WFeNiMo alloys. In general, the FCC-based alloys show high strain hardening rate, especially, the classic CoCrFeMnNi alloy. We summarize several HEAs with their corresponding dynamic stress strain curves and strain hardening rate in Fig. 36; in comparison with ultra-fine grain Ti (UFG), many HEAs exhibit much better work hardening ability in spite of the higher strength.

In comparison with FCC HEAs, the dynamic properties of refractory HEAs at room temperature are less attractive due to strongly limited ductility. However, they can retain strength at elevated temperatures due to the inherently high melting temperature of refractory elements. Therefore, their unrealized potential at high temperatures and high loading speeds makes them promising and applicable for extreme environments.

With respect of spallation failure, similar to dynamic compression/tensile tests, most of the research was performed on 3d-transition HEA, while this field of study stays vastly inadequate for BCC RHEAs. Existing studies claim that spallation in HEAs is significantly influenced by second-phase formation. Further studies need to be done to thoroughly understand how voids and cracks evolve within HEA alloys during spallation.

4.1. *Applications*

In contrast to the conventional materials, unique characteristics and complex constituent compositions renders HEAs superior in many aspects, such as great resistance to strength-ductility trade-off, spallation resistance, thermal stability, and highly tunable properties, which make them versatile for a broad range of applications. Some of them are discussed below.

4.1.1. *Armor materials*

Armor is classified, in a simplified manner, into body (personal) and heavy (armored vehicles). The requirements and the projectile-defeating mechanisms are very different. Armor materials are known to be extremely demanding in terms of their resistance to the high strain-rate loading which not merely requires strength but also involves complex thermomechanical processes, in order to minimize damage from a projectile. Superior modern armor is composed of different layers including ceramic, metallic, and polymeric materials. Armors use a range of stratagems: specially developed steels, polyamide, polyethylene, and ceramics are some of the materials. Kevlar (poly-para-phenylene terephthalamide) is a flexible body armor material with a very low density and enables the wearer to retain excellent agility. However, the materials mentioned above have to provide protection against a projectile with mass and flying speeds over 10 g and 850 m/s, respectively, if they are to be satisfactory body armors. With superior strength found in dynamic compression/tensile tests and excellent hardening capacity found in ballistic impact tests, HEAs undoubtedly become one of most competent candidates for the metallic component of armor. The transition in deformation mode at higher strain-rate endows excellent strain hardening ability of HEAs under ultra-high loading rate. Moreover, the high strain rate sensitivity also contributes to enhanced strength at high strain rate condition.

4.1.2. *Nuclear energy materials*

Given by its high efficiency, economy, environmental friendliness, nuclear energy has become more and more popular, with vast amounts of effort devoted to the structural materials in nuclear reactors. Ni-based alloys, zirconium-based alloys, and stainless steels are widely used. Under atmosphere of intense irradiation with flux of neutrons and protons, severe swelling and spalling failure can occur. Irradiation damage can induce defects such as hydrogen and helium bubbles (voids). Refractory HEAs have obtained substantial amount of attention for their relatively inert characteristics due to lack of activity of the refractory elements, which make them promising candidates as next generation nuclear energy materials. The good spallation resistance of HEAs suggests the unrealized potential to endure extreme radiation damage.

4.1.3. *Aerospace materials*

In the aerospace industry, the structural components of turbine engines are among the most demanding environments for materials, requiring high stability, high strength, and excellent fracture strength. Contemporary aerospace materials including Fe-based, Ni-based, Ti-based and Co-based superalloys exhibit poor stability at elevated temperature. Refractory HEAs such as TaNbHfZrTi HEA and TiHfZrTaNb, have intrinsically high melting points and high configurational entropies. These endow them with outstanding stability at high temperature. One major shortcoming for the application of refractory HEAs is the undeniably high expense and their challenging processing. Therefore, besides traditional fabrication method, laser additive manufacturing as one of the latest developed processing techniques, provides defect-free components, which make HEAs more durable [225].

Declaration of Competing Interest

The authors declare that they have no known competing financial interests or personal relationships that could have appeared to influence the work reported in this paper.

REFERENCES

[1] Yeh J-W, Chen S-K, Lin S-J, Gan J-Y, Chin T-S, Shun T-T, et al. Nanostructured High-entropy alloys with multiple principal elements: Novel Alloy Design Concepts and outcomes. Adv Eng Mater 2004;6:299–303. https://doi.org/10.1002/adem.200300567.

[2] Cantor B, Chang ITH, Knight P, Vincent AJB. Microstructural development in equiatomic multicomponent alloys. Mater

Sci Eng Jul. 2004;375–377:213–8. https://doi.org/10.1016/j.msea.2003.10.257. 1-2 SPEC. ISS.
[3] Gali A, George EP. "Tensile properties of high- and medium-entropy alloys,". Intermetallics 2013;39:74–8. https://doi.org/10.1016/j.intermet.2013.03.018.
[4] Bernd G, Anton H, Dhiraj C, H CE, P GE, O RR. A fracture-resistant high-entropy alloy for cryogenic applications. Science Sep. 2014;345(6201):1153–8. https://doi.org/10.1126/science.1254581. 1979.
[5] Stepanov N, Tikhonovsky M, Yurchenko N, Zyabkin D, Klimova M, Zherebtsov S, et al. Effect of cryo-deformation on structure and properties of CoCrFeNiMn high-entropy alloy. Intermetallics 2015;59:8–17. https://doi.org/10.1016/j.intermet.2014.12.004.
[6] Otto F, Hanold NL, George EP. Microstructural evolution after thermomechanical processing in an equiatomic, single-phase CoCrFeMnNi high-entropy alloy with special focus on twin boundaries. Intermetallics Nov. 2014;54:39–48. https://doi.org/10.1016/J.INTERMET.2014.05.014.
[7] Chen W, Fu Z, Fang S, Xiao H, Zhu D. Alloying behavior, microstructure and mechanical properties in a $FeNiCrCo_{0.3}Al_{0.7}$ high entropy alloy. Mater Des Oct. 2013;51:854–60. https://doi.org/10.1016/J.MATDES.2013.04.061.
[8] Wang FJ, Zhang Y. Effect of Co addition on crystal structure and mechanical properties of $Ti_{0.5}$CrFeNiAlCo high entropy alloy. Mater Sci Eng, A Nov. 2008;496(1–2):214–6. https://doi.org/10.1016/J.MSEA.2008.05.020.
[9] Yeh JW, Chen YL, Lin SJ, Chen SK. High-Entropy alloys – a new era of exploitation. Mater Sci Forum 2007;560. https://doi.org/10.4028/www.scientific.net/msf.560.1.
[10] Feng R, Gao M, Lee C, Mathes M, Zuo T, Chen S, et al. Design of light-weight high-entropy alloys. Entropy 2016;18:333. https://doi.org/10.3390/e18090333.
[11] Pickering EJ, Muñoz-Moreno R, Stone HJ, Jones NG. Precipitation in the equiatomic high-entropy alloy CrMnFeCoNi. Scripta Mater Mar. 2016;113:106–9. https://doi.org/10.1016/J.SCRIPTAMAT.2015.10.025.
[12] Otto F, Yang Y, Bei H, George EP. Relative effects of enthalpy and entropy on the phase stability of equiatomic high-entropy alloys. Acta Mater 2013;61(7). https://doi.org/10.1016/j.actamat.2013.01.042.
[13] An Z, Jia H, Wu Y, Rack PD, Patchen AD, Liu Y, et al. Solid-solution CrCoCuFeNi high-entropy alloy thin films synthesized by sputter deposition. Mater Res Lett 2015;3:203–9. https://doi.org/10.1080/21663831.2015.1048904.
[14] Lee C, Chou Y, Kim G, Gao MC, An K, Brechtl J, et al. Lattice-distortion-enhanced yield strength in a refractory high-entropy alloy. Adv Mater 2020;32:2004029. https://doi.org/10.1002/adma.202004029.
[15] Lee C, Song G, Gao MC, Feng R, Chen P, Brechtl J, et al. Lattice distortion in a strong and ductile refractory high-entropy alloy. Acta Materialia 2018;160:158–72. https://doi.org/10.1016/j.actamat.2018.08.053.
[16] Oh H, Ma D, Leyson G, Grabowski B, Park E, Körmann F, et al. Lattice distortions in the FeCoNiCrMn high entropy alloy studied by theory and experiment. Entropy 2016;18:321. https://doi.org/10.3390/e18090321.
[17] Owen LR, Pickering EJ, Playford HY, Stone HJ, Tucker MG, Jones NG. An assessment of the lattice strain in the CrMnFeCoNi high-entropy alloy. Acta Mater Jan. 2017;122:11–8. https://doi.org/10.1016/J.ACTAMAT.2016.09.032.
[18] Ranganathan S. Alloyed pleasures multimetallic cocktails. Curr Sci 2003;85(10):1404–6.
[19] Schönfeld B. Local atomic arrangements in binary alloys. Prog Mater Sci 1999;44(5). https://doi.org/10.1016/s0079-6425(99)00005-5.
[20] Clément N, Caillard D, Martin JL. Heterogeneous deformation of concentrated Ni Cr F.C.C. alloys: macroscopic and microscopic behaviour. Acta Metall Jun. 1984;32(6):961–75. https://doi.org/10.1016/0001-6160(84)90034-8.
[21] Dubiel SM, Cieslak J. Short-range order in iron-rich Fe-Cr alloys as revealed by Mössbauer spectroscopy. Phys Rev B Condens Matter 2011;83(18). https://doi.org/10.1103/PhysRevB.83.180202.
[22] Fernández-Caballero A, Wróbel JS, Mummery PM, Nguyen-Manh D. Short-range order in high entropy alloys: theoretical formulation and application to Mo-Nb-Ta-V-W system. J Phase Equilibria Diffus 2017;38(4). https://doi.org/10.1007/s11669-017-0582-3.
[23] Huang X, Liu L, Duan X, Liao W, Huang J, Sun H, et al. Atomistic simulation of chemical short-range order in HfNbTaZr high entropy alloy based on a newly-developed interatomic potential. Mater Des 2021;202:109560. https://doi.org/10.1016/j.matdes.2021.109560.
[24] Antillon E, Woodward C, Rao SI, Akdim B, Parthasarathy TA. Chemical short range order strengthening in a model FCC high entropy alloy. Acta Mater 2020;190. https://doi.org/10.1016/j.actamat.2020.02.041.
[25] Linden Y, Pinkas M, Munitz A, Meshi L. Long-period antiphase domains and short-range order in a B2 matrix of the Alcocrfeni High-entropy alloy. Scripta Materialia 2017;139:49–52. https://doi.org/10.1016/j.scriptamat.2017.06.015.
[26] Santodonato LJ, Zhang Y, Feygenson M, Parish CM, Gao MC, Weber RJK, et al. Deviation from high-entropy configurations in the atomic distributions of a multi-principal-element alloy. Nat Commun 2015;6. https://doi.org/10.1038/ncomms6964.
[27] Zhang FX, Zhao S, Jin K, Xue H, Velisa G, Bei H, et al. Local structure and short-range order in a NiCoCr solid solution alloy. Phys Rev Lett 2017;118. https://doi.org/10.1103/physrevlett.118.205501.
[28] Schönfeld B, Sax CR, Zemp J, Engelke M, Boesecke P, Kresse T, et al. Local order in Cr-Fe-Co-Ni: experiment and electronic structure calculations. Phys Rev B 2019;99. https://doi.org/10.1103/physrevb.99.014206.
[29] Zhang R, Zhao S, Ding J, Chong Y, Jia T, Ophus C, et al. Short-range order and its impact on the CrCoNi medium-entropy alloy. Nature 2020;581:283–7. https://doi.org/10.1038/s41586-020-2275-z.
[30] Ding J, Yu Q, Asta M, Ritchie RO. Tunable stacking fault energies by tailoring local chemical order in CrCoNi medium-entropy alloys. Proc Natl Acad Sci U S A 2018;115(36):8919–8924, Sep. https://doi.org/10.1073/pnas.1808660115.
[31] Ye YF, Wang Q, Lu J, Liu CT, Yang Y. High-entropy alloy: challenges and prospects. Mater Today Jul. 01, 2016;19(6):349–62. https://doi.org/10.1016/j.mattod.2015.11.026. Elsevier B.V.
[32] (Rusty) Gray GT. High-strain-rate deformation: mechanical behavior and deformation substructures induced. Annu Rev Mater Res 2012;42:285–303. https://doi.org/10.1146/annurev-matsci-070511-155034.
[33] Gerold' V, Karnthaler' HP. On the origin of planar slip in F.C.C.. ALLOYS; 1989.
[34] Clifton RJ. High strain rate behavior of metals. Appl Mech Rev 1990;43. https://doi.org/10.1115/1.3120862.
[35] Meyers MA. Dynamic behavior of materials. John Wiley & Sons; 1994. p. 488–566. https://doi.org/10.1002/9780470172278.ch16.

[36] Couque H. The use of the direct impact Hopkinson pressure bar technique to describe thermally activated and viscous regimes of metallic materials. Phil Trans Math Phys Eng Sci 2014;372. https://doi.org/10.1098/rsta.2013.0218. 2023.
[37] Kumar N, Ying Q, Nie X, Mishra RS, Tang Z, Liaw PK, et al. High strain-rate compressive deformation behavior of the $Al_{0.1}$CrFeCoNi High Entropy Alloy. Mater Des 2015;86:598–602. https://doi.org/10.1016/j.matdes.2015.07.161.
[38] Kravchenko VY. Effect of directed electron beam on moving dislocations. Sov Phys - JETP 1967;24(6).
[39] Otto F, Dlouhý A, Somsen C, Bei H, Eggeler G, George EP. The influences of temperature and microstructure on the tensile properties of a CoCrFeMnNi high-entropy alloy. Acta Mater 2013;61(15). https://doi.org/10.1016/j.actamat.2013.06.018.
[40] Wu Z, Bei H, Pharr GM, George EP. Temperature dependence of the mechanical properties of equiatomic solid solution alloys with face-centered cubic crystal structures. Acta Mater 2014;81. https://doi.org/10.1016/j.actamat.2014.08.026.
[41] Leyson GPM, Hector LG, Curtin WA. Solute strengthening from first principles and application to aluminum alloys. Acta Mater 2012;60(9). https://doi.org/10.1016/j.actamat.2012.03.037.
[42] Leyson GPM, Hector LG, Curtin WA. First-principles prediction of yield stress for basal slip in Mg-Al alloys. Acta Mater 2012;60:13–4. https://doi.org/10.1016/j.actamat.2012.06.020.
[43] Laplanche G, Bonneville J, Varvenne C, Curtin WA, George EP. Thermal activation parameters of plastic flow reveal deformation mechanisms in the CrMnFeCoNi high-entropy alloy. Acta Mater Jan. 2018;143:257–64. https://doi.org/10.1016/j.actamat.2017.10.014.
[44] Meyers MA, Armstrong Ronald W, Kirchner Helmut OK. Mechanics and materials: fundamentals and linkages. Wiley VCH; 1999.
[45] Gali A, George EP. Tensile properties of high- and medium-entropy alloys. Intermetallics 2013;39. https://doi.org/10.1016/j.intermet.2013.03.018.
[46] Fan Y, Osetsky YN, Yip S, Yildiz B. Onset mechanism of strain-rate-induced flow stress upturn. Phys Rev Lett 2012;109(13). https://doi.org/10.1103/PhysRevLett.109.135503.
[47] Johnson GR, Hoegfeldt JM, Lindholm US, Nagy A. Response of various metals to large torsional strains over a large range of strain rates-part 2: less ductile metals. J Eng Mater Techno Trans ASME 1983;105(1). https://doi.org/10.1115/1.3225618.
[48] Zerilli FJ, Armstrong RW. Dislocation-mechanics-based constitutive relations for material dynamics calculations. J Appl Phys 1987;61(5). https://doi.org/10.1063/1.338024.
[49] Armstrong RW, Arnold W, Zerilli FJ. Dislocation mechanics of copper and iron in high rate deformation tests. J Appl Phys 2009;105(2). https://doi.org/10.1063/1.3067764.
[50] Hoge KG, Mukherjee AK. The temperature and strain rate dependence of the flow stress of tantalum. J Mater Sci 1977;12(8). https://doi.org/10.1007/BF00542818.
[51] Balakrishna Bhat T, Arunachalam VS. Strengthening mechanisms in alloys. Pro India Acad Sci: Eng Sci 1980;3(4). https://doi.org/10.1007/BF02842915.
[52] Gil Sevillano J, van Houtte P, Aernoudt E. Large strain work hardening and textures. Prog Mater Sci 1980;25(2–4). https://doi.org/10.1016/0079-6425(80)90001-8.
[53] Edington JW. The distribution of dislocations in specimens of niobium and copper after deformation in the Hopkinson bar. Trans. Metall. Soc. AIME 1969;245:1653–64.
[54] Tsai S-P, Tsai Y-T, Chen Y-W, Chen P-J, Chiu P-H, Chen C-Y, et al. High-entropy CoCrFeMnNi alloy subjected to high-strain-rate compressive deformation. Mater Char 2019;147:193–8. https://doi.org/10.1016/j.matchar.2018.10.028.
[55] Gutierrez-Urrutia I, Raabe D. Study of deformation twinning and planar slip in a TWIP steel by electron channeling contrast imaging in a SEM. Mater Sci Forum 2012:702–3. https://doi.org/10.4028/www.scientific.net/MSF.702-703.523.
[56] Zhang Z, Sheng H, Wang Z, Gludovatz B, Zhang Z, George EP, et al. Dislocation mechanisms and 3D twin architectures generate exceptional strength-ductility-toughness combination in CrCoNi medium-entropy alloy. Nat Commun 2017;8. https://doi.org/10.1038/ncomms14390.
[57] Hong SI, Laird C. Mechanisms of slip mode modification in F.C.C. solid solutions. Acta Metall Mater 1990;38(8). https://doi.org/10.1016/0956-7151(90)90126-2.
[58] Wong SK, Shun TT, Chang CH, Lee CF. Microstructures and properties of $Al_{0.3}$CoCrFeNiMnx high-entropy alloys. Mater Chem Phys 2018;210. https://doi.org/10.1016/j.matchemphys.2017.07.085.
[59] Clouet E. The vacancy-edge dislocation interaction in fcc metals: a comparison between atomic simulations and elasticity theory. Acta Mater 2006;54(13). https://doi.org/10.1016/j.actamat.2006.03.043.
[60] Yasi JA, Hector LG, Trinkle DR. First-principles data for solid-solution strengthening of magnesium: from geometry and chemistry to properties. Acta Mater 2010;58(17). https://doi.org/10.1016/j.actamat.2010.06.045.
[61] Fleischer RL. Substitutional solution hardening. Acta Metall 1963;11(3). https://doi.org/10.1016/0001-6160(63)90213-X.
[62] Fleischer RL. Solution hardening. Acta Metallurgica 1961;9:996–1000. https://doi.org/10.1016/0001-6160(61)90242-5.
[63] Friedel J. Discolations, vol. 3. Pergamon Press; 1967.
[64] Labusch R. A statistical theory of solid solution hardening. Phys Status Solidi 1970;41(2). https://doi.org/10.1002/pssb.19700410221.
[65] Labusch R. Statistische theorien der mischkristallhärtung. Acta Metall 1972;20(7). https://doi.org/10.1016/0001-6160(72)90085-5.
[66] Mott NF. CXVII. A theory of work-hardening of metal crystals. The London, Edinburgh, and Dublin Philosophical Magazine and Journal of Science 1952;43. https://doi.org/10.1080/14786441108521024. 346.
[67] Toda-Caraballo I, Wróbel JS, Dudarev SL, Nguyen-Manh D, Rivera-Díaz-Del-Castillo PEJ. Interatomic spacing distribution in multicomponent alloys. Acta Mater 2015;97. https://doi.org/10.1016/j.actamat.2015.07.010.
[68] Toda-Caraballo I, Rivera-Díaz-Del-Castillo PEJ. Modelling solid solution hardening in high entropy alloys. Acta Mater 2015;85. https://doi.org/10.1016/j.actamat.2014.11.014.
[69] Gypen LA, Deruyttere A. Multi-component solid solution hardening - Part 1 Proposed model. J Mater Sci 1977;12(5). https://doi.org/10.1007/BF00540987.
[70] Toda-Caraballo I. A general formulation for solid solution hardening effect in multicomponent alloys. Scripta Mater 2017;127. https://doi.org/10.1016/j.scriptamat.2016.09.009.
[71] Varvenne C, Leyson GPM, Ghazisaeidi M, Curtin WA. Solute strengthening in random alloys. Acta Mater 2017;124. https://doi.org/10.1016/j.actamat.2016.09.046.
[72] Varvenne C, Luque A, Curtin WA. Theory of strengthening in fcc high entropy alloys. Acta Mater 2016;118. https://doi.org/10.1016/j.actamat.2016.07.040.
[73] Brown LM. Strengthening mechanisms in crystal plasticity, by Ali argon. Contemp Phys 2013;54(6). https://doi.org/10.1080/00107514.2013.857723.
[74] Trinkle DR, Woodward C. Materials science: the chemistry of deformation: how solutes soften pure metals. Science

2005;310:5754. https://doi.org/10.1126/science.1118616. 1979.
[75] Maresca F, Curtin WA. Mechanistic origin of high strength in refractory BCC high entropy alloys up to 1900K. Acta Mater 2020;182. https://doi.org/10.1016/j.actamat.2019.10.015.
[76] Senkov ON, Scott JM, Senkova SV, Miracle DB, Woodward CF. Microstructure and room temperature properties of a high-entropy TaNbHfZrTi alloy. J Alloys Compd 2011;509(20). https://doi.org/10.1016/j.jallcom.2011.02.171.
[77] Yao HW, Qiao JW, Hawk JA, Zhou HF, Chen MW, Gao MC. Mechanical properties of refractory high-entropy alloys: experiments and modeling. J Alloys Compd 2017;696. https://doi.org/10.1016/j.jallcom.2016.11.188.
[78] Coury FG, Kaufman M, Clarke AJ. Solid-solution strengthening in refractory high entropy alloys. Acta Mater 2019;175. https://doi.org/10.1016/j.actamat.2019.06.006.
[79] Coury FG, Clarke KD, Kiminami CS, Kaufman MJ, Clarke AJ. High throughput discovery and design of strong multicomponent metallic solid solutions. Sci Rep 2018;8(1). https://doi.org/10.1038/s41598-018-26830-6.
[80] Schuh B, Mendez-Martin F, Völker B, George EP, Clemens H, Pippan R, et al. Mechanical properties, microstructure and thermal stability of a nanocrystalline CoCrFeMnNi high-entropy alloy after severe plastic deformation. Acta Materialia 2015;96:258–68. https://doi.org/10.1016/j.actamat.2015.06.025.
[81] Gangireddy S, Gwalani B, Mishra RS. Grain size dependence of strain rate sensitivity in a single phase FCC high entropy alloy $Al_{0.3}$CoCrFeNi. Mater Sci Eng 2018;736. https://doi.org/10.1016/j.msea.2018.09.009.
[82] Babyak WJ, Rhines FN. The relationship between the boundary area and hardness of recrysallized cartridge brass. Trans Metall Soc AIME 1960;218(1):21–3.
[83] Zhu T, Gao H. Plastic deformation mechanism in nanotwinned metals: an insight from molecular dynamics and mechanistic modeling. Scripta Mater 2012;66(11). https://doi.org/10.1016/j.scriptamat.2012.01.031.
[84] You Z, Li X, Gui L, Lu Q, Zhu T, Gao H, et al. Plastic anisotropy and associated deformation mechanisms in nanotwinned metals. Acta Materialia 2013;61:217–27. https://doi.org/10.1016/j.actamat.2012.09.052.
[85] Lu K, Lu L, Suresh S. Strengthening materials by engineering coherent internal boundaries at the nanoscale. Science 2009;324:5925. https://doi.org/10.1126/science.1159610.
[86] Shen YF, Lu L, Lu QH, Jin ZH, Lu K. Tensile properties of copper with nano-scale twins. Scripta Mater 2005;52(10). https://doi.org/10.1016/j.scriptamat.2005.01.033.
[87] Wang YB, Wu B, Sui ML. Dynamical dislocation emission processes from twin boundaries. Appl Phys Lett 2008;93(4). https://doi.org/10.1063/1.2965637.
[88] Zhu YT, Narayan J, Hirth JP, Mahajan S, Wu XL, Liao XZ. Formation of single and multiple deformation twins in nanocrystalline fcc metals. Acta Mater 2009;57(13). https://doi.org/10.1016/j.actamat.2009.04.020.
[89] Li N, Wang J, Misra A, Zhang X, Huang JY, Hirth JP. Twinning dislocation multiplication at a coherent twin boundary. Acta Mater 2011;59(15). https://doi.org/10.1016/j.actamat.2011.06.007.
[90] Jin Z-H, Gumbsch P, Ma E, Albe K, Lu K, Hahn H, et al. The interaction mechanism of screw dislocations with coherent twin boundaries in different face-centred cubic metals. Scripta Materialia 2006;54:1163–8. https://doi.org/10.1016/j.scriptamat.2005.11.072.
[91] Jin Z-H, Gumbsch P, Albe K, Ma E, Lu K, Gleiter H, et al. Interactions between non-screw lattice dislocations and coherent twin boundaries in face-centered cubic metals. Acta Materialia 2008;56:1126–35. https://doi.org/10.1016/j.actamat.2007.11.020.
[92] Meyers MA, Vöhringer O, Lubarda VA. The onset of twinning in metals: a constitutive description. Acta Materialia 2001;49:4025–39. https://doi.org/10.1016/s1359-6454(01)00300-7.
[93] Narita N, Takamura J. Deformation twinning in fcc and bcc metals. Dislocations Solids 1992;9:135–89.
[94] Gray GTIII, Kaschner GC, Mason T. The influence of interstitial content, temperature, and strain rate on deformation twin formation. Adv Twin 1999:157–70.
[95] Smith CS. Metallographic studies of metals after explosive shock. Trans. AIME 1958;212.
[96] Yoo MH. Slip, twinning, and fracture in hexagonal close-packed metals. Metall Trans A 1981;12(3). https://doi.org/10.1007/BF02648537.
[97] Seeger A. Mechanical twinning of crystalsKlassen-Neklyudova MV, editor. Acta Crystallogr 1966;20(2). https://doi.org/10.1107/s0365110x66000732.
[98] Gallagher PCJ. The influence of alloying, temperature, and related effects on the stacking fault energy. Metall Trans A 1970;1(9). https://doi.org/10.1007/BF03038370.
[99] Deng Y, Tasan CC, Pradeep KG, Springer H, Kostka A, Raabe D. Design of a twinning-induced plasticity high entropy alloy. Acta Mater May 2015;94:124–33. https://doi.org/10.1016/j.actamat.2015.04.014.
[100] Ren B, Liu ZX, Cai B, Wang MX, Shi L. Aging behavior of a $CuCr_2Fe_2NiMn$ high-entropy alloy. Mater Des 2012;33(1). https://doi.org/10.1016/j.matdes.2011.07.005.
[101] Chen S-T, Tang W-Y, Kuo Y-F, Chen S-Y, Tsau C-H, Shun T-T, et al. Microstructure and properties of age-hardenable $Al_xCrFe_{1.5}MnNi_{0.5}$ alloys. Mater Sci Eng A 2010;527:5818–25. https://doi.org/10.1016/j.msea.2010.05.052.
[102] Liu WH, Yang T, Liu CT. Precipitation hardening in CoCrFeNi-based high entropy alloys. Mater Chem Phys 2018;210. https://doi.org/10.1016/j.matchemphys.2017.07.037.
[103] Eißmann N, Mühle U, Gaitzsch U, Walther G, Weißgärber T, Kieback B. Precipitation hardening of high entropy alloy CoCrFeMnNi containing titanium. J Alloys Compd 2021;857. https://doi.org/10.1016/j.jallcom.2020.157610.
[104] He JY, Wang H, Huang HL, Xu XD, Chen MW, Wu Y, et al. A precipitation-hardened high-entropy alloy with outstanding tensile properties. Acta Materialia 2016;102:187–96. https://doi.org/10.1016/j.actamat.2015.08.076.
[105] Moon J, Qi Y, Tabachnikova E, Estrin Y, Choi W-M, Joo S-H, et al. Deformation-induced phase transformation of $Co_{20}Cr_{26}Fe_{20}Mn_{20}Ni_{14}$ high-entropy alloy during high-pressure torsion at 77 K. Mater Lett 2017;202:86–8. https://doi.org/10.1016/j.matlet.2017.05.065.
[106] Lin Q, Liu J, An X, Wang H, Zhang Y, Liao X. Cryogenic-deformation-induced phase transformation in an FeCoCrNi high-entropy alloy. Materials Research Letters 2018;6(4). https://doi.org/10.1080/21663831.2018.1434250.
[107] Huang E-W, Lin C-M, Jain J, Shieh SR, Wang C-P, Chuang Y-C, et al. Irreversible phase transformation in a CoCrFeMnNi high entropy alloy under hydrostatic compression. Mater Today Commun 2018;14:10–4. https://doi.org/10.1016/j.mtcomm.2017.12.001.
[108] Zhao C, Li J, Liu Y, Wang WY, Kou H, Beaugnon E, et al. Tailoring mechanical and magnetic properties of AlCoCrFeNi High-entropy alloy via phase transformation. J

Mater Sci Technol 2021;73:83–90. https://doi.org/10.1016/j.jmst.2020.08.063.
[109] Zhao S, Li Z, Zhu C, Yang W, Zhang Z, Armstrong DE, et al. Amorphization in extreme deformation of the CrMnFeCoNi high-entropy alloy. Sci Adv 2021;7. https://doi.org/10.1126/sciadv.abb3108.
[110] Wang H, Chen D, An X, Zhang Y, Sun S, Tian Y, et al. Deformation-induced crystalline-to-amorphous phase transformation in a CrMnFeCoNi high-entropy alloy. Sci Adv 2021;7. https://doi.org/10.1126/sciadv.abe3105.
[111] H. Kolsky, "An investigation of the mechanical properties of materials at very high rates of loading."
[112] Kolsky H. Stress waves in solids. J Sound Vib 1964;1(1). https://doi.org/10.1016/0022-460X(64)90008-2.
[113] Hauser FE. Techniques for measuring stress-strain relations at high strain rates. Exp Mech 1966;6(8). https://doi.org/10.1007/bf02326284.
[114] Lindholm US, Yeakley LM. High strain-rate testing: tension and compression. Exp Mech 1968;8(no. 1). https://doi.org/10.1007/bf02326244.
[115] Chiddister JL, Malvern LE. Compression-impact testing of aluminum at elevated temperatures. Exp Mech 1963;3(4). https://doi.org/10.1007/bf02325890.
[116] Baker WE, Yew CH. Strain-rate effects in the propagation of torsional plastic waves 1 [Online]. Available: http://asmedigitalcollection.asme.org/appliedmechanics/article-pdf/33/4/917/5447998/917_1.pdf; 1966.
[117] Meyers MA, Andrade UR, Chokshi AH. The effect of grain size on the high-strain, high-strain-rate behavior of copper. Metall Mater Trans 1995;26(11). https://doi.org/10.1007/BF02669646.
[118] Meyers MA, Xu YB, Xue Q, Pérez-Prado MT, McNelley TR. Microstructural evolution in adiabatic shear localization in stainless steel. Acta Mater 2003;51(5). https://doi.org/10.1016/S1359-6454(02)00526-8.
[119] Mishra B, Mondal C, Goyal R, Ghosal P, Kumar KS, Madhu V. Plastic flow behavior of 7017 and 7055 aluminum alloys under different high strain rate test methods. Mater Sci Eng 2014;612. https://doi.org/10.1016/j.msea.2014.06.037.
[120] Andrade U, Meyers MA, Vecchio KS, Chokshi AH. Dynamic recrystallization in high-strain, high-strain-rate plastic deformation of copper. Acta Metall Mater 1994;42(9). https://doi.org/10.1016/0956-7151(94)90417-0.
[121] Peirs J, Tirry W, Amin-Ahmadi B, Coghe F, Verleysen P, Rabet L, et al. Microstructure of adiabatic shear bands in Ti-6Al-4V. Mater Char 2013;75:79–92. https://doi.org/10.1016/j.matchar.2012.10.009.
[122] Li QM, Jones N. Response and failure of a double-shear beam subjected to mass impact. Int J Solid Struct 2002;39(7). https://doi.org/10.1016/S0020-7683(02)00004-5.
[123] Glema A, Łodygowski T, Sumelka W. Nowacki's double shear test in the framework of the anisotropic thermo-elasto-viscoplastic material model. J Theor Appl Mech 2010;48(4).
[124] Klepaczko JR. An experimental technique for shear testing at high and very high strain rates. The case of a mild steel. Int J Impact Eng 1994;15(1). https://doi.org/10.1016/S0734-743X(05)80005-3.
[125] Kalthoff JF. Transition in the failure behawior of dynamically shear loaded cracks [Online]. Available: http://asmedigitalcollection.asme.org/appliedmechanicsreviews/article-pdf/43/5S/S247/5435877/s247_1.pdf; 1990.
[126] Kalthoff JF. Modes of dynamic shear failure in solids. Int J Fract 2000;101:1–2. https://doi.org/10.1023/a:1007647800529.
[127] Zhou M, Ravichandran G, Rosakis AJ. Dynamically propagating shear bands in impact-loaded prenotched plates - II. Numerical simulations. J Mech Phys Solid 1996;44(6). https://doi.org/10.1016/0022-5096(96)00004-X.
[128] Zhou M, Rosakis AJ, Ravichandran G. Dynamically propagating shear bands in impact-loaded prenotched plates - I. Experimental investigations of temperature signatures and propagation speed. J Mech Phys Solid 1996;44(6). https://doi.org/10.1016/0022-5096(96)00003-8.
[129] Gray GT, Vecchio KS, Livescu V. Compact forced simple-shear sample for studying shear localization in materials. Acta Mater 2016;103. https://doi.org/10.1016/j.actamat.2015.09.051.
[130] Nesterenko VF, Meyers MA, LaSalvia JC, Bondar MP, Chen YJ, Lukyanov YL. Shear localization and recrystallization in high-strain, high-strain-rate deformation of tantalum. Mater Sci Eng 1997;229(1–2). https://doi.org/10.1016/s0921-5093(96)10847-9.
[131] Chen RW, Vecchio KS. Microstructural characterization of shear band formation in Al-Li alloys. J Phys IV : JP 1994;4. https://doi.org/10.1051/jp4:1994871. C8.
[132] Lee WS, Sue WC, Lin CF, Wu CJ. Strain rate and temperature dependence of the dynamic impact properties of 7075 aluminum alloy. J Mater Process Technol 2000;100(1). https://doi.org/10.1016/S0924-0136(99)00465-3.
[133] A. Molinari, C. Musquar, and G. Sutter, "Adiabatic shear banding in high speed machining of Ti-6Al-4V: experiments and modeling." [Online]. Available: www.elsevier.com/locate/ijplas
[134] Culver RS. Thermal instability strain in dynamic plastic deformation. 1973. https://doi.org/10.1007/978-1-4615-8696-8_29.
[135] Clifton RJ, Duffy J, Hartley KA, Shawki TG. On critical conditions for shear band formation at high strain rates. Scripta Metall 1984;18(5). https://doi.org/10.1016/0036-9748(84)90418-6.
[136] Lindholm US. Review of dynamic testing techniques and material behavior. Mechanical properties at high rates of strain 1974.
[137] Meyers MA, Subhash G, Kad BK, Prasad L. Evolution of microstructure and shear-band formation in α-hcp titanium. Mech Mater 1994;17(2–3). https://doi.org/10.1016/0167-6636(94)90058-2.
[138] Zener C, Hollomon JH. Effect of strain rate upon plastic flow of steel. J Appl Phys 1944;15(1). https://doi.org/10.1063/1.1707363.
[139] Molinari A, Clifton RJ. Analytical characterization of shear localization in thermoviscoplastic materials. Journal of Applied Mechanics, Transactions ASME 1987;54(4). https://doi.org/10.1115/1.3173121.
[140] Dirras G, Ota M, Tingaud D, Ameyama K, Sekiguchi T. Microstructure evolution during direct impact loading of commercial purity α -titanium with harmonic structure design: direct impact loading of pure harmonic α -Ti. Matériaux Tech 2015;103(3). https://doi.org/10.1051/mattech/2015031.
[141] Lins JFC, Sandim HRZ, Kestenbach HJ, Raabe D, Vecchio KS. A microstructural investigation of adiabatic shear bands in an interstitial free steel. Mater Sci Eng 2007;457(1–2). https://doi.org/10.1016/j.msea.2006.12.019.
[142] Meyers MA, Pak HR. Observation of an adiabatic shear band in titanium by high-voltage transmission electron microscopy. Acta Metall 1986;34(12). https://doi.org/10.1016/0001-6160(86)90152-5.
[143] Hines JA, Vecchio KS, Ahzi S. A model for microstructure evolution in adiabatic shear bands. Metall Mater Trans A 1998;29(1). https://doi.org/10.1007/s11661-998-0172-4.
[144] Meyers MA, LaSalvia JC, Nesterenko VF, Chen Y, Kad B. Dynamic recrystallization in high-strain-rate deformation, in "Recrystallization and Related Phenomena", Ed. J.R. McNelley, 279–286. Proc Rex, 96 Monterey 1997.

[145] Li Z, Zhao S, Diao H, Liaw PK, Meyers MA. High-velocity deformation of $Al_{0.3}$CoCrFeNi high-entropy alloy: remarkable resistance to shear failure. Sci Rep Feb. 2017;7. https://doi.org/10.1038/srep42742.
[146] Tang QH, Huang Y, Huang YY, Liao XZ, Langdon TG, Dai PQ. Hardening of an $Al_{0.3}$CoCrFeNi high entropy alloy via high-pressure torsion and thermal annealing. Mater Lett 2015;151. https://doi.org/10.1016/j.matlet.2015.03.066.
[147] Wang L, Qiao JW, Ma SG, Jiao ZM, Zhang TW, Chen G, et al. Mechanical response and deformation behavior of $Al_{0.6}$CoCrFeNi high-entropy alloys upon dynamic loading. Mater Sci Eng A 2018;727:208–13. https://doi.org/10.1016/j.msea.2018.05.001.
[148] Park J, Kang M, Sohn SS, Kim S-H, Kim HS, Kim NJ, et al. Quasi-static and dynamic deformation mechanisms interpreted by microstructural evolution in twinning induced plasticity (TWIP) steel. Mater Sci Eng A 2017;684:54–63. https://doi.org/10.1016/j.msea.2016.12.037.
[149] Liu G, Liu L, Liu X, Wang Z, Han Z, Zhang G, et al. Microstructure and mechanical properties of $Al_{0.7}$CoCrFeNi high-entropy-alloy prepared by directional solidification. Intermetallics 2018;93:93–100. https://doi.org/10.1016/j.intermet.2017.11.019.
[150] Bartholomeusz MF, Cantrell MA, Wert JA. The enhanced work hardening rates of the constituent TiAl and Ti_3Al phases in a lamellar microstructure. Mater Sci Eng 1995;201(1–2). https://doi.org/10.1016/0921-5093(95)09779-1.
[151] de Formanoir C, Brulard A, Vivès S, Martin G, Prima F, Michotte S, et al. A strategy to improve the work-hardening behavior of Ti–6Al–4V parts produced by additive manufacturing. Mater Res Lett 2016;5(3):201–8. https://doi.org/10.1080/21663831.2016.1245681.
[152] Jiao ZM, Ma SG, Chu MY, Yang HJ, Wang ZH, Zhang Y, et al. Superior mechanical properties of AlCoCrFeNiTi_x high-entropy alloys upon dynamic loading. J Mater Eng Perform 2015;25(2):451–6. https://doi.org/10.1007/s11665-015-1869-3.
[153] Jiang L, Lu Y, Dong Y, Wang T, Cao Z, Li T. Annealing effects on the microstructure and properties of bulk high-entropy CoCrFeNi$Ti_{0.5}$ alloy casting ingot. Intermetallics 2014;44. https://doi.org/10.1016/j.intermet.2013.08.016.
[154] Lu Y, Dong Y, Guo S, Jiang L, Kang H, Wang T, et al. A promising new class of high-temperature alloys: eutectic high-entropy alloys. Sci Rep 2014;4(1). https://doi.org/10.1038/srep06200.
[155] Armstrong RW, Walley SM. High strain rate properties of metals and alloys. Int Mater Rev May 2008;53(3):105–28. https://doi.org/10.1179/174328008X277795.
[156] Wang B, Wang C, Liu B, Zhang X. Dynamic mechanical properties and microstructure of an $(Al_{0.5}CoCrFeNi)_{0.95}Mo_{0.025}C_{0.025}$ high entropy alloy. Entropy 2019;21(12). https://doi.org/10.3390/e21121154.
[157] Zhuang YX, Zhang XL, Gu XY. Effect of molybdenum on phases, microstructure and mechanical properties of $Al_{0.5}$CoCrFeMoxNi high entropy alloys. J Alloys Compd 2018;743. https://doi.org/10.1016/j.jallcom.2018.02.003.
[158] Peng J, Li Z, Fu L, Ji X, Pang Z, Shan A. Carbide precipitation strengthening in fine-grained carbon-doped FeCoCrNiMn high entropy alloy. J Alloys Compd 2019;803. https://doi.org/10.1016/j.jallcom.2019.06.204.
[159] Park JM, Moon J, Bae JW, Jang MJ, Park J, Lee S, et al. Strain rate effects of dynamic compressive deformation on mechanical properties and microstructure of CoCrFeMnNi high-entropy alloy. Mater Sci Eng A 2018;719:155–63. https://doi.org/10.1016/j.msea.2018.02.031.
[160] Jang MJ, Ahn D-H, Moon J, Bae JW, Yim D, Yeh J-W, et al. Constitutive modeling of deformation behavior of high-entropy alloys with face-centered cubic crystal structure. Mater Res Lett 2017;5:350–6. https://doi.org/10.1080/21663831.2017.1292325.
[161] Li Z, Zhao S, Alotaibi SM, Liu Y, Wang B, Meyers MA. Adiabatic shear localization in the CrMnFeCoNi high-entropy alloy. Acta Mater Jun. 2018;151:424–31. https://doi.org/10.1016/j.actamat.2018.03.040.
[162] Xue Q, Meyers MA, Nesterenko VF. Self-organization of shear bands in titanium and Ti-6Al-4V alloy [Online]. Available: www.elsevier.com/locate/actamat; 2002.
[163] Wang B, Yao X, Wang C, Zhang X, Huang X. Mechanical properties and microstructure of a NiCrFeCoMn high-entropy alloy deformed at high strain rates. Entropy 2018;20(11). https://doi.org/10.3390/e20110892.
[164] Zhang Y, Liu JP, Chen SY, Xie X, Liaw PK, Dahmen KA, et al. Serration and noise behaviors in materials. Prog Mater Sci 2017;90:358–460. https://doi.org/10.1016/j.pmatsci.2017.06.004.
[165] Portevin A, Chatelier FL. On a phenomenon observed in the tensile testing of alloys during processing. Comp. Rend. Acad. Sci. Paris 1923;176:507.
[166] Hu Q, Zhang Q, Cao P, Fu S. Thermal analyses and simulations of the type A and type B Portevin-Le Chatelier effects in an Al-Mg alloy. Acta Mater 2012;60(4). https://doi.org/10.1016/j.actamat.2011.12.003.
[167] Cai Y, Tian C, Fu S, Han G, Cui C, Zhang Q. Influence of γ' precipitates on Portevin-Le Chatelier effect of Ni-based superalloys. Mater Sci Eng 2015;638. https://doi.org/10.1016/j.msea.2015.04.033.
[168] Fu S, Cheng T, Zhang Q, Hu Q, Cao P. Two mechanisms for the normal and inverse behaviors of the critical strain for the Portevin-Le Chatelier effect. Acta Mater 2012;60(19). https://doi.org/10.1016/j.actamat.2012.08.035.
[169] Wang B, Huang X, Fu A, Liu Y, Liu B. Serration behavior and microstructure of high entropy alloy CoCrFeMnNi prepared by powder metallurgy. Mater Sci Eng May 2018;726:37–44. https://doi.org/10.1016/j.msea.2018.04.071.
[170] Soares GC, Patnamsetty M, Peura P, Hokka M. Effects of adiabatic heating and strain rate on the dynamic response of a CoCrFeMnNi high-entropy alloy. J Dynam Behav Mater Sep. 2019;5(3):320–30. https://doi.org/10.1007/s40870-019-00215-w.
[171] Qiao Y, Chen Y, Cao FH, Wang HY, Dai LH. Dynamic behavior of CrMnFeCoNi high-entropy alloy in impact tension. Int J Impact Eng Dec. 2021;158. https://doi.org/10.1016/j.ijimpeng.2021.104008.
[172] Cao CM, Tong W, Bukhari SH, Xu J, Hao YX, Gu P, et al. Dynamic tensile deformation and microstructural evolution of Al_xCrMnFeCoNi High-entropy alloys. Mater Sci Eng A 2019;759:648–54. https://doi.org/10.1016/j.msea.2019.05.095.
[173] Zhao S, Kad B, Hahn EN, Remington BA, Wehrenberg CE, Huntington CM, et al. Pressure and shear-induced amorphization of Silicon. Extreme Mech Lett 2015;5:74–80. https://doi.org/10.1016/j.eml.2015.10.001.
[174] Gamero-Castaño M, Torrents A, Valdevit L, Zheng JG. Pressure-induced amorphization in silicon caused by the impact of electrosprayed nanodroplets. Phys Rev Lett 2010;105(14). https://doi.org/10.1103/PhysRevLett.105.145701.
[175] Jiang W, Gao X, Guo Y, Chen X, Zhao Y. Dynamic impact behavior and deformation mechanisms of $Cr_{26}Mn_{20}Fe_{20}Co_{20}Ni_{14}$ high-entropy alloy. Mater Sci Eng A 2021;824:141858. https://doi.org/10.1016/j.msea.2021.141858.
[176] Gao X, Lu Y, Liu J, Wang J, Wang T, Zhao Y. Extraordinary ductility and strain hardening of $Cr_{26}Mn_{20}Fe_{20}Co_{20}Ni_{14}$ TWIP high-entropy alloy by cooperative planar slipping and twinning. Materialia (Oxf) 2019;8. https://doi.org/10.1016/j.mtla.2019.100485.

[177] Wu Z, Gao Y, Bei H. Thermal activation mechanisms and Labusch-type strengthening analysis for a family of high-entropy and equiatomic solid-solution alloys. Acta Mater 2016;120. https://doi.org/10.1016/j.actamat.2016.08.047.

[178] Hong SI, Moon J, Hong SK, Kim HS. Thermally activated deformation and the rate controlling mechanism in CoCrFeMnNi high entropy alloy. Mater Sci Eng 2017;682. https://doi.org/10.1016/j.msea.2016.11.078.

[179] Dirras G, et al. Mechanical behavior and microstructure of $Ti_{20}Hf_{20}Zr_{20}Ta_{20}Nb_{20}$ high-entropy alloy loaded under quasi-static and dynamic compression conditions. Mater Char Jan. 2016;111:106–13. https://doi.org/10.1016/j.matchar.2015.11.018.

[180] Senkov ON, Scott JM, Senkova Sv, Meisenkothen F, Miracle DB, Woodward CF. Microstructure and elevated temperature properties of a refractory TaNbHfZrTi alloy. J Mater Sci 2012;47(9). https://doi.org/10.1007/s10853-012-6260-2.

[181] Pérez-Prado MT, Hines JA, Vecchio KS. Microstructural evolution in adiabatic shear bands in Ta and Ta-W alloys. Acta Mater 2001;49(15). https://doi.org/10.1016/S1359-6454(01)00215-4.

[182] lei Hu M, dong Song W, bo Duan D, Wu Y. Dynamic behavior and microstructure characterization of TaNbHfZrTi high-entropy alloy at a wide range of strain rates and temperatures. Int J Mech Sci Sep. 2020;182. https://doi.org/10.1016/j.ijmecsci.2020.105738.

[183] Yao S, Pei X, Liu Z, Yu J, Yu Y, Wu Q. Numerical investigation of the temperature dependence of dynamic yield stress of typical BCC metals under shock loading with a dislocation-based constitutive model. Mech Mater 2020;140. https://doi.org/10.1016/j.mechmat.2019.103211.

[184] Regazzoni G, Kocks UF, Follansbee PS. Dislocation kinetics at high strain rates. Acta Metall 1987;35(12). https://doi.org/10.1016/0001-6160(87)90285-9.

[185] Introduction to high strain rate testing. In: Mechanical testing and evaluation; 2018. https://doi.org/10.31399/asm.hb.v08.a0003293.

[186] The use of flat-ended projectiles for determining dynamic yield stress I. Theoretical considerations. Proceedings of the Royal Society of London. Series A. Mathematical and Physical Sciences 1948;194(1038). https://doi.org/10.1098/rspa.1948.0081.

[187] Jones SE, Gillis PP, Foster JC, Wilson LL. A one-dimensional, two-phase flow model for taylor impact specimens. J Eng Mater Techno Trans ASME 1991;113(2). https://doi.org/10.1115/1.2903397.

[188] Orgorkie RM. Armor for combat vehicles-new armor materials. Mach Des 1969;41(27):36.

[189] Muskeri S, et al. Ballistic impact response of $Al_{0.1}$CoCrFeNi high-entropy alloy. Adv Eng Mater Jun. 2020;22(6). https://doi.org/10.1002/adem.202000124.

[190] Chung T-F, Chiu P-H, Tai C-L, Li Y-L, Wang L-M, Chen C-Y, et al. Investigation on the ballistic induced nanotwinning in the Mn-free $Fe_{27}Co_{24}Ni_{23}Cr_{26}$ high entropy alloy plate. Mater Chem Phys 2021;270:124707. https://doi.org/10.1016/j.matchemphys.2021.124707.

[191] Wang Z, Bei H, Baker I. Microband induced plasticity and the temperature dependence of the mechanical properties of a carbon-doped FeNiMnAlCr high entropy alloy. Mater Char 2018;139:373–81. https://doi.org/10.1016/j.matchar.2018.03.017.

[192] Guo W, Su J, Lu W, Liebscher CH, Kirchlechner C, Ikeda Y, et al. Dislocation-induced breakthrough of strength and ductility trade-off in a non-equiatomic high-entropy alloy. Acta Materialia 2020;185:45–54. https://doi.org/10.1016/j.actamat.2019.11.055.

[193] Zherebtsov S, Yurchenko N, Panina E, Tojibaev A, Tikhonovsky M, Salishchev G, et al. Microband-induced plasticity in a Ti-rich high-entropy alloy. J Alloys Compd 2020;842:155868. https://doi.org/10.1016/j.jallcom.2020.155868.

[194] Choudhuri D, Jannotti PA, Muskeri S, Shukla S, Gangireddy S, Mukherjee S, et al. Ballistic response of a FCC-B2 eutectic $AlCoCrFeNi_{2.1}$ high entropy alloy. J Dyn Behav Mater 2019;5:495–503. https://doi.org/10.1007/s40870-019-00220-z.

[195] Liu XF, Tian ZL, Zhang XF, Chen HH, Liu TW, Chen Y, et al. "Self-sharpening" tungsten high-entropy alloy. Acta Materialia 2020;186:257–66. https://doi.org/10.1016/j.actamat.2020.01.005.

[196] Jinxu L, Shukui L, Wei G, Haiyun Z, Fang N, Changqing S. Susceptibility to adiabatic shear band of tungsten heavy alloy fabricated through hot-hydrostatic extrusion and cold torsion. Rare Metal Mater Eng 2008;37:1360–3. https://doi.org/10.1016/s1875-5372(09)60037-0.

[197] Kim DK, Lee S, Noh JW. Dynamic and quasi-static torsional behavior of tungsten heavy alloy specimens fabricated through sintering, heat-treatment, swaging and aging. Mater Sci Eng 1998;247(1–2). https://doi.org/10.1016/s0921-5093(97)00547-9.

[198] Yu Y, Zhang W, Wang E. Effect of heat treatment on microstructure and mechanical properties of hot-hydrostatically extruded 93W-4.9Ni-2.1Fe alloy. J Alloys Compd 2015;622. https://doi.org/10.1016/j.jallcom.201411.009.

[199] Yang Y, Lianxi H, Erde W. Microstructure and mechanical properties of a hot-hydrostatically extruded 93W-4.9Ni-2.1Fe alloy. Mater Sci Eng 2006;435–436. https://doi.org/10.1016/j.msea.2006.07.074.

[200] Hazell PJ, Appleby-Thomas GJ, Philbey D, Tolman W. The effect of gilding jacket material on the penetration mechanics of a 7.62 mm armour-piercing projectile. Int J Impact Eng 2013;54. https://doi.org/10.1016/j.ijimpeng.2012.10.013.

[201] Ryu HJ, Hong SH, Baek WH. Microstructure and mechanical properties of mechanically alloyed and solid-state sintered tungsten heavy alloys. Mater Sci Eng 2000;291(1–2). https://doi.org/10.1016/S0921-5093(00)00968-0.

[202] Mishra B, Ramakrishna B, Jena PK, Siva Kumar K, Madhu V, Gupta NK. Experimental studies on the effect of size and shape of holes on damage and microstructure of high hardness armour steel plates under ballistic impact. Mater Des 2013;43. https://doi.org/10.1016/j.matdes.2012.06.037.

[203] Couque H, Nicolas G, Altmayer C. Relation between shear banding and penetration characteristics of conventional tungsten alloys. Int J Impact Eng 2007;34(3). https://doi.org/10.1016/j.ijimpeng.2005.12.003.

[204] Ravi Kiran U, Panchal A, Sankaranarayana M, Nageswara Rao GVS, Nandy TK. Effect of alloying addition and microstructural parameters on mechanical properties of 93% tungsten heavy alloys. Mater Sci Eng 2015;640. https://doi.org/10.1016/j.msea.2015.05.046.

[205] Kim DK, Lee S, Hyung Baek W. Microstructural study of adiabatic shear bands formed by high-speed impact in a tungsten heavy alloy penetrator. Mater Sci Eng 1998;249(1–2). https://doi.org/10.1016/s0921-5093(98)00565-6.

[206] Magness LS. High strain rate deformation behaviors of kinetic energy penetrator materials during ballistic impact. Mech Mater 1994;17(2–3). https://doi.org/10.1016/0167-6636(94)90055-8.

[207] Wei Z, Yu J, Li J, Li Y, Hu S. Influence of stress condition on adiabatic shear localization of tungsten heavy alloys. Int J Impact Eng 2001;26(1–10). https://doi.org/10.1016/s0734-743x(01)00137-3.

[208] Jiang ZJ, He JY, Wang HY, Zhang HS, Lu ZP, Dai LH. Shock compression response of high entropy alloys. Materials Research Letters Oct. 2016;4(4):226–32. https://doi.org/10.1080/21663831.2016.1191554.
[209] Zhao L, Zong H, Ding X, Lookman T. Anomalous dislocation core structure in shock compressed bcc high-entropy alloys. Acta Mater 2021;209. https://doi.org/10.1016/j.actamat.2021.116801.
[210] Remington TP, Remington BA, Hahn EN, Meyers MA. Deformation and failure in extreme regimes by high-energy pulsed lasers: a review. Mater Sci Eng 2017;688. https://doi.org/10.1016/j.msea.2017.01.114.
[211] Grady DE. The spall strength of condensed matter. J Mech Phys Solid 1988;36(3). https://doi.org/10.1016/0022-5096(88)90015-4.
[212] Curran DR, Seaman L, Shockey DA. Dynamic failure of solids. Phys Rep 1987;147(5–6):253–388. https://doi.org/10.1016/0370-1573(87)90049-4.
[213] Antoun T, Seaman L, Curran DR, Kanel GI, Razorenov Sv, Utkin Av. Spall fracture. Springer Science & Business Media; 2003.
[214] Weng J, Tan H, Wang X, Ma Y, Hu S, Wang X. Optical-fiber interferometer for velocity measurements with picosecond resolution. Appl Phys Lett 2006;89(11). https://doi.org/10.1063/1.2335948.
[215] Stepanov Gv, Romanchenko VI, Astanin Vv. Experimental determination of failure stresses under spallation in elastic-plastic waves. Probl Strength 1977;8:96–9.
[216] Yang Y, Yang S, Wang H. Effects of the phase content on dynamic damage evolution in $Fe_{50}Mn_{30}Co_{10}Cr_{10}$ high entropy alloy. J Alloys Compd 2021;851(Jan). https://doi.org/10.1016/j.jallcom.2020.156883.
[217] Yang Y, Jiang Z, Chen J, Guo Z, Tang T, Hu H. The characteristics of void distribution in spalled high purity copper cylinder under sweeping detonation. Phil Mag 2018;98(9). https://doi.org/10.1080/14786435.2017.1417649.
[218] Yang Y, et al. Multidimensional study on spall behavior of high-purity copper under sliding detonation. Metall Mater Trans A 2015;46(9). https://doi.org/10.1007/s11661-015-3027-9.
[219] Yang Y, Chen J, Peng Z, Guo Z, Tang T, Hu H, et al. X-ray quantitative analysis on spallation response in high purity copper under sweeping detonation. Mater Sci Eng A 2016;667:54–60. https://doi.org/10.1016/j.msea.2016.04.090.
[220] Yang Y, Jixiong C, Zhaoliang G, Tiegang T, Haibo H, Yanan F. 3-D characterization of incipient spallation response in cylindrical copper under sweeping detonation. J Mater Res 2017;32:1499–505. https://doi.org/10.1557/jmr.2017.25.
[221] Zhang NB, Xu J, Feng ZD, Sun YF, Huang JY, Zhao XJ, et al. Shock compression and spallation damage of high-entropy alloy $Al_{0.1}CoCrFeNi$. J Mater Sci Technol 2022;128:1–9. https://doi.org/10.1016/j.jmst.2022.02.056.
[222] Hawkins MC, Thomas S, Hixson RS, Gigax J, Li N, Liu C, et al. Dynamic properties of fecrmnni, a high entropy alloy. Mater Sci Eng A 2022;840:142906. https://doi.org/10.1016/j.msea.2022.142906.
[223] Thürmer D, Zhao S, Deluigi OR, Stan C, Alhafez IA, Urbassek HM, et al. Exceptionally high spallation strength for a high-entropy alloy demonstrated by experiments and simulations. J Alloys Compd 2022;895:162567. https://doi.org/10.1016/j.jallcom.2021.162567.
[224] Xie ZC, Li C, Wang HY, Lu C, Dai LH. Hydrogen induced slowdown of spallation in high entropy alloy under shock loading. Int J Plast 2021;139:102944. https://doi.org/10.1016/j.ijplas.2021.102944.
[225] Ladani L, Sadeghilaridjani M. Review of powder bed fusion additive manufacturing for metals. Metals 2021;11(9). https://doi.org/10.3390/met11091391.
[226] Wu Y, Zhang F, Yuan X, Huang H, Wen X, Wang Y, et al. Short-range ordering and its effects on mechanical properties of high-entropy alloys. J Mater Sci Technol 2021;62:214–20. https://doi.org/10.1016/j.jmst.2020.06.018.
[227] Lu K. Stabilizing nanostructures in metals using grain and twin boundary architectures. Nat Rev Mater 2016;1. https://doi.org/10.1038/natrevmats.2016.19.
[228] Gangireddy S, Gwalani B, Banerjee R, Mishra RS. High strain rate response of $Al_{0.7}CoCrFeNi$ high entropy alloy: dynamic strength over 2 GPa from thermomechanical processing and hierarchical microstructure. J Dynam Behav Mater 2019;5(1). https://doi.org/10.1007/s40870-018-00178-4.